

**Local Quantum Impurities in Large-Scale Systems:
Trapped-Hole Diffusion in Cadmium-Chalcogenide Nanocrystals
and Locally-Varying Vibrational Modes in Polytetrafluoroethylene**

by

Robert Peyton Cline

A.B., Chemistry, Princeton University, 2013

A thesis submitted to the
Faculty of the Graduate School of the
University of Colorado in partial fulfillment
of the requirement for the degree of
Doctor of Philosophy, Chemical Physics
Department of Chemistry

2020

Committee Members:

Joel Eaves

Sandeep Sharma

Gordana Dukovic

Veronica Vaida

Charles Rogers

ProQuest Number: 28092408

All rights reserved

INFORMATION TO ALL USERS

The quality of this reproduction is dependent on the quality of the copy submitted.

In the unlikely event that the author did not send a complete manuscript and there are missing pages, these will be noted. Also, if material had to be removed, a note will indicate the deletion.



ProQuest 28092408

Published by ProQuest LLC (2020). Copyright of the Dissertation is held by the Author.

All Rights Reserved.

This work is protected against unauthorized copying under Title 17, United States Code
Microform Edition © ProQuest LLC.

ProQuest LLC
789 East Eisenhower Parkway
P.O. Box 1346
Ann Arbor, MI 48106 - 1346

Cline, Robert Peyton (Ph.D., Chemical Physics)

Local Quantum Impurities in Large-Scale Systems:

Trapped-Hole Diffusion in Cadmium-Chalcogenide Nanocrystals and

Locally-Varying Vibrational Modes in Polytetrafluoroethylene

Thesis directed by Associate Professor Joel D. Eaves

Abstract

Condensed matter systems involve upwards of 10^{23} degrees of freedom. However, Bloch's theorem allows one to truncate these systems down to their smallest irreducible parts, and the development of methods like density functional theory (DFT) has made the study of large systems comprising a few thousand electrons possible. Furthermore, theoretical models can help bridge the gap between computations and reality, as they provide physically-relevant insights for a variety of phenomena, such as those related to local disorder and impurity states. This dissertation describes efforts to understand two phenomena involving local disorder and impurities in nanoscale and mesoscale systems through a balance of heavy computations and systematic theoretical modeling.

The first phenomenon corresponds to trapped-hole diffusion in cadmium-chalcogenide nanocrystals. Recent experimental data on CdS and CdSe nanorod systems show that photoexcited holes in these particles are dynamic and undergo diffusion along the surfaces of the nanorods. I develop and present a semi-periodic DFT model for the nanocrystal surfaces and elucidate the nature of the surface-trapped hole states and the mechanisms by which they diffuse. In the presence of thermal fluctuations, these holes localize to the nonbonding sp^3 orbitals on surface chalcogen atoms and form nonadiabatic small polarons. The trapped holes diffuse along the surfaces in two quantifiable ways: direct hopping between orbitals and indirect tunneling, or superexchange, through the bulk electronic states. I use Green's functions to calculate the superexchange mechanism to all orders in perturbation theory, yielding a formally exact model for trapped-hole diffusion.

The second phenomenon corresponds to extreme local frequency shifts within mesoscale

samples of polytetrafluoroethylene (PTFE). Emerging experimental vibrational microscopy data collected for micron-sized samples of melted PTFE reveal locally-distinct spectroscopic signatures throughout the samples. In particular, these experiments measure a systematic correlation between the symmetric and antisymmetric stretching modes. I parametrize a vibrational-exciton model from DFT calculations that relates the mesoscale structure of the sample to the observable symmetric and antisymmetric stretching modes of PTFE. In doing so, I develop a mesoscopic theory for the spatially-varying polarization and show that these spectroscopic features are electrostatic in origin.

Acknowledgements

To my family: First and foremost, I want to thank my parents, Alan Cline and Paige Thomas Cline, for supporting me immensely and unconditionally throughout the years. I especially want to thank my dad, Alan, who sent me to some of the best schools I could have hoped for: first to Pulaski Academy, one of the best schools in my home state of Arkansas, and then to Princeton University, one of the best schools in the world. Those decisions have directly led to the success I have found here at the University of Colorado Boulder, and I could not be more thankful. I also want to thank my immediate extended family, Susan Nelson and Laura Pritchett, and my grandparents — Robert Emmett Cline, Mary Jo Cline, Tommy Thomas, and Kathryn Thomas — for their support and curiosity in my life endeavors over the years.

To my high school teachers: I want to thank my high school teachers for sparking my interest in science as a career in the first place. Alecia Castleberry, thank you for instilling in me my love for chemistry, and thank you, Doug Reed, for instilling in me my love for physics. I have thought about your classes a lot over the years, and through your teachings, I realized not only how important these two subjects are, but also how relevant they are to promoting change in our everyday lives. But most importantly, you taught me that science is fun, which is the best motivation for me.

To my Princeton experience: I want to thank Princeton University in general for the extensive training to perform difficult tasks. This was an invaluable skill to have during my time as a graduate student. More specifically, I want to thank the conductor of the Princeton University Orchestra, Michael Pratt, for believing in my musical talent at the time and pushing for my acceptance into the university. It is likely that without my love for music, I might not have gotten the opportunity to go to Princeton at all, and I cannot be more thankful for that opportunity. And finally, thanks to all my friends from Princeton who have enriched my life to this very day: David Faris, Sean Conrad, Evan Larson, Alex Stokes, Matthew Marder, and everyone else for all the fun times and interesting conversations.

To Gordana and James: Thank you so much for your guidance and also for including me on the trapped-hole diffusion project. I learned more than I could have hoped through this project, and I will continue to learn from it after completing this dissertation. I especially want to thank James Utterback for being there whenever I needed help and for always having encouraging words to say to me. Often, I felt under-productive and overly stressed about my work moving slowly at times, and just hearing “You’re doing a great job” on multiple occasions meant more to me than anything I learned in my classes.

To Joel: My success during my graduate career is due in large part to Joel for his guidance these last several years. Thanks for putting up with the same twenty questions I asked each week and giving me time to struggle and figure out the intricate details of my work. You instilled in me the importance of understanding the fundamental details of each project and to always frame the problem at hand in the proper experimental context, an invaluable tool for a theorist to have. And especially, thank you for keeping me and our whole group grounded and safe during the COVID-19 crisis. From allowing us to work from home until this pandemic finally ends, to the weekly Zoom happy hours on Fridays, you kept us all safe and motivated during these unprecedented times.

To my Colorado friends: Finally, I want to thank my friends here in Colorado. Steven Sartor, Alex Gilligan, Ethan Miller, Ben Williamson, Jesse Ruzicka, Ryan Dill, Austin Cano, and everyone else: thanks for all the fun times we have had.

Contents

1	Introduction	1
1.1	Theoretical Background	1
1.2	Experimental Motivation and Current Work	3
1.2.1	Cadmium-Chalcogenide Nanocrystals	3
1.2.2	Polytetrafluoroethylene (PTFE)	6
1.3	Future Work	7
2	On the Nature of Trapped-Hole States in CdS Nanocrystals and the Mechanism of Their Diffusion	9
2.1	Abstract	9
2.2	Introduction	10
2.3	Methods	12
2.3.1	DFT Calculations	12
2.3.2	Wannier Localization	15
2.4	Results and Discussion	18
2.5	Conclusions	19
2.6	Computational Details	20
2.7	Appendix A Contents	21
2.8	Acknowledgement	21
3	Surface-Trapped Hole Diffusion in CdS and CdSe: The Superexchange Mechanism	22

3.1 Abstract	22
3.2 Introduction	23
3.3 Methods	25
3.3.1 DFT Calculations	26
3.3.2 Wannier Localization	28
3.3.3 Green's Function Formalism	31
3.4 Results and Discussion	35
3.5 Conclusions	37
3.6 Appendix B Contents	38
3.7 Acknowledgement	39
4 Locally-Varying Vibrational Modes in Polytetrafluoroethylene	40
4.1 Abstract	40
4.2 Introduction	41
4.3 Methods	43
4.3.1 Experiment	43
4.3.2 Theory	46
4.3.2.1 DFT Calculations	46
4.3.2.2 Vibrational-Exciton Hamiltonian	47
4.3.2.3 Linear Response Theory	53
4.4 Results and Discussion	58
4.4.1 Model Fits of DFT Data	58
4.4.2 Local Spectra Calculations	61
4.5 Conclusions	65
4.6 Computational Methods	65
5 Future Work: Phonon Modes Assisting Trapped-Hole Diffusion in CdS and CdSe Nanocrystals	67

5.1	Introduction	67
5.2	Methods	68
5.2.1	Spin-Boson Hamiltonian	68
5.2.2	Molecular Dynamics	73
A	Supplementary Information for Chapter 2: On the Nature of Trapped-Hole States in CdS Nanocrystals and the Mechanism of Their Diffusion	75
A.1	Derivation of the Diffusion Constants, D_{\parallel} and D_{\perp}	75
A.2	Crystal Structure / VASP Convergence Details	80
A.2.1	Bulk Cell Parameters	80
A.2.2	Bulk Convergence Details	80
A.2.3	($10\bar{1}0$) Surface Slab Parameters	81
A.2.4	$3 \times 4 \times 3$ “Anti-Aliased” Surface Slab	82
A.2.5	Pseudohydrogen Passivation and Ionic Relaxation Scheme	82
A.2.6	Surface Convergence Details	84
A.3	Wannier Localization Procedure	85
A.3.1	Wannier90: A Brief Description	85
A.3.2	Convergence Criteria	86
A.3.3	The Outer and Inner Energy Windows	86
A.4	Alternate Electronic Structure Comparisons	87
A.4.1	Fully-Passivated $2 \times 2 \times 8$ Surface Slab	87
A.4.2	Asymmetric $2 \times 2 \times 8$ Surface Slab	89
B	Supplementary Information for Chapter 3: Surface-Trapped Hole Diffusion in CdS and CdSe: The Superexchange Mechanism	91
B.1	DFT Parameters / Convergence Details for CdSe	91
B.1.1	Bulk Calculations	91
B.1.2	Surface Slab Calculations	92

B.1.2.1	Surface Slab Construction	92
B.1.2.2	Passivation/Relaxation Schemes	93
B.1.2.3	Convergence Details	94
B.1.2.4	Miscellaneous	94
B.2	Wannier-Basis Hamiltonian	95
B.3	Mapping onto the Fano-Anderson Problem	97
B.4	Effect of Wannier Localization Scheme and Orbital Energies on Green's Function Analysis	98
B.4.1	Wannier Localization with Disentanglement for CdS	99
B.4.2	Wannier Localization without Disentanglement for CdS: The “Excluded Bands” Procedure	103
B.4.2.1	Excluded Bands	103
B.4.2.2	Included Bands	104
B.4.3	Wannier Localization without Disentanglement for CdSe	107
B.4.3.1	Excluded Bands	107
B.4.3.2	Included Bands	108
B.5	Wannier Localization Convergence Details	109
B.6	Orbital Spread Comparison	109
B.7	Asymmetric CdS and CdSe Diffusion Results	111
B.8	Perpendicular Couplings: Symmetric Slabs	112
Bibliography		114

List of Tables

3.1	Relevant energetic couplings (in meV) for trapped-hole diffusion in Cd-chalcogenide nanocrystals	37
4.1	Symmetric (S) and antisymmetric (AS) peak positions from DFT	59
4.2	Fit parameters for the helical conformations of PTFE	61
A.1	Calculated tunneling matrix elements for CdS surface slabs	85
B.1	Relevant matrix elements (in meV) for trapped-hole diffusion in Cd-chalcogenide nanocrystals as calculated using the asymmetric slab variants	112
B.2	Perpendicular-hop matrix elements, t_{\perp} and σ_{\perp} , between neighboring surface chalcogen sites in Cd-chalcogenide nanocrystals for the $2 \times 2 \times 8$ symmetric slab variants	113

List of Figures

2.1	Illustration and cross section of a CdS nanorod and surface	11
2.2	Total density of states for a CdS nanorod surface	14
2.3	Band structure of the CdS surface slab near the Fermi energy	16
2.4	The relevant states used to construct the effective tight-binding Hamiltonian for surface holes	17
3.1	Illustration and cross section of a cadmium-chalcogenide nonuniform nanorod and adiabatic DFT results.	27
3.2	The relevant orbitals and tight-binding grid for surface-trapped holes	29
3.3	Trace of the negative imaginary part of the bare Green's function for a surface hopping event	33
3.4	Energy correlation diagram for a pair of donor/acceptor surface states	36
4.1	The 13_6 helical conformation of PTFE	41
4.2	The 15_7 helical conformation of PTFE	42
4.3	Experimental setup and results	44
4.4	Experimental correlation plot for the symmetric and antisymmetric vibra- tional modes of a sample of melted PTFE	45
4.5	Closeup view of one unit of CF_2 in a strand of PTFE	47
4.6	Turning on interactions in a vibrational-exciton model	48
4.7	Angled view of a helical PTFE molecule	51
4.8	Vibrational spectra, $C(\omega)$, for different conformers and fits of PTFE. . . .	60

4.9	Cross section of a bundle of parallel PTFE strands for local spectra calculations	62
4.10	Local spectra calculations for various PTFE strands and fit parameters	63
4.11	Summary of the peak positions of local spectra calculations	64
5.1	Energy level diagram of the diabatic donor and acceptor states	70
A.1	Schematic of the surface sulfur sites in CdS.	76
A.2	Side views of $2 \times 2 \times 8$ symmetric and asymmetric surface slabs	83
A.3	Total DOS for a fully-passivated $2 \times 2 \times 8$ CdS surface slab	88
A.4	Total DOS and band structure for the $2 \times 2 \times 8$ asymmetric CdS slab	89
B.1	Side views of the geometrically-relaxed $2 \times 2 \times 8$ symmetric and asymmetric CdSe slabs	93
B.2	Illustration of the real-space Wigner-Seitz (WS) supercell generated by Wannier90 for an orthorhombic input cell	96
B.3	DFT band structure for the symmetric $2 \times 2 \times 8$ CdS surface slab	100
B.4	Variation of the surface NBO energy across increasing frozen window widths for the symmetric CdS slab	101
B.5	Band structures for the symmetric CdS surface slab	102
B.6	Projected densities of states (PDOS) over the interval $-8 < E - E_{Fermi} < -5.5$ eV for all atoms in the symmetric CdS surface slab	103
B.7	PDOS over the interval $-12.5 < E - E_{Fermi} < -10.5$ eV for all atoms in the symmetric CdS surface slab	105
B.8	PDOS over the interval $-4.45 < E - E_{Fermi} < -4.15$ eV for all atoms in the symmetric CdS surface slab	105
B.9	PDOS over the interval $-4.1 < E - E_{Fermi} < 0.2$ eV for all atoms in the symmetric CdS surface slab	106
B.10	PDOS over the interval $-8.5 < E - E_{Fermi} < -5.5$ eV for all atoms in the symmetric CdSe surface slab	107

B.11 PDOS over the interval $-12.5 < E - E_{Fermi} < -11$ eV for all atoms in the symmetric CdSe surface slab	108
B.12 PDOS over the interval $-4.6 < E - E_{Fermi} < -4.3$ eV for all atoms in the symmetric CdSe surface slab	108
B.13 PDOS over the interval $-4.1 < E - E_{Fermi} < 0.2$ eV for all atoms in the symmetric CdSe surface slab	109
B.14 Converged surface NBO spread as a function of frozen window width for the symmetric CdS surface slab	110
B.15 Converged surface NBO spread as a function of frozen window width for the symmetric CdSe surface slab	111

Copyright

All images, figures and illustrations are the work of the author unless otherwise noted. Text and figures are © 2020 Robert Peyton Cline unless otherwise noted.

“People are always asking for the latest developments in the unification of this theory with that theory, and they don’t give us a chance to tell them anything about one of the theories that we know pretty well. They always want to know things that we don’t know.”

Richard P. Feynman

Chapter 1

Introduction

1.1 Theoretical Background

Condensed matter systems can involve upwards of 10^{23} degrees of freedom. Due to Bloch's theorem, however, we can study such large systems on a much smaller scale without loss of generality. Conceived in 1928,¹ Bloch's theorem states the wave function of a perfect crystal is periodic and reflects the same periodicity as that of the atoms that make up the crystal structure. The existence of this periodicity, which is a translational symmetry, means the total structure can be reduced to its smallest indivisible portion: the primitive unit cell. This unit cell contains the least number of atoms necessary such that replicating the cell in all periodic directions produces the correct macroscopic structure. Electronic band structures, band gaps, and other unique properties of the crystal can be evaluated in this reduced representation.

The advent of Bloch's theorem was instrumental for the development of many approximate, yet effective, methods to study simple periodic systems from the 1930s to early 1960s.²⁻⁹ Most often, these applications of Bloch's theorem were used to describe relatively simple metal crystal structures, such as sodium, iron, copper, zinc, and aluminum.¹⁰ However, addressing more complicated systems still needed much development.

In 1964, one seminal development came from the work of Hohenberg and Kohn, who developed the theory for the inhomogeneous electron gas.¹¹ This work showed that the ground state of an interacting electron gas in an external potential corresponds to a universal

functional of the electron density in the absence of the external potential. Through this theory, the electron density is described as a function of only three spatial coordinates, which is far fewer than the $3N$ spatial coordinates typically needed to describe the many-body wave function of N electrons. Today, this theory is aptly called density functional theory (DFT) and is the foundation of many modern chemistry computations.

DFT is indeed a powerful tool for the modern research scientist. Modern computational packages allow the researcher to evaluate the electronic structure of both molecular and solid state systems that comprise up to hundreds of atoms and thousands of electrons. Furthermore, DFT is accessible to both theorists and non-theorists alike, and it has helped bridge the gap between theory and experiment.

While DFT represents one aspect of progress that has been instrumental for studying more complex systems, the development and use of rigorous theoretical models for these systems provides another source of progress. One model of particular note concerns Anderson localization. Philip Anderson showed in 1958¹² that electron localization is possible in a lattice, provided that the degree of disorder in the lattice is sufficiently large. In fact for the one- and two-dimensional variants of this model, it turns out that *any* amount of disorder causes localization. This result is peculiar because, if the disorder is gone entirely, then electrons within that lattice would hop between sites like normal. Therefore, disorder in this model yields a lattice that changes from a conducting phase to an insulating phase: an electron can locally trap in the lattice and never again move to the rest of the lattice. The source of the disorder in Anderson's model is that the energy varies randomly from site to site, a phenomenon that certainly occurs in any realistic system at finite temperature. This illustrates that disorder as simple as random energy fluctuations can have potentially extreme consequences for the physical properties of a system. Anderson received the Nobel Prize in physics in 1977¹³ in part because of the contributions from this work, signifying its importance in the theoretical community.

Another example of a powerful theoretical model concerns the Kondo effect. Popularized

by Jun Kondo in 1964,¹⁴ this model represents a staple problem in the condensed matter literature¹⁵ and describes the scattering of conduction electrons in nonmagnetic metals due to a magnetic impurity, resulting in a resistance minimum at non-zero temperature. This is in contrast to the expected result that the resistance minimum occurs at zero-temperature. The idea that a single impurity state can cause such a drastic change in the expected results is just one reason why this model is so important. In fact, this model was later studied by Kenneth Wilson in 1975¹⁶ when he solved the problem within his theoretical formalism of the renormalization group, earning him the Nobel Prize in physics in 1982.¹⁷ The importance and influence of this model and the ideas that came from it cannot be overstated.

While these two particular models do not come up again in this dissertation, I discuss them in this introduction because they illustrate a core theme: careful theoretical modeling of complex systems has led to great achievements in science, and developing a model description of the problem at hand can lead to insights and solutions that would otherwise go unnoticed. DFT can simulate systems with thousands of electrons, and computers in the last decade have become more powerful than ever before. But just because large systems can be calculated more accurately than in the past, this does not guarantee a correct answer will be found. In fact, as I will show in Chapter 2, taking some DFT results at face value without conforming to some relevant model description might lead to the wrong interpretation entirely.

1.2 Experimental Motivation and Current Work

1.2.1 Cadmium-Chalcogenide Nanocrystals

Employing both theoretical modeling and heavy computations is particularly useful for the study of nanocrystal surfaces, which is my research focus for Chapters 2 and 3. These surfaces are rife with complexity, which could give rise to disorder and impurity states not unlike those discussed previously. To describe a complex system such as a surface, a large

unit cell must be used to capture the necessary features. This requires methods like DFT to achieve a reasonable starting point for future theoretical frameworks.

An early understanding of the complexities of nanocrystals dates back to 1984. Louis Brus¹⁸ developed an elementary model for the excited states of a few types of semiconductor nanoparticles, which were sized approximately 5 nanometers in diameter. Brus noticed that the electronic properties of these particles differed substantially from the bulk electronic properties. In fact, he found that increasing the size of the nanoparticles by a factor of two or three decreased the calculated excitation energies by as much as 1 eV, suggesting these particles had highly tunable band gaps at the nanoscale level.

One particular system Brus studied in his work was cadmium sulfide. Along with a similar material, cadmium selenide, these cadmium-chalcogenide nanocrystals are among the most well-studied systems in nanoscience.^{18–21} Much research has been conducted on this class of materials since the 1980s, in particular because they show promise for use in optoelectronic applications, such as solar energy harvesting.^{22–27}

In both CdS and CdSe nanocrystals, and semiconductor colloidal nanocrystals in general, surface traps are intricately linked to the fates of photoexcited carriers, which are critical for energy harvesting. Despite their importance, the microscopic nature and character of the trapped states have remained ill-defined over the years. As a result, an area of active research concerns the impact of surface states on the nature and dynamics of photoexcited carriers.^{28–33} In cadmium-chalcogenide systems, electron and hole traps form on the surface.^{19,34–43} Electron traps are associated with undercoordinated cadmium atoms on the surface; however, in most syntheses, capping ligands eliminate these traps by forming bonds with the surface cadmium atoms.^{38,43–47} Chalcogen atoms at the surface often remain under-coordinated, resulting in hole traps on the surface corresponding to these atoms.^{36,37,42,43,48–50}

The conventional view has been that surface-trapped holes in CdS and CdSe nanocrystals are static and immobile; however, work by Utterback *et al.* in 2016 for CdS³⁰ and in 2018 for CdSe³² showed that this is not necessarily the case. Transient absorption experiments

conducted in Refs. [30, 32] showed the first direct evidence that trapped holes are actually mobile at room temperature. In particular, hole states trapped on the surfaces of these nanoparticles undergo net one-dimensional diffusion. The authors employed a diffusion–annihilation model to explain their data, which revealed a signature $t^{-1/2}$ power-law signal decay.^{30,32} They hypothesized that the holes undergo an effective one-dimensional random walk in discrete steps between neighboring atomic sites on the surface.

While these experimental advancements helped uncover this critical feature of surface-trapped holes in CdS and CdSe nanocrystals, these states had yet to be characterized theoretically from the point of view of diffusion. The modeling conducted by Utterback *et al.*^{30,32} could not determine the exact mechanism for diffusion since they did not have direct access to the relevant atomic and electronic structures. This new development in a widely-researched field demanded further theoretical investigation.

In Chapter 2, I begin with the problem of surface-trapped hole diffusion in CdS nanorods. To assess the mechanism of diffusion, I start from first principles and employ DFT to generate approximate, zero-temperature, ground-state atomic and electronic structures for the relevant CdS surface configuration. These DFT results form the foundation of this model and future models. From here, I discover the existence of hole states that are localized to the surface sulfur atoms but delocalized across the entire surface. At finite temperature, however, I show that these delocalized adiabatic states will decohere under the influence of thermal fluctuations and will instead localize to atomic orbitals centered at surface sulfur sites. In doing so, I employ a systematic change of basis protocol to generate a set of diabatic — localized — atomic orbitals. It turns out the relevant quantities for trapped-hole diffusion are the direct tunneling matrix elements between neighboring surface hole orbitals, and these matrix elements contribute to an effective one-dimensional diffusion constant for trapped-hole motion on the CdS surface. This mechanism corresponds to “direct” transfer between the orbitals. At this point, I neglect higher-order interactions that might tune these tunneling matrix elements for the sake of developing the model, leaving room for future

improvements.

In Chapter 3, I expand the model developed in Chapter 2 to describe trapped-hole diffusion in CdSe. Additionally, I extend the formalism to include previously-neglected corrections to the tunneling matrix elements for both CdS and CdSe. These corrections, which I calculate exactly for these materials, involve tunneling from a donor orbital into the bulk electronic states and then to the final acceptor orbital. The bulk electronic states thus act as virtual hole states. This virtual tunneling mechanism is also called “superexchange.” The superexchange corrections tune the direct tunneling amplitudes substantially and yield quantitative agreement with more recent experimental results.³³ The corrections are not so substantial, however, as to invalidate the local-orbital picture established in Chapter 2. The fact that these corrections are exact illustrates a rather interesting property of trapped-hole diffusion in CdS and CdSe nanocrystals: the superexchange mechanism for this phenomenon is accurate to all orders in perturbation theory. All possible paths through the relevant bulk electronic states are now explored in this updated diffusion model.

1.2.2 Polytetrafluoroethylene (PTFE)

In Chapter 4, I take a departure from the diffusion project and apply the combined DFT/modeling methodology to a different system, polytetrafluoroethylene (PTFE). PTFE is a fluorinated linear polymer with many phases near room temperature. It is often considered as a model system for vibrational spectroscopy due to its high oscillator density and large C–F oscillator transition dipole moments.^{51,52} The phases that exist near room temperature differ not only in their molecular packing, but also in the conformations of individual molecules. Much conformational disorder is observed in the crystalline phase as the temperature varies between 0 and 30 °C.^{51,53,54}

Emerging experimental work from the Raschke group has shown that samples of melted PTFE, hundreds of nanometers wide and tall, exhibit peculiar spectroscopic signatures. In particular, when measuring distinct regions corresponding to various thicknesses of a

melted PTFE sample, the experiments show positively-correlated shifts of the symmetric and antisymmetric stretching modes of the molecules. These modes, which usually occur near 1160 and 1220 cm^{-1} , respectively, shift by as much as 25 cm^{-1} in different regions of this mesoscopic sample. Such extreme frequency shifts for such large samples could not be explained by typical means, like temperature-induced spectral variations and local heterogeneities.

Using their experiments as a backdrop, I develop a mesoscopic theory for the spatially-varying polarization within their samples of PTFE. Like in previous chapters, I again start from first principles and employ DFT as the foundation for a model. I then construct a model Hamiltonian for the vibrational excitations in the sample, specifically the local C–F oscillators that constitute the molecules of PTFE, and I use linear response theory to quantify the spatially-varying polarization of each oscillator. I show that local C–F oscillators that exist in different molecular environments yield distinct spectra. The mechanism for these differences is electrostatic in nature: the dipole-dipole interaction between oscillators depends sensitively on the relative orientation and distance between oscillators. C–F oscillators in bulk-like regions of a sample will experience different dipole-dipole forces compared to C–F oscillators in the interface regions of a sample.

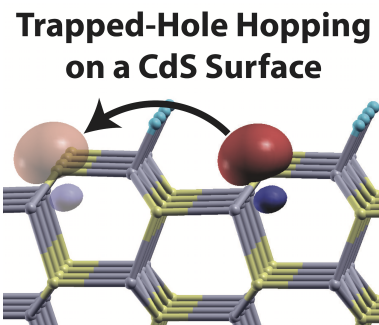
1.3 Future Work

In Chapter 5, I conclude the dissertation by proposing future work that ties all previous chapters together. I propose to apply the ideas of linear response employed in Chapter 4 to the diffusion problem in Chapters 2 and 3. In doing so, I aim to study the relevant *dynamical* quantities that influence trapped-hole diffusion, since the *static* picture with superexchange corrections is now accurate to infinite order in perturbation theory. Doing so will require calculations involving the normal modes since the vibrations of a crystal structure at finite temperature are superpositions of the crystal’s phonon modes. These vibrations can influence

trapped-hole diffusion, and understanding which phonons are most important is paramount for manipulating diffusion in CdS and CdSe nanocrystals. In Chapters 2 and 3, I write down a connection to the phonon modes in equation form, but they cannot be evaluated explicitly. Using a combination of linear response and molecular dynamics, I propose to extract the important phonon modes and calculate the relevant electron–phonon coupling terms that link the phonons to the diabatic hole orbitals. Doing so will help inform, or ideally predict, how future experiments can influence trapped-hole diffusion in CdS and CdSe nanocrystals.

Chapter 2

On the Nature of Trapped-Hole States in CdS Nanocrystals and the Mechanism of Their Diffusion*



2.1 Abstract

Recent transient absorption experiments on CdS nanorods suggest that photoexcited holes rapidly trap to the surface of these particles and then undergo diffusion along the rod surface. In this Chapter, we present a semi-periodic density functional theory model for the CdS nanocrystal surface, analyze it, and comment on the nature of both the hole-trap states and the mechanism by which the holes diffuse. Hole states near the top of the valence band form an energetic near continuum with the bulk and localize to the nonbonding sp^3 orbitals on surface sulfur atoms. After localization, the holes form nonadiabatic small polarons that move between the sulfur orbitals on the surface of the particle in a series of uncorrelated,

* Adapted with permission from Cline, R. P.; Utterback, J. K.; Strong, S. E.; Dukovic, G.; and Eaves, J. D. *J. Phys. Chem. Lett.* **2018**, 9, 3532–3537. (Copyright © 2018, American Chemical Society).

incoherent, thermally activated hops at room temperature. The surface-trapped holes are deeply in the weak-electronic coupling limit and, as a result, undergo slow diffusion.

2.2 Introduction

In semiconductor colloidal nanocrystals, surface traps play a pivotal role in deciding the fates of photoexcited carriers. Despite their importance, the microscopic nature and character of the trapped states remain elusive. In cadmium-chalcogenide systems like CdS and CdSe, electron and hole traps form on the surface.^{19,34–43} In most syntheses, capping ligands form bonds with the cadmium atoms at the surface and turn electron trapping into a minor decay pathway.^{38,43–47} In contrast, chalcogen atoms at the surface often remain under-coordinated and participate in hole trapping.^{36,37,42,43,48–50} The valence band holes in these materials exhibit subpicosecond lifetimes, the quantum yield for band gap photoluminescence is low, and there is emission from recombination between trapped holes and conduction band electrons.^{38,41,48,50,55–60} The energies of the hole states relative to the bulk valence band and the extent of wave function localization within the trapped states of nanocrystals have mostly been inferred from experimental spectra, though calculations for small clusters do exist.^{37,42,43,61} Recent work by Utterback *et al.*³⁰ makes the picture richer, showing that trapped holes are not static but are mobile at room temperature. That work showed that a one-dimensional diffusion–annihilation model could explain the long-lived power law decays in transient absorption spectra of nanorods and hypothesized that hole diffusion occurs through hopping, where hops occur on length scales that are on the order of individual bond lengths. Deducing the mechanism for this hole motion and testing that hypothesis³⁰ is a principal goal of this Chapter.

In this work, we use density functional theory (DFT) to describe the atomic and electronic structure of the surface and bulk states of CdS nanorods. By parametrizing a tight-binding Hamiltonian from the DFT data, we put forward a mechanism for the motion of trapped holes

on the surface by computing hole hopping rates using Holstein small polaron/nonadiabatic Marcus theory. We show that the rates are related to an anisotropic diffusion coefficient, and from the rate theory, we propose a lower bound on the reorganization energy for hole hopping that is consistent with the experimental data reported in Ref. [30].

As Figure 2.1A illustrates, CdS nanorods exhibit six identical faces, with all facets characterized by the $(10\bar{1}0)$ Miller–Bravais index.^{44,62,63} On this surface, both cadmium and sulfur

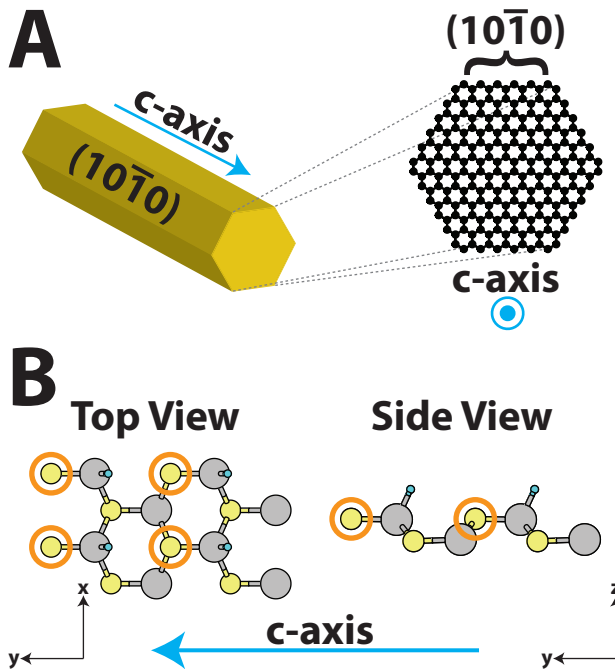


FIGURE 2.1: (A) Illustration and cross section of a CdS nanorod. The cross section shows the six radial surfaces, which are all crystallographically the same and correspond to the $(10\bar{1}0)$ Miller–Bravais index. The crystal c -axis runs parallel to the long axis of the nanorod. (B) Surface atoms forming the top layer of the computationally relaxed supercell, showing eight cadmium (gray) and eight sulfur (yellow) atoms from the top-down and side views. Pseudohydrogen atoms, used as a surrogate for passivating ligands, appear in blue. Orange circles outline the surface sulfur atoms. The remaining atoms forming the supercell are not shown (see Figure A.2A for the full structure). The two small axes in black denote the orthorhombic coordinates mentioned in the text.

atoms make three bonds to the crystal lattice, leaving one orbital on each atom exposed to the surface to be either passivated by a ligand or left as a dangling bond.

2.3 Methods

2.3.1 DFT Calculations

To construct a computational model for the CdS bulk and surface where ligands passivate cadmium but not sulfur on the surface, we begin by optimizing the nuclear positions of a $2 \times 2 \times 2$ wurtzite supercell in the bulk phase by minimizing the energy, changing both atomic positions and cell dimensions, at constant stress. To build the surface “slab” supercell from the bulk wurtzite cell, we use the fact that a wurtzite crystal cleaved along the $(10\bar{1}0)$ plane has an orthorhombic symmetry,^{62,64} with the sulfur atoms forming a rectangular lattice in the orthorhombic $x-y$ plane for CdS (Figure 2.1B). We choose coordinates so that the orthorhombic $x-y$ plane coincides exactly with the wurtzite crystal $b-c$ plane. From the $2 \times 2 \times 2$ bulk supercell, we form the surface slab by replicating the $2 \times 2 \times 2$ bulk cell along the orthorhombic z -axis. It is convenient to define a layer as comprising 8 atoms of cadmium and 8 atoms of sulfur (Figure 2.1B) lying approximately in the orthorhombic $x-y$ plane. The results reported here use an 8-layer slab supercell, $2 \times 2 \times 8$ unit cells in size, though Appendix A (section A.2.6) provides extensive convergence tests as a function of supercell dimensions. This supercell generates two equivalent, but independent, $(10\bar{1}0)$ surfaces separated by a bulk phase of CdS sandwiched between the surfaces in a “middle-out” geometry. Finally, placing a vacuum layer 30 Å thick normal to the $(10\bar{1}0)$ surface allows plane-wave basis functions and periodic boundary conditions to be applied in all directions but ensures that periodic images in the z -direction do not interact with one another.

Because Utterback *et al.*³⁰ found that the long-time transients in TA spectra assigned to trapped-hole diffusion occur in CdS nanorods with different ligands, including ligands with thiolate and phosphonate binding groups, we postulate that the details of the ligand chemistry are of secondary importance and employ pseudohydrogen potentials^{65,66} to all surface cadmium sites. These potentials simply saturate the dangling bonds on cadmium atoms, which are the sites that ligands bond to in most syntheses. While pseudohydrogen

potentials make the calculations presented here feasible, they leave us unable to comment on how ligand groups that were not explored in Ref. [30] might influence trapped-hole diffusion. To model the appropriate experimental systems, we leave surface sulfur atoms unpassivated. We then find the equilibrium nuclear positions for the slab by minimizing the energy, changing atomic positions at fixed supercell dimensions. The positions of the atoms in the middle two layers of the slab remain fixed during surface relaxation to simulate a rigid bulk region, though after relaxation the constraint forces on these atoms are zero to within accepted tolerance (23 meV/Å). This implies that the middle two layers appear approximately as bulk to the other atoms, whose positions we allow to change until their atomic forces have magnitudes less than 10 meV/Å.

Figure 2.2A shows the total density of states (DOS) of the slab around the Fermi energy, E_F . In these calculations, E_F identifies the energy at which the bands become half filled, similar to E_F in a metal at finite temperatures. At energies below E_F , the electron population dominates, while at energies above E_F , the hole population dominates. The inset to the DOS in Figure 2.2A shows the region above E_F but below the band gap, representing the lowest-energy hole states. Figure 2.2B shows the orbital density corresponding to the lowest-energy hole states, which are clearly localized to the surface. This orbital density looks like it could be formed from a linear combination of sp^3 hybridized orbitals, centered at the sulfur atoms located on the surface. Indeed, as we will show below, this observation provides the basis for a quantitative tight-binding model for the surface hole states. Constraining the energy window to lie within $k_B T = 25$ meV above or below E_F , to focus on the thermally accessible hole states, does not change the picture for the orbitals in Figure 2.2B qualitatively.

Other electronic structure calculations of small CdS and CdSe clusters have reported that hole states are localized to the sulfur atoms on the surface, in agreement with this work.^{37,42,43,61} Unlike those calculations, however, our hole states are not well-separated from the bulk DOS but rather form a continuum with the highest fully occupied (by electrons) states. This result is consistent with the experimental work of Mooney *et al.*,⁶⁰ which finds

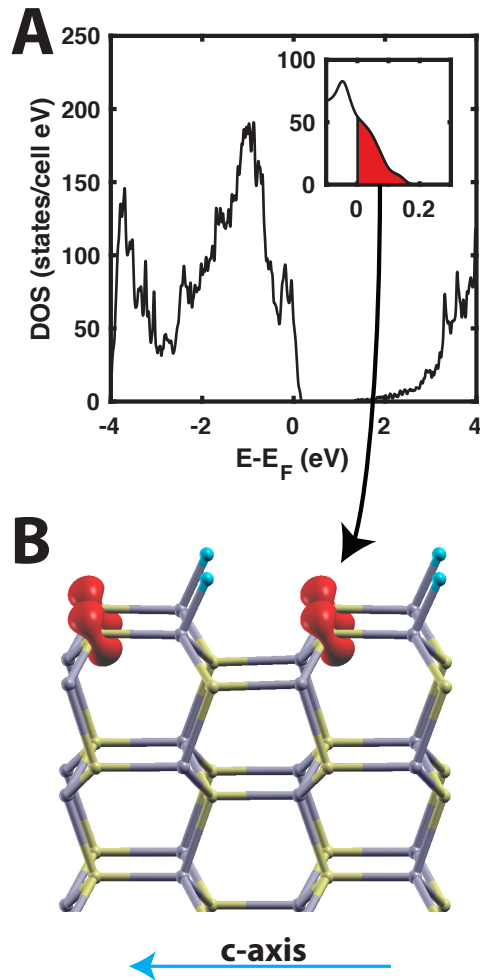


FIGURE 2.2: (A) Total density of states (DOS) for the $2 \times 2 \times 8$ slab supercell, showing states within the range $E_F \pm 4$ eV, where E_F is the Fermi energy. The inset focuses on the states above E_F that are unoccupied at zero Kelvin and are therefore hole states. (B) The hole-state density (red) corresponding to the energy range in the red part of the inset above shows that holes are localized to the sulfur atoms on the surface. Only the top 2.5 layers of the supercell are shown. Focusing on the thermally accessible hole states in the energy range within $k_B T = 25$ meV above or below E_F exhibits a similar density.

that bulk and surface states can be separated by merely tens of millielectronvolts.

The continuous density of states in the vicinity of the highest occupied valence bands, shown as the inset in Figure 2.2A, implies that holes prepared in the bulk rapidly move to the surface, lowering their energy by accessing a tier of intermediate states that are separated by infinitesimally small amounts of energy. This result supports experimental reports on CdS nanocrystals, which find that hole trapping to the surface occurs on the time scale of

picoseconds.^{30,48,50,55,59}

At first blush, the data in Figure 2.2 seem to imply that the hole states are delocalized across sulfur atoms on the surface. But one must keep in mind the limitations of adiabatic electronic structure theory, which gives the solutions to the electronic structure problem in the Born-Oppenheimer approximation at zero absolute temperature. Similar to constructing molecular orbitals from linear combinations of atomic orbitals, if two orbitals are coupled, even weakly, DFT will yield adiabatic states that are delocalized superpositions.⁶⁷ However, if the electronic coupling is weak relative to the coupling between the electrons and the environment, this delocalization will not survive decoherence from thermal fluctuations at finite temperature.^{15,68} Thermal decoherence in the electronic space will produce localized states that, while not eigenstates of the electronic Hamiltonian, more closely resemble the eigenstates of the system plus the environment.

2.3.2 Wannier Localization

The calculations presented here do not explicitly include solvent, ligand, or electron–phonon coupling. While it is computationally infeasible to include them directly into the electronic structure calculations, we can include their effects by constructing a model Hamiltonian. We begin by quantizing the electron density in terms of the sp^3 orbitals on all sulfur atoms. This leads to a tight-binding Hamiltonian, \mathcal{H}_{TB} , whose diagonal elements are the on-site energies, $\{\epsilon_\alpha\}$, and the off-diagonal elements are the tunneling matrix elements, $\{t_{\alpha,\beta}\}$. The subscripts denote the sp^3 orbitals of the sulfur atoms. We use Wannier localization⁶⁹ to generate these orbitals and compute the matrix elements. Figure 2.3 shows that, indeed, diagonalizing \mathcal{H}_{TB} and forming the two-dimensional band structure for the directions conjugate to the x – y orthorhombic axes yields a band structure that is indistinguishable from the adiabatic solution to the electronic structure near the valence band maximum, where the surface hole states dominate.

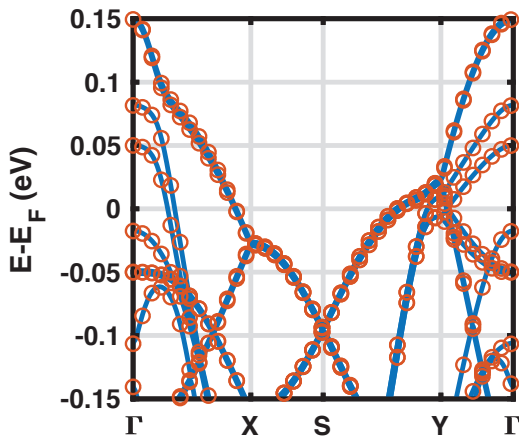


FIGURE 2.3: Band structure of the surface slab near the Fermi energy, E_F . The original bands generated directly from DFT (blue lines) and the band structure from the eigenvalues of \mathcal{H}_{TB} (orange circles) are overlaid to emphasize the accuracy of the Wannier localization procedure and the choice of sulfur sp^3 orbitals as the basis set for \mathcal{H}_{TB} . Symmetry points match the reciprocal directions of the x - y plane in the orthorhombic cell. The chosen energies include the energy range specified in the inset to the DOS in Figure 2.2A, which is dominated by surface sulfur states.

At zero temperature and in the absence of electron–phonon coupling, the adiabatic solution corresponding to the eigenvalues and eigenstates of \mathcal{H}_{TB} would be an accurate solution to the electronic problem. However, the energies of the relevant tunneling matrix elements for hole transport, described in more detail below and reported in detail in Appendix A (Table A.1), are on the order of or smaller than $k_B T$ at room temperature, implying that thermal fluctuations of the nuclei do indeed destroy coherence between orbitals and collapse the band structure in Figure 2.3.^{15,70}

To construct a model Hamiltonian that captures these effects at the level of a linear response theory, we project out the surface sulfur atoms from \mathcal{H}_{TB} , giving an effective two-dimensional tight-binding Hamiltonian for the holes on the surface, \mathcal{H}_S . The system–bath Hamiltonian, \mathcal{H}_{S-B} , which couples the surface electronic degrees of freedom to the phonons, ligands, and solvent, is linear in the electron density, $\mathcal{H}_{S-B} = -\int d\mathbf{r} \rho(\mathbf{r}) \Phi(\mathbf{r})$, where $\Phi(\mathbf{r})$ is the electrostatic potential of the nuclei.^{15,70} The electron density, quantized in the mutually orthogonal Wannier sp^3 orbitals, $\{\psi_n(\mathbf{r})\}$, is $\rho(\mathbf{r}) = \sum_n c_n^\dagger c_n |\psi_n(\mathbf{r})|^2$. Assuming that all nuclei undergo harmonic vibrations about their equilibrium positions and expanding $\Phi(\mathbf{r})$

to linear order in all bath modes leads to the Holstein small-polaron Hamiltonian, where the nuclear motions comprise a heat bath,

$$\mathcal{H} = \sum_{\langle\langle m,n \rangle\rangle} \epsilon_m c_m^\dagger c_m + t_{m,n} c_m^\dagger c_n + t_{n,m} c_n^\dagger c_m + \sum_{n,\nu} \lambda_\nu^n (a_\nu^\dagger + a_\nu) c_n^\dagger c_n + \sum_\nu \hbar\omega_\nu a_\nu^\dagger a_\nu. \quad (2.1)$$

Here, c_m^\dagger (c_m) is the Fermionic creation (annihilation) operator that puts (removes) a hole in orbital m , a_ν^\dagger (a_ν) the bosonic creation (annihilation) operator for bath mode ν , λ_ν^n the coupling matrix element between mode ν and electronic orbital n , and $\hbar\omega_\nu$ the energy of bath mode ν . The sum over m and n goes over nonbonding orbitals of nearest- and next-nearest-neighbors on the surface. Figure 2.4A shows one of these orbitals.

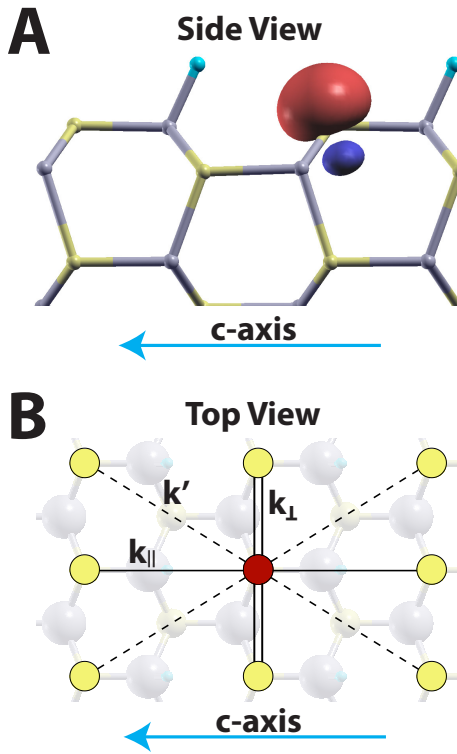


FIGURE 2.4: The relevant states used to construct the effective tight-binding Hamiltonian for surface holes. (A) Side view of a nonbonding sp^3 orbital centered on a surface sulfur atom of the slab supercell. (B) Top-down view of the surface layer with hole sites highlighted by colored circles. A hole that exists at the center position (red) can hop to any of the 8 labeled sites (yellow). The rates k_{\parallel} (single solid lines) and k' (dashed lines) contribute to the diffusion constant for hole hopping down the crystal c -axis. The sulfur atoms connected by the single black lines are separated by $c = 6.84 \text{ \AA}$.

2.4 Results and Discussion

The relevant tunneling matrix elements for hole transfer down the crystal c -axis are t_{\parallel} and t' , corresponding to the tunneling matrix elements between nearest- and next-nearest-neighbors along the rod axis, respectively (Figure 2.4B). Our calculations for t_{\parallel} and t' yield $|t_{\parallel}| \approx |t'| \approx 3$ meV. These small values for the tunneling matrix elements, compared to both room-temperature $k_B T$ and to characteristic values for λ_{ν}^n ,^{15,70} place this system squarely in the weak electronic coupling limit, where bath fluctuations destroy the band structure and localize holes to orbitals on individual sulfur atoms. In this limit, the hole populations on the surface sites obey the quantum master equation,

$$\frac{dP_m(t)}{dt} = \sum_n k_{n \rightarrow m} P_n(t) - \sum_n k_{m \rightarrow n} P_m(t), \quad (2.2)$$

where $P_m(t)$ is the probability of being at site m at time t , and the rates $k_{n \rightarrow m}$ are given by the Golden Rule, $k_{n \rightarrow m} \sim |t_{m,n}|^2$. In the high-temperature limit, which is the simplest approximation, bath energies are much less than $k_B T$, and the detailed spectrum of the heat bath is irrelevant. One then recovers the Marcus expression⁷¹ for nonadiabatic hole transfer between degenerate states,

$$k_{n \rightarrow m} = \frac{|t_{m,n}|^2}{\hbar} \sqrt{\frac{\pi}{\lambda k_B T}} \exp\left\{-\frac{\lambda}{4k_B T}\right\}, \quad (2.3)$$

where $\lambda = \sum_{\nu} \frac{(\lambda_{\nu}^n - \lambda_{\nu}^m)^2}{\hbar \omega_{\nu}}$ is the reorganization energy. As implied earlier by our notation, t_{\parallel} and t' correspond to the rates k_{\parallel} and k' , respectively (Figure 2.4B). Finally, an asymptotic expansion of Eq. 2.2, presented in Appendix A (section A.1), gives a Fokker–Planck approximation to the master equation, which is an anisotropic diffusion equation. The diffusion constant for hole hopping along the axis of the nanorod, D_{\parallel} , is

$$D_{\parallel} = c^2(k_{\parallel} + 2k'), \quad (2.4)$$

where $c = 6.84 \text{ \AA}$ is the surface sulfur-to-sulfur distance parallel to the long axis of the nanorod. Note that k' , the hopping rate along the diagonal line connecting next-nearest-neighbors (Figure 2.4B), makes a significant contribution to D_{\parallel} . The factor of 2 in Eq. 2.4 reflects the fact that there are two next-nearest-neighbors for each nearest-neighbor on the rectangular lattice, in the direction of the crystal c -axis.

Calculating λ is not an objective of this work, nor is it computationally feasible in a system of this size. Without a value for λ , we cannot compute the diffusion constant D_{\parallel} , but we can use our computed hopping matrix elements, $|t_{\parallel}| \approx |t'| \approx 3 \text{ meV}$, in conjunction with experimental data to bound the value of λ . Utterback *et al.*³⁰ measured an upper bound for D_{\parallel} to be $\sim 10^{-7} \text{ cm}^2 \text{s}^{-1}$. From this bound on D_{\parallel} and our calculated values of t_{\parallel} and t' , we use Eq. 2.3-2.4 to find a lower bound for λ of 1 eV. This value of λ is large for electron-transfer reactions in solution but not uncommon for polaron hopping transport in polar semiconductors, where lattice phonons couple strongly to the electronic degrees of freedom.^{60,72} Similarly, the high-temperature approximation to the system–bath coupling, while appropriate for a wide class of electron-transfer reactions in solution, may need to be revised as more information about the specific coupling to lattice phonons and to nuclear distortions of the ligands becomes available. The tunneling matrix element for hopping perpendicular to the crystal c -axis, $|t_{\perp}| \approx 80 \text{ meV}$ (Figure 2.4B), is about an order of magnitude larger than t_{\parallel} . Because it is still much smaller than λ , the holes still remain small polarons localized to atomic sites, not delocalized around the waist of the rod.

2.5 Conclusions

In summary, we have presented an atomistic computational model to capture the electronic structure of the bulk and surface states of CdS nanorods. The adiabatic solution to the electronic structure of this surface slab clearly shows hole states, near the Fermi energy, that are localized to the undercoordinated sulfur atoms on the surface. Our results show

that the hole states of a CdS surface slab form a near continuum with the bulk states of electrons, a result that differs from previous theoretical work on small quantum dots,^{37,42,43,61} but is consistent with recent experimental work of Mooney *et al.*⁶⁰ The continuous density of states between holes and electrons presented here would rationalize a wealth of experimental data that finds holes prepared in the bulk relax quickly to the surface.^{30,48,50,55,59}

Motivated by the adiabatic electronic structure results, we parametrize a model tight-binding Hamiltonian from the sp^3 orbitals centered on sulfur atoms. The calculated tunneling matrix elements between relevant sulfur orbitals on the surface are small relative to the estimated reorganization energy, so that thermal fluctuations and nuclear motions localize holes into small polarons, trapped in nonbonding sulfur orbitals on the surface. While we cannot rule out hole hopping through a superexchange mechanism, mediated through virtual bulk or ligand states, it is notable that this mechanism need not be invoked. Because hole-trap states in CdS nanocrystals made by conventional syntheses are so deep in the weak electronic coupling regime, trapped-hole transport in these particles is slow at room temperature. Our results give direct support for the picture presented by Utterback *et al.*,³⁰ who hypothesized that holes diffuse by hopping on length scales comparable to interatomic spacings.

2.6 Computational Details

The DFT calculations employed the Vienna Ab initio Simulation Package,^{73–76} a plane-wave electronic structure code. We used the projector augmented wave method with the Perdew–Burke–Ernzerhof generalized gradient approximation for the exchange–correlation functional,^{77,78} which for CdS strikes a reasonable balance between computational feasibility and accuracy. The cadmium $5s^24d^{10}$ and sulfur $3s^23p^4$ electrons were treated explicitly in all calculations. To analyze the results of the electronic structure calculation in the framework of

nonadiabatic polaron theory, we employed a localization procedure using Wannier90.⁶⁹ Wannier90 encompasses a method for obtaining maximally localized Wannier functions (MLWFs) from the adiabatic Bloch states, and it computes these MLWFs according to the method of Marzari and Vanderbilt.^{79,80} We used the XCrySDen⁸¹ software to visualize all structures, wave function densities, and Wannier functions.

2.7 Appendix A Contents

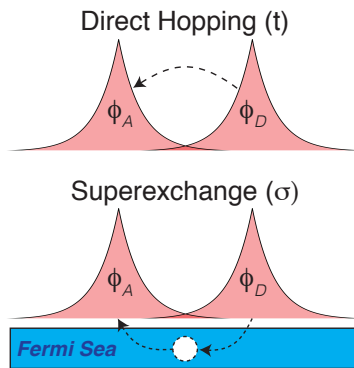
Derivation of the diffusion constants from the hopping rates; crystal structure parameters; bulk and surface convergence details; surface construction details; Wannier localization procedure details; additional figures.

2.8 Acknowledgement

This material is based upon work supported by the National Science Foundation under Grant No. CHE-1455365. This work utilized the RMACC Summit supercomputer, which is supported by the National Science Foundation (Awards ACI-1532235 and ACI-1532236), the University of Colorado Boulder, and Colorado State University. The Summit supercomputer is a joint effort of the University of Colorado Boulder and Colorado State University. J.K.U. and S.E.S. acknowledge support from National Science Foundation Graduate Research Fellowships under Grant No. DGE-1144083. G.D. acknowledges support from Air Force Office of Scientific Research under AFOSR award No. FA9550-15-1-0253.

Chapter 3

Surface-Trapped Hole Diffusion in CdS and CdSe: The Superexchange Mechanism[†]



3.1 Abstract

In contrast to the conventional view that surface-trapped holes in CdS and CdSe nanoparticles are static and immobile, recent experimental and theoretical work have shown that these holes are dynamic and undergo diffusion along the surfaces of these particles. We present semi-periodic density functional theory calculations for nanocrystal surfaces of these materials and employ Green's function methods to assess the mechanisms of trapped-hole diffusion. Bulk electronic states can serve as intermediate virtual states that link the donor and acceptor hole traps on the surface. The associated superexchange tunneling mechanism dominates over the conventional direct tunneling pathway. The methodology presented in

[†]Adapted with permission from Cline, R. P.; and Eaves, J. D. Surface-Trapped Hole Diffusion in CdS and CdSe: The Superexchange Mechanism, *submitted for publication*.

this work is non-perturbative in nature and should be applicable to a wide range of other nanoscale problems in which underlying phenomena are strongly influenced by coupling to a dense manifold of electronic states.

3.2 Introduction

Cadmium-chalcogenide nanocrystals are among the most well-studied systems in nanoscience.^{20,21} But their surfaces are rife with complexity, and the impact of surface states on the dynamics of photoexcited carriers remains an area of active research.^{28–33} Photoexcited holes in these materials can trap rapidly to undercoordinated chalcogen atoms on the surface.^{19,31,34–36,38–43,49} The first direct evidence that trapped holes are mobile comes from transient absorption spectra of CdS nanorods where the electron and hole can spatially separate.³⁰ The authors were able to explain the experimental data by positing a diffusion–annihilation model, where the surface-trapped hole undergoes a one-dimensional random walk on the nanocrystal surface before recombining with an electron. The power-law decay characteristic of the one-dimensional diffusion–annihilation model has since been observed in CdSe nanorods and heterostructures,³² and it has proven to be insensitive to ligand type, solvent, and nanorod length.^{30,32,33} Just as the diffusion–annihilation model would predict, the exponent of the power-law decay has been found to be invariant to temperature.³³

Motivated by the original finding³⁰ in CdS nanorods, we used microscopic electronic structure density functional theory (DFT) calculations on semi-periodic surfaces of CdS (Chapter 2).³¹ These calculations confirmed that holes localize to undercoordinated sulfur atoms on the surface. Activated by nuclear motion, these holes perform a random walk through a series of incoherent hops on the surface. We showed that an effective one-dimensional diffusion constant can be calculated using nonadiabatic small polaron theory and that the diffusion constant is proportional to the absolute value squared of an effective tunneling amplitude.³¹

More recent experimental measurements have measured the transient absorption spectra

on CdS and CdSe nanocrystals through a range of temperatures.³³ These new temperature-dependent data can be analyzed to estimate the effective tunneling amplitudes for one-dimensional diffusion, which are on the order of 10-100 meV. This is roughly an order of magnitude larger than what our previous calculations (Chapter 2) gave for the direct pathway.³¹ In this work, we show that superexchange, where holes first hop into a dense tier of bulk electronic states before localizing back to the surface, can explain much of the discrepancy between our earlier predictions and the extracted hole-hopping amplitudes for CdS and CdSe.

The superexchange calculation in these materials, however, is far from trivial. It is complicated by the fact that there are many band-like states that lie close in energy to the initial and final states. This means that second-order perturbation theory cannot be used to compute superexchange tunneling amplitudes. To solve this problem, we transform the hole-hopping problem into two uncoupled but exactly solvable problems for the hole Green's function. The solution to this pair of problems is accurate to all orders in perturbation theory, and shows that virtual states dress the hole tunneling amplitudes substantially. The superexchange corrections increase the effective tunneling matrix element by roughly an order of magnitude, bringing them into quantitative agreement with experimental estimates.

As we have previously shown (Chapter 2),³¹ the effective one-dimensional diffusion constant can be calculated by computing the tunneling couplings between two inequivalent pairs of sites on the surface taken one pair at a time. We call the chosen pair $|D\rangle$ and $|A\rangle$ for the hole donor and hole acceptor, respectively. If we consider for a moment a single hopping event and neglect interactions between the surface and bulk orbitals, we arrive at a “bare” 2×2 hopping Hamiltonian,

$$\mathbf{H}_{\text{hop}} \doteq \begin{pmatrix} \epsilon_0 & t_{DA} \\ t_{AD} & \epsilon_0 \end{pmatrix}, \quad (3.1)$$

for any pair of donor (D) and acceptor (A) orbitals on the surface. With the electronic problem given by single-particle orbitals and energies of the full Hamiltonian, H , the matrix

element $\epsilon_0 = \langle A|H|A \rangle = \langle D|H|D \rangle$ denotes the on-site energy, and $t_{DA} = \langle D|H|A \rangle$ is the bare or direct tunneling amplitude. All other off-diagonal terms are set to zero.³¹ At this level of description, no other states are coupled to the donor or acceptor, so only t_{DA} allows direct tunneling between trap sites.

However, if we adiabatically turn on the interactions between each of the hole trapping sites and the bulk states, there are conditions under which the orbital energies shift and the couplings renormalize to their effective or “dressed” values. The dressed Hamiltonian for the surface traps becomes

$$\tilde{\mathbf{H}}_{\text{hop}} \doteq \begin{pmatrix} \tilde{\epsilon}_0 & \tilde{t}_{DA} \\ \tilde{t}_{AD} & \tilde{\epsilon}_0 \end{pmatrix}, \quad (3.2)$$

We use tildes to denote dressed parameters. In nonadiabatic small polaron theory, the hole-hopping rate between a pair of trap sites on the surface, which is proportional to the diffusion constant, goes as $|\tilde{t}_{DA}|^2$. The difference between the bare and dressed couplings is due to the superexchange mechanism, where holes tunnel into the band and then into the donor trap site. A second-order perturbation calculation would calculate the superexchange contribution by allowing one such event per band state, but it turns out that second-order perturbation theory fails for this problem. We will show how to compute the renormalized tunneling couplings, \tilde{t}_{DA} , to infinite order in perturbation theory by mapping the problem into a pair of exactly solvable quantum impurity problems.

3.3 Methods

To obtain the Hamiltonian in Eq. 3.1, we use semi-periodic density functional theory (DFT) calculations to find adiabatic ground-state electronic structures and corresponding atomic configurations. From the adiabatic orbitals, we then transform into a diabatic representation where the holes are localized to molecular orbitals on the chalcogen atoms. From the diabatic Hamiltonian, we apply Green’s function methods to turn the bare Hamiltonian

in Eq. 3.1 into the dressed Hamiltonian in Eq. 3.2, thereby computing the renormalized tunneling couplings.

3.3.1 DFT Calculations

The construction of the nanorod follows closely from our previous work (Chapter 2),³¹ and details of the calculations specific to CdSe are located in Appendix B (section B.1). An illustration of the nanorod and a cross section appear in Figure 3.1A. The cross section shows the configuration of atoms in the interior and on the two opposing surfaces, where the trap sites lie. These surfaces correspond to the $(10\bar{1}0)$ Miller-Bravais facet for both CdS and CdSe. Experimentally, the nanorod thickness is about 13 layers of material for CdS and 23 layers of material for CdSe, or 4.2 and 8.1 nanometers, respectively.^{30,32} We have found convergence using 8 layers of material to model the bulk phase (see Appendix B, section B.1.2.3). These are large DFT calculations — the $2 \times 2 \times 8$ surface slab supercell reported in this work corresponds to a semi-periodic simulation of 136 atoms and 1164 electrons.

We use the Vienna Ab initio Simulation Package (VASP) for all of the DFT calculations and XCrySDen to visualize the molecular structures and orbital densities.^{73–78,81} Our calculations employ the projector augmented wave (PAW) method for the atomic potentials and the Perdew-Burke-Ernzerhof (PBE) generalized gradient approximation for the exchange-correlation functional.^{77,78} Pseudohydrogen potentials mimic the effect of ligands and passivate the Cd atoms on the surface. While this choice leaves us unable to comment on ligand-specific effects, a body of work suggests that many ligands play only a minor role in trapped-hole diffusion.^{30–32,65,66} For all non-hydrogen atoms, we use the PAW PBE pseudopotentials to explicitly treat the $(5s)^2(4d)^{10}$, $(3s)^2(3p)^4$, and $(4s)^2(4p)^4$ electrons for cadmium, sulfur, and selenium, respectively.

Having presented CdS in Chapter 2,³¹ we focus here on the electronic structure of the CdSe surface slab. Figure 3.1B shows the total density of states (DOS) for our model CdSe surface slab near the Fermi energy, E_F . The inset shows the region directly above E_F and

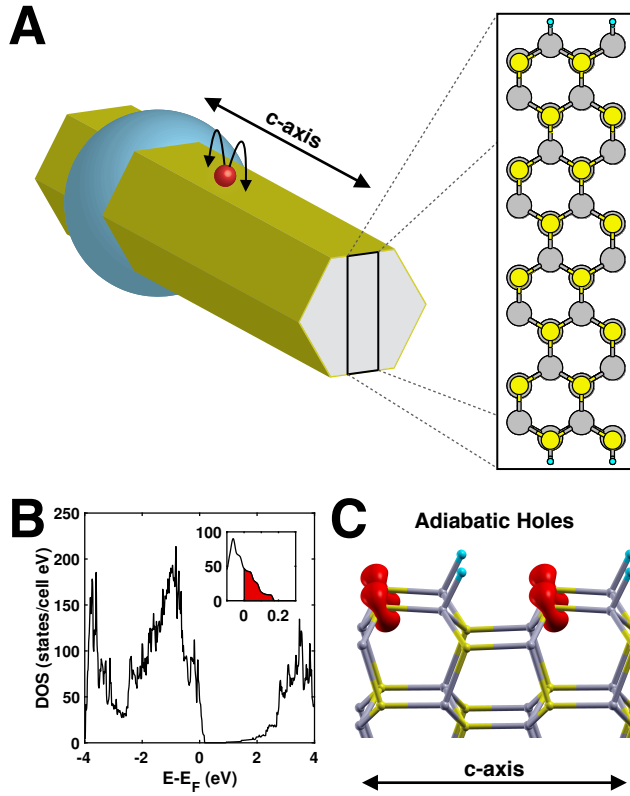


FIGURE 3.1: (A) Illustration and cross section of a cadmium-chalcogenide nonuniform nanorod. The surface-trapped hole on the rod part is represented as a small red sphere, and the electron localized in the wider bulb part is represented as a larger blue sphere. All six radial surfaces of the nanocrystal correspond to the same $(10\bar{1}0)$ Miller-Bravais facet. The cross section shows the configuration of atoms in the interior and on opposing surfaces of a crystal comprising 8 layers of material. The crystal c -axis runs parallel to the long axis of the nanorod. This axis also corresponds to the direction of the one-dimensional diffusion measured by Utterback *et al.*^{30,32,33} (B) Total density of states (DOS) for the $2 \times 2 \times 8$ CdSe surface slab, showing states within the range $E_F \pm 4$ eV, where E_F is the Fermi energy. The inset focuses on the hole states directly above E_F , which are unoccupied at zero Kelvin and zero charge. (C) The hole-state density (red) corresponding to the lowest energy holes depicted in the inset of (B) shows holes are localized to the selenium atoms on the surface. For clarity, only the top 2 layers of the surface slab are shown.

below the band gap, corresponding to the lowest-energy hole states. Figure 3.1C shows the wave function density for these hole states, which are centered at the surface selenium atoms and delocalized across the surface. As with our previous results for CdS (Chapter 2),³¹ the existence of a continuum of states about E_F is consistent with the work of Mooney *et al.*,⁶⁰ particularly that the bulk and surface states of these materials can be separated by tens of millielectronvolts. A nanoparticle with the electronic filling and energy-level structure

corresponding to Figure 3.1B will readily acquire electrons from the environment, placing them on the surface chalcogen atoms. This is consistent with basic chemical intuition, which would place a negative formal charge on the chalcogen atoms. Just like in CdS, the gapless separation in CdSe between the surface trap sites and the continuum of states in the band implies that there will be a rapid and efficient energetic driving force to trap the holes to the chalcogen atoms on the surface.

3.3.2 Wannier Localization

The DFT results represent the zero-temperature, Born-Oppenheimer, adiabatic solutions to the problem. The apparent delocalization of the adiabatic hole states across the surface will not survive decoherence from nuclear thermal fluctuations at finite temperature if the coupling between the hole states, in a localized atomic-orbital picture, is weak relative to the electron-nuclear coupling.^{15,68} Thus, we fix the nuclei at their ground-state positions and transform the adiabatic orbitals into a diabatic representation. We accomplish this by using a Wannier localization procedure^{69,79,80,82,83} to find an appropriate set of maximally localized, mutually orthogonal, diabatic states from which we compute the couplings between surface orbitals. Strictly speaking, the nuclei should be allowed to equilibrate in the diabatic hole state. While that would change the on-site energy, ϵ_0 , it would not change the inter-site tunneling coupling in the Condon approximation. The localization procedure leads to a tight-binding Hamiltonian, and one can demand self-consistency in the localization procedure by requiring that the band structure produced by the tight-binding Hamiltonian matches that of the DFT calculation.

One has to place high demands on the localization procedure to get an accurate description of the interaction between the surface-localized trap states and the bulk states. The conventional “entangled band” methodology⁸⁰ that we employed in Chapter 2 is insufficient. In that work, the entangled band method achieved the maximally-localized description of the surface orbitals with minimal selection bias. But this method limits the energy range over

which the band structure of the localized Hamiltonian matches the DFT calculation, and it is not accurate for evaluating the higher-order superexchange corrections to the matrix elements that we present here.

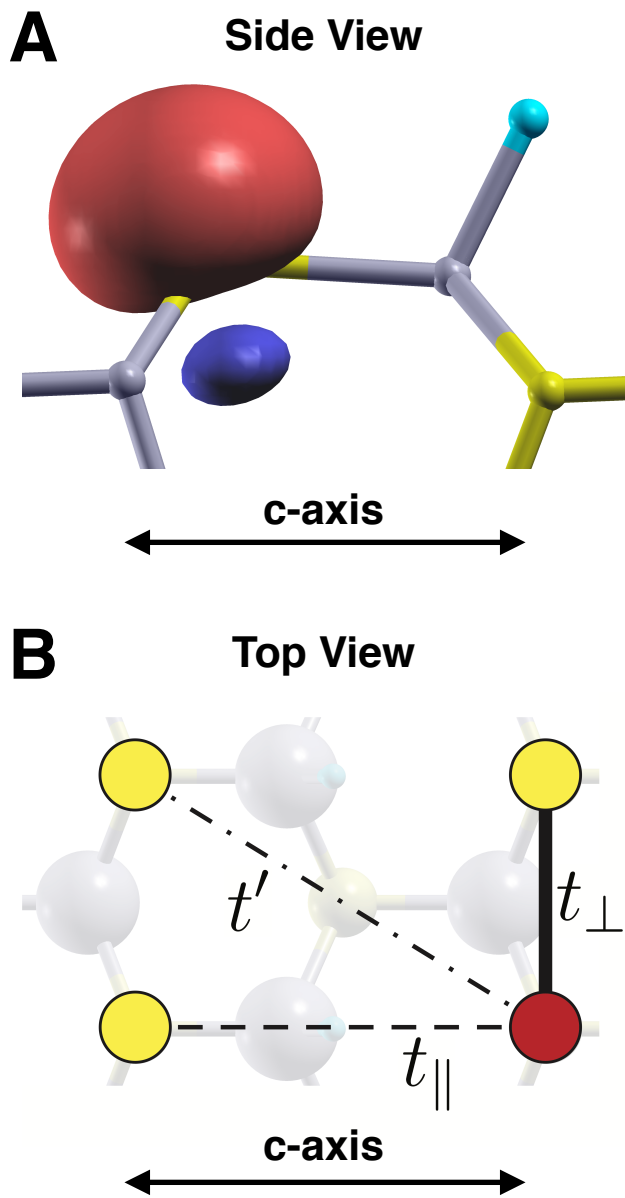


FIGURE 3.2: The relevant orbitals and tight-binding grid for surface-trapped holes. (A) Close-up of a converged nonbonding sp^3 orbital on the surface of a CdSe slab, pointing in the direction of the missing bond. (B) Top-down view of the surface layer, with surface hole sites highlighted by colored circles. In our model, a hole positioned at the red circle can hop in 3 distinct ways: down the crystal c -axis of the nanocrystal (t_{\parallel} , dashed line), perpendicular to the crystal c -axis (t_{\perp} , solid line), or diagonally (t' , dot-dashed line). Only the t_{\parallel} and t' matrix elements contribute to trapped-hole diffusion in the nanorods studied by Utterback *et al.*^{30,32,33} In the text, we refer to acceptor and donor states as any pair of trap states, taken two at a time, with one red state and one yellow state.

In the DOS for CdSe (Figure 3.1B), the adiabatic hole density lies in close proximity to the dense manifold of valence bands in the energy window $-4 \lesssim E - E_F < 0$ eV that is mostly comprised of chalcogen p orbitals (Figures B.9 and B.13). There will be strong mixing between the trap states and these bulk-like band states. Therefore, we demand that *all* of the adiabatic states in this wide energy window — both surface and bulk states — are reproduced in the Wannier localization procedure.

One can, in principle, “freeze” eigenvalues in a window during the Wannier localization process, but this leads to an over-parameterization of the resulting diabatic Hamiltonian. Such a protocol leaves too few bands to approximate the “unfrozen” band structure outside of the “frozen” energy window. The agreement between the band structure of the tight-binding Hamiltonian and the DFT band structure outside of the frozen energy range becomes increasingly poor, particularly near the bands dominated by the chalcogen s orbitals (Figure B.5). The on-site energies of the hole traps are sensitive to selection bias for frozen and unfrozen windows (Figure B.4), which can lead to problems in the Green’s function formalism (see Appendix B, section B.4.1).

To circumvent these issues, we first explicitly exclude all occupied bands dominated by the cadmium d orbitals (Figures B.6 and B.10) and all conduction band states with energies $E - E_F > 0.2$ eV. We include all other states from the DFT calculation when constructing the Wannier orbital basis for both CdS and CdSe. This means we initialize the localization procedure with four sp^3 orbitals per chalcogen atom and one s orbital per pseudohydrogen atom to account for all included adiabatic states, which have energies $E - E_F < 0.2$ eV. We discuss our decision to include the hydrogen states in Appendix B, section B.4.2. Our approach in this work corresponds to the “composite band” method detailed in Ref. [79], and allows for the entire input band structure to be reproduced exactly. The Wannier-localization process shows that the hole traps form in the nonbonding orbital (NBO) of each surface chalcogen atom (Figure 3.2A), which is exactly what one finds using the entangled band method.³¹ These states couple with each other through their direct tunneling matrix

elements (Figure 3.2B) and to all other states in the bulk.

3.3.3 Green's Function Formalism

With an accurate diabatic description in place for both the bulk band structure and the surface traps, we project out a pair of orbitals, $|D\rangle$ and $|A\rangle$, involved in a single hopping event by defining the operators P and Q , where $P = |D\rangle\langle D| + |A\rangle\langle A|$ and $Q = \mathbf{1} - P$. While Q formally contains projections onto states of all energies, we remove projections onto states with energies outside the range depicted in Figure 3.3.

The projection operators allows the electronic Hamiltonian to be partitioned as

$$\mathbf{H} \doteq \left(\begin{array}{c|c} \mathbf{P}\mathbf{H}\mathbf{P} & \mathbf{P}\mathbf{H}\mathbf{Q} \\ \hline \mathbf{Q}\mathbf{H}\mathbf{P} & \mathbf{Q}\mathbf{H}\mathbf{Q} \end{array} \right), \quad (3.3)$$

where $\mathbf{P}\mathbf{H}\mathbf{P}$ is precisely the 2×2 bare Hamiltonian in Eq. 3.1. To cast Eq. 3.3 in the form of a system and a bath, $H = H_S + H_B + V$, we numerically diagonalize the $\mathbf{P}\mathbf{H}\mathbf{P}$ and $\mathbf{Q}\mathbf{H}\mathbf{Q}$ blocks to yield

$$\mathbf{H} \doteq \left(\begin{array}{c|c} \mathbf{H}_S & \mathbf{V} \\ \hline \mathbf{V}^\dagger & \mathbf{H}_B \end{array} \right), \quad (3.4)$$

such that $H = H_0 + V$, where $H_0 = H_S + H_B$ is diagonal, and V represents the coupling between the system and bath states. Details of this procedure appear in Appendix B, section B.3. The eigenstates of the system Hamiltonian are $|\pm\rangle = \frac{1}{\sqrt{2}}(|A\rangle \pm |D\rangle)$, and each of these states couples to bath state $|q\rangle$ through $V_{\pm,q} = \langle \pm | H | q \rangle$.

With the electronic Hamiltonian in the form of Eq. 3.4, we can immediately calculate the bare Green's function,

$$G_0(E) = \frac{1}{E - H_0 + i\epsilon}, \quad (3.5)$$

where, as usual, ϵ is a small positive number that regularizes the Laplace transform of the time evolution operator and that formally approaches 0 from the positive side at the end of

the calculation.^{15,84,85} In the numerical calculations presented here, we keep $\epsilon = 0.01$ meV to be a small but finite number. For plotting the results in Figure 3.3, we use a larger value of 25 meV. The full Green's function is

$$G(E) = \frac{1}{E - H + i\epsilon}. \quad (3.6)$$

These Green's functions are evidently operators that are to be understood as a sum over the poles that correspond to the eigenvalues of H_0 and H , for example, for $H|n\rangle = E_n|n\rangle$, $G(E) = \sum_n |n\rangle \frac{1}{E - E_n + i\epsilon} \langle n|$. $G(E)$ is related to $G_0(E)$ through the Dyson equation,

$$G(E) = G_0(E) + G_0(E)VG(E). \quad (3.7)$$

Figure 3.3 shows the results for the imaginary part of matrix elements for the bare Green's function for the adjacent pair of hole sites parallel to the long axis (*c*-axis) of the nanorod (Figure 3.2B). The poles corresponding to the resonances of the bare 2×2 , H_S , shown as red vertical lines are split by twice the very small direct coupling: $2t_{\parallel}$ for both CdS (Figure 3.3A) and CdSe (Figure 3.3B) in this example. Figure 3.3 illustrates that the usual application of second-order perturbation theory will fail for the superexchange corrections to the hole-hopping rate since the states within H_S are degenerate (Figure 3.3A) or nearly-degenerate (Figure 3.3B) with some of the bath states within H_B .

Diagonalizing the blocks corresponding to H_S and H_B leaves two uncoupled quantum impurity problems: one for the symmetric, $|+\rangle$, and one for the antisymmetric, $|-\rangle$, linear combinations of the $|A\rangle$ and $|D\rangle$ states. Each state independently couples to the continuum in the way that Fano⁸⁶ and Anderson⁸⁷ wrote about decades ago. The resulting pair of Fano-Anderson problems are *exactly* solvable, which is a rarity in quantum many-body physics.¹⁵

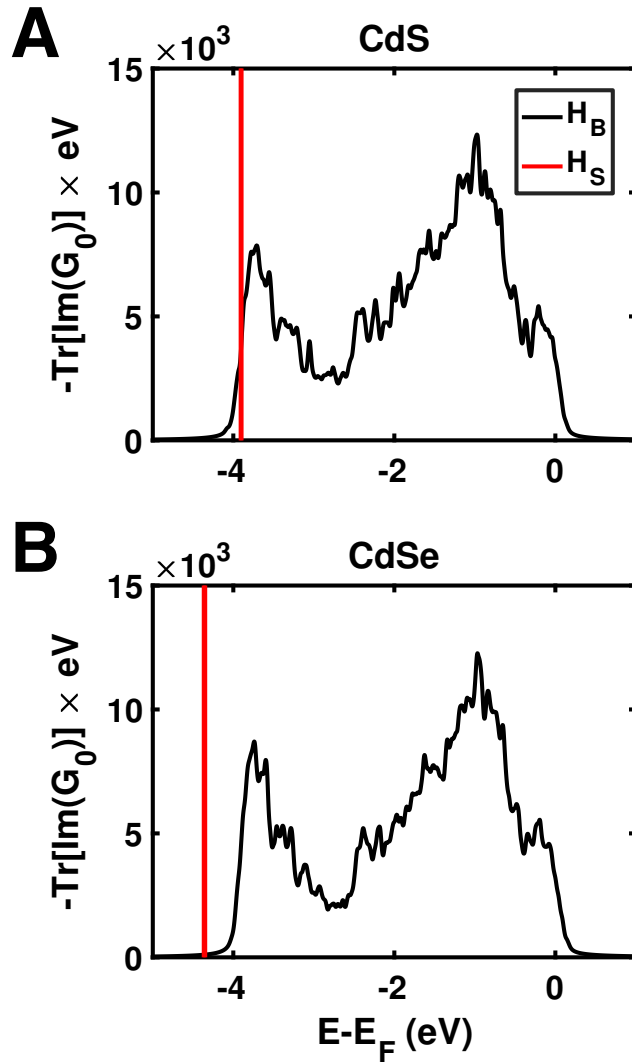


FIGURE 3.3: Trace of the negative imaginary part of the bare Green's function, Eq. 3.5, for an example hopping event for (A) CdS and (B) CdSe. The trace of $-\text{Im}[G_0(E)]$ is proportional to the bare density of states. The results shown here are nearly identical for all hopping events. Of particular interest are the states corresponding to H_S , which are degenerate (A) or nearly-degenerate (B) with the states corresponding to H_B . This invalidates conventional second-order perturbation theory as a method for calculating the superexchange corrections.

The matrix elements of the Green's functions corresponding to the impurity states follows from the Fano-Anderson model,^{15,84,85}

$$G_{\pm}(E) = \frac{1}{E - (E_{\pm} + \Sigma_{\pm}(E))}, \quad (3.8)$$

where $E_{\pm} = \langle \pm | H_S | \pm \rangle$ and

$$\Sigma_{\pm}(E) = \sum_q \frac{|V_{\pm,q}|^2}{E - E_q + i\epsilon} \theta(E_F - E_q) \quad (3.9)$$

are the self-energies for each impurity. The sum in Eq. 3.9 goes over the bath states in H_B , and $\theta(E_F - E_q)$ is the Heaviside step function that ensures only electrons below the Fermi energy contribute to the sum.

The self-energies in Eq. 3.9 describe how the poles of $G_{\pm}(E)$ shift as V turns on adiabatically slowly. In principle, the impurity sites can become metastable once they hybridize with the continuum — this would be observed as an imaginary part of the self-energy.⁸⁸ In such a case, a reduced effective 2×2 Hamiltonian like Eq. 3.2 would be impossible to write down unless one was willing to accept complex energies. But in the cases studied here, the self-energy is purely real, which makes the rewriting from Eq. 3.1 to Eq. 3.2 — and the calculation of the tunneling coupling accurate to all orders in perturbation theory — possible. We simply calculate the renormalized tunneling couplings from the difference in the self energies in Eq. 3.9.

Just as the resonances of the impurity states in the bare Green's functions, $\langle \pm | G_0(E) | \pm \rangle$, occur at $E_{\pm} = \epsilon_0 \pm t_{DA}$, the resonances of the dressed Green's function, $\langle \pm | G(E) | \pm \rangle$, occur at energies $\tilde{E}_{\pm} = \tilde{\epsilon}_0 \pm \tilde{t}_{DA}$. The dressed tunneling matrix elements are thus directly related to the splitting between the pair of poles of the full Green's function. Because the hole trap sites on the surface are chemically equivalent, their normalized bare energies, $\tilde{\epsilon}_0$, are equal, and so the renormalized tunneling coupling is directly proportional to the splitting between the poles of $G_+(E)$ and $G_-(E)$. The key result is that $\tilde{t} = \frac{1}{2}(\tilde{E}_+ - \tilde{E}_-)$ corresponds to the *total* nonadiabatic coupling between the acceptor and donor states, summed to infinite order in perturbation theory over the interactions with the bulk.^{15,84} Figure 3.4 is an energy correlation diagram that illustrates the procedure we apply to any donor/acceptor pair. Depending on the degree of hybridization of the $|\pm\rangle$ states with the continuum, \tilde{t}_{DA} either

carries the same or opposite sign as t_{DA} . Figure 3.4B shows the former case; the latter occurs when the resulting $|\tilde{-}\rangle$ state shifts below the $|\tilde{+}\rangle$ state in energy.

3.4 Results and Discussion

A perturbative calculation for the superexchange mechanism between $|D\rangle$ and $|A\rangle$ is inappropriate, but it does give some physical insights. At second-order in perturbation theory, the hole tunnels *once* into a bath state and then into the acceptor state (Figure 3.4A). The tunneling amplitude is the sum of this event taken over all bath states. While the initial and final states have the same energy, the intermediate state can be at any energy, and is thus never occupied — it is a virtual state. By analogy, the self-energy, before being cast in the form of Eq. 3.9, can be viewed as an infinite sum over *all possible* tunneling events between all virtual bath states, where the hole hops to a virtual state, and then to another one, and so on — each term corresponding to a higher-order perturbation — before arriving at the acceptor. It is a remarkable fact that an infinite sum over all such sequences converges, but that is what makes the Fano-Anderson model exactly solvable.

The poles of the dressed $G_{\pm}(E)$ lie outside of the continuum and thus correspond to well-localized stable states; the self-energy is real to numerical precision. The *dressed* diabatic couplings increase by about an order of magnitude compared to the *undressed* direct couplings (Table 3.1), but they are not so large that they imply that a stable coherence forms between the two sites. We know from experimental data that the reorganization energy is about an order of magnitude larger, and so nuclear motions at finite temperature would destroy such a putative coherence.³³ The superexchange correction is an important but quantitative one that does not change the overall picture: the surface-trapped holes are still nonadiabatic small polarons.

In the Appendix for Chapter 2 (section A.1),³¹ we derived an effective one-dimensional diffusion constant along the crystallographic c -axis of the nanocrystal, $D_{\parallel} \propto (k_{\parallel} + 2k') = k_{\text{eff}}$,

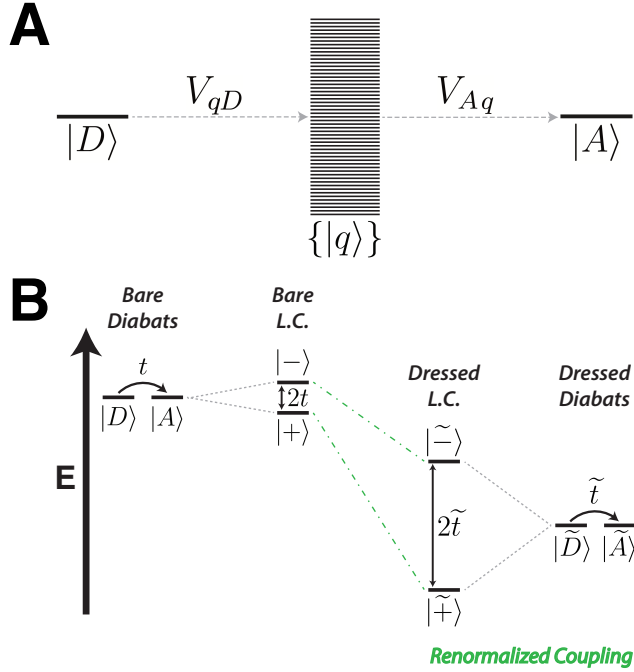


FIGURE 3.4: Energy correlation diagram for a pair of donor/acceptor surface states. (A) At the level of second-order perturbation theory, a trapped hole in the donor orbital could tunnel into a virtual hole state, $|q\rangle$, with amplitude V_{qD} and then appear in the acceptor orbital with amplitude V_{Aq} . The Green’s function calculation presented here allows for tunneling between all virtual states along the pathway between donor and acceptor. (B) To use Green’s functions to quantify the effect of tunneling through virtual states, we must first numerically diagonalize the bare 2×2 to form the uncoupled linear combinations (L.C.) of the degenerate donor/acceptor orbitals. These new states are separated by $2t$ in energy. We then apply Eq. 3.8-3.9 to these states (green dot-dashed lines) to quantify their interactions with the bath states, $\{|q\rangle\}$. The result is the bare L.C. states become dressed due to these interactions, and their energies shift such that their new separation is $2\tilde{t}$. Undiagonalizing these dressed L.C. states yields two dressed diabats coupled by \tilde{t} , which is accurate to all orders in perturbation theory.

with the rates, k_{\parallel} and k' , given by the Marcus expression for nonadiabatic hole transfer between degenerate states, or the equivalent high temperature limit of the Holstein small polaron theory. Since we only considered the direct mechanism in that work, we found that $k_{\text{eff}} \propto |V_{\text{eff}}|^2 = |t_{\parallel}|^2 + 2|t'|^2$. With the superexchange corrections calculated here, the analogous tunneling matrix elements are $|\tilde{V}_{\text{eff}}|^2 = |\tilde{t}_{\parallel}|^2 + 2|\tilde{t}'|^2$. Introducing the variable σ to denote the superexchange correction to each direct matrix element t , we further define $\tilde{t}_{\parallel} = t_{\parallel} + \sigma_{\parallel}$ and $\tilde{t}' = t' + \sigma'$. Quantum superposition theory dictates that these terms sum coherently; the direct and superexchange mechanisms can interfere. But because the

values of the two amplitudes are so different, the pathway interference is minimal. Recent temperature-dependent data on CdS and CdSe nanorods have found a value of V_{eff} between 10-100 meV. With superexchange corrections included, our results are remarkably consistent with those values.

Table 3.1 summarizes our findings for CdS and CdSe. The values for the direct matrix elements for CdS ($|t_{||}| \approx |t'| \approx 5$ meV) are slightly different than those presented in Chapter 2 ($|t_{||}| \approx |t'| \approx 3$ meV) due to the change in procedure for the Wannier localization applied here. The direct matrix elements for CdSe are within a factor of two compared to those of CdS. The superexchange tunneling couplings for either material are up to an order of magnitude larger than their respective direct couplings, suggesting that tunneling into the virtual hole states is the primary mechanism for diffusion hopping in both of these materials. One notable detail is the slightly destructive interference between all direct and superexchange matrix elements relevant for diffusion along the crystal *c*-axis. This occurs because the orbital energies shift such that the $|\tilde{-}\rangle$ state is lower in energy than the $|\tilde{+}\rangle$ state.

System	$t_{ }$	t'	$\sigma_{ }$	σ'	$ V_{\text{eff}} $	$ \tilde{V}_{\text{eff}} $
CdS	-5.4	-4.6	44.6	33.4	8.4	56.6
CdSe	-8.6	-7.8	47.8	34.8	14.0	54.7

TABLE 3.1: Relevant energetic couplings (in meV) for trapped-hole diffusion in Cd-chalcogenide nanocrystals. For both CdS and CdSe, all superexchange terms ($\{\sigma\}$) outweigh the direct tunneling matrix elements ($\{t\}$) by roughly an order of magnitude. The calculated diffusion constant will be proportional to the square of the effective coupling, which is V_{eff} for the direct pathway and \tilde{V}_{eff} including both direct and superexchange pathways. The superexchange mechanism increases the diffusion constant by about an order of magnitude in both materials.

3.5 Conclusions

In summary, this work modifies and expands upon our previous atomistic computational model for CdS.³¹ Here we study both CdS and CdSe with an emphasis on the superexchange corrections to the tunneling amplitudes between neighboring nonbonding sp^3 orbitals on the

surfaces of both CdS and CdSe nanocrystals. For each acceptor and donor (Figure 3.2) pair of trap sites, we partition the the Hamiltonian into a system and bath, where the bath corresponds to the dense set of bulk states. After partitioning, we transform the problem into two uncoupled Fano-Anderson models, which have exact expressions for the Green's functions and self-energies of the relevant impurity states. The difference in self-energies between the new dressed states, $|\tilde{\pm}\rangle$, allows for a direct calculation of the superexchange tunneling amplitude. When calculated in this fashion, the superexchange matrix elements are accurate to all orders in perturbation theory.

The direct tunneling pathway alone cannot account for the hole-hopping mechanism in CdS and CdSe. However, when including superexchange, we find that our results agree *quantitatively* with recent experimental work.³³ Surface-trapped holes are critically important participants in nanoscale photophysics and photochemistry, but they have been difficult to characterize both theoretically and experimentally. Our work shows that a systematic treatment founded in the quasiparticle nature inherent of the Green's function formalism is instrumental in understanding their behavior. This is likely true not only for CdS and CdSe, but also for any nanoscale material where underlying phenomena are strongly influenced by coupling to a dense manifold of electronic states.

3.6 Appendix B Contents

DFT convergence details for CdSe; description of the Wannier-basis Hamiltonian; mapping onto the Fano-Anderson problem; effect of the Wannier localization scheme on orbital energies and Green's function analyses; Wannier localization convergence details; orbital localization comparisons; additional figures and results.

3.7 Acknowledgement

This material is based upon work supported by the National Science Foundation under Grant No. CHE-1455365 and the Air Force Office of Scientific Research under AFOSR Award No. FA9550-19-1-0083. This work utilized the RMACC Summit supercomputer, which is supported by the National Science Foundation (Awards ACI-1532235 and ACI-1532236), the University of Colorado Boulder, and Colorado State University. The Summit supercomputer is a joint effort of the University of Colorado Boulder and Colorado State University.

Chapter 4

Locally-Varying Vibrational Modes in Polytetrafluoroethylene[†]

4.1 Abstract

Polytetrafluoroethylene (PTFE) is a simple technologically-important fluorinated linear polymer. It is also a model system for solid–solid phase behavior in organic compounds that are held together through non-covalent forces. In this Chapter, we parametrize a vibrational-exciton model from density functional theory that relates mesoscale structure to the observable symmetric and antisymmetric stretching modes of PTFE. We apply this model to interpret emerging experimental vibrational microscopy data from the Raschke group. A sample of melted PTFE on a gold substrate contains regions of varying thickness of PTFE and yields distinct spectroscopic signatures. Low-thickness regions correspond to a systematic increase in the both the symmetric and antisymmetric frequencies, while high-thickness regions correspond to a systematic decrease in these frequencies. There is an observed statistical correlation between symmetric and antisymmetric stretch frequencies. We develop a mesoscopic theory for the spatially-varying polarization and show that these features are electrostatic in origin.

[†]Adapted with permission from Dönges, S. A.; Cline, R. P.; Zeltmann, S. E.; Nishida, J.; Metzger, B.; Minor, A. M.; Eaves, J. D.; and Raschke, M. B., *to be submitted for publication*.

4.2 Introduction

Polytetrafluoroethylene (PTFE) is a simple technologically-important fluorinated linear polymer. It is often considered as a model system for vibrational spectroscopy due to its high oscillator density in combination with a large transition dipole moment of the C–F bonds.^{51,52} PTFE molecules tend to form straight segments because of the electronegativity of the F atoms, and these molecules also have a large average chain lengths.

The non-covalent interactions are weak in PTFE, and a plethora of solid phases exist that are in near-coexistence at room temperature. These phases differ not only in molecular packing, but also in the conformation of individual molecules, especially between 0 and 30 °C.^{51,53,54} Much conformational disorder is observed in the crystalline phase as the temperature increases in this range.

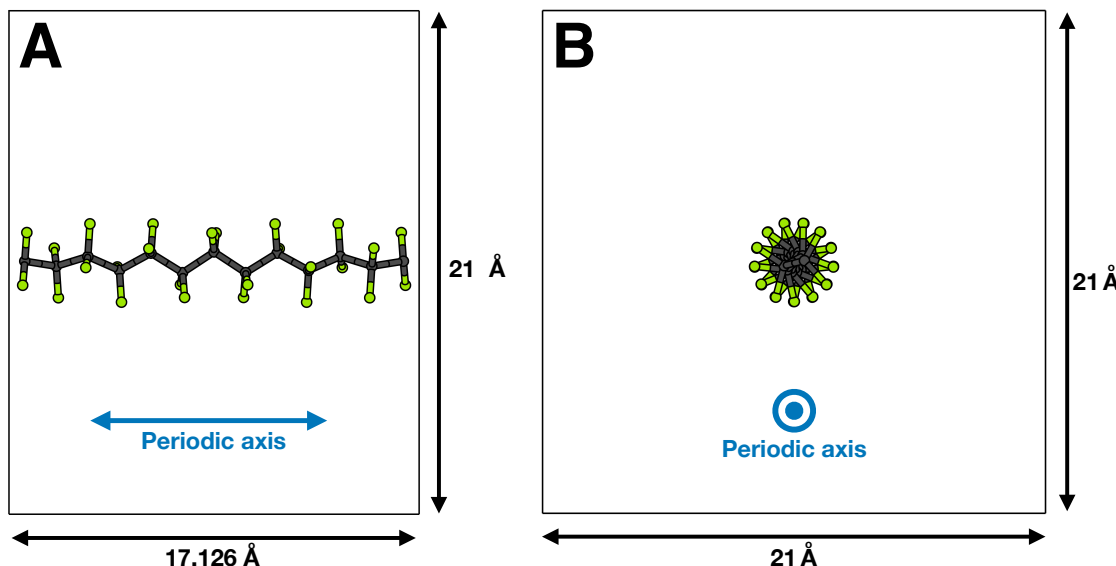


FIGURE 4.1: (A) Side view of the 13_6 infinite helix of PTFE. The DFT-relaxed chain length is 17.126 Å. (B) Perpendicular view of the 13_6 helix. The concentric circles denote the periodic axis is now perpendicular to the page. Only vacuum spacing is important for the box directions shown, whose lengths are both 21 Å, to minimize interactions between periodic images in directions perpendicular to the strand's periodic axis.

Near room temperature, two regular conformations of the polymer are well known: Form

II, stable below 19 °C, and Form IV, stable between temperatures of 19 and 30 °C. In Form II, PTFE organizes in a non-commensurable helix, with approximately 6 full helical turns every 13 carbon atoms, and packs in a pseudo-hexagonal triclinic crystal structure in the bulk phase. This is also called the 13_6 helix, and is the most ordered form of PTFE near room temperature. The experimental helix is closer to a commensurable 54_{25} helix,⁵⁴ but this is often approximated as a commensurable 13_6 helix, shown in Figure 4.1.^{51,53}

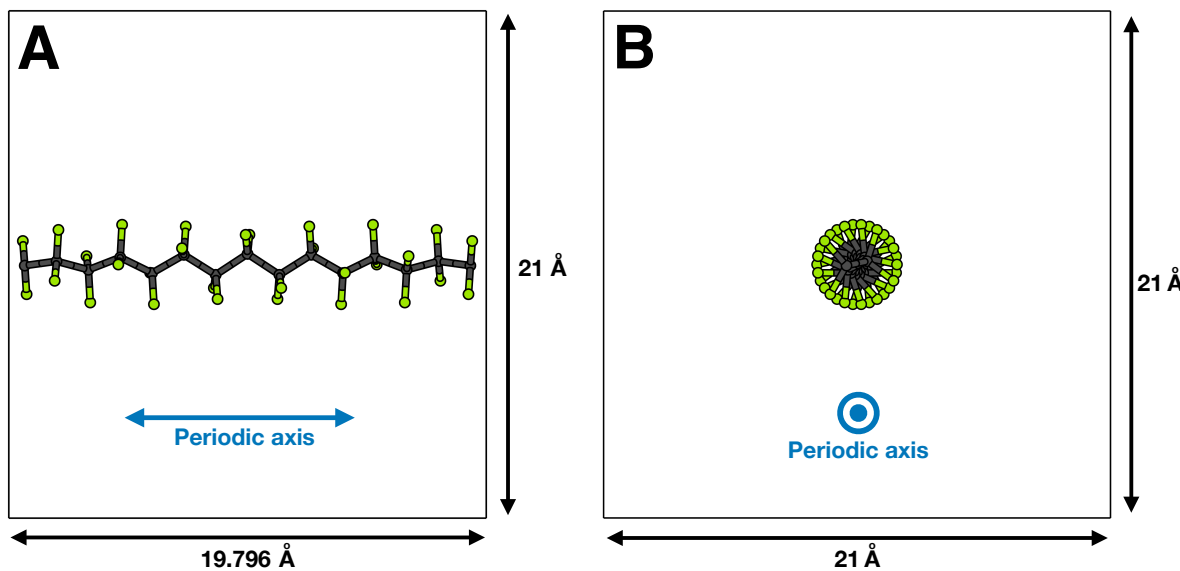


FIGURE 4.2: (A) Side view of the 15₇ infinite helix of PTFE. The DFT-relaxed chain length is 19.796 Å. (B) Perpendicular view of the 15₇ helix. The concentric circles denote the periodic axis is now perpendicular to the page. Only vacuum spacing is important for the box directions shown, whose lengths are both 21 Å, to minimize interactions between periodic images in directions perpendicular to the strand's periodic axis.

The transition to the more disordered Form IV occurs at 19° C. In Form IV, the helix untwists slightly to form a commensurable 15₇ helix, shown in Figure 4.2, and packs in a perfectly hexagonal crystal structure in the bulk phase. This conformation also gives rise to an increase of helical reversal defects and axial translational disorder of strands within the bulk.^{53,54,89}

Because of the closeness in temperature of the 13_6 and 15₇ phases and the propensity for disorder as temperature increases, ordered structures can coexist with disordered structures

within a thin temperature range of, for example, 15 – 25 °C, which corresponds to ambient room-temperature conditions. Thus, there may be spatially-varying structural heterogeneity throughout a sample studied in this range. Vibrational microscopy is a tool that might unveil such structural heterogeneity.

4.3 Methods

4.3.1 Experiment

Macroscopic function and properties in polymeric systems are strongly linked to their microscopic morphologies, especially in polymer systems with multiple constituents, such as polymer networks, block co-polymers, and polymer composites. Yet, while the compositional heterogeneity in these systems is well understood and often specifically engineered, few experimental techniques exist that can spatially resolve and identify variations in the local polymer morphology, particularly in homopolymers. Vibrational spectroscopy is a useful tool for probing information about the structure, coupling, and dynamics that give rise to the properties of complex molecular systems. Atkin *et al.*⁵² used femtosecond infrared scattering scanning near-field optical microscopy (IR *s*-SNOM) to resolve to examine the vibrational dynamics of local nanoscale probe volumes of PTFE in spatially distinct chemical environments. The IR *s*-SNOM measurements were characterized with high temporal, spectral, and spatial resolution.

The Raschke group has recently used (unpublished) highly delocalized vibrational modes in PTFE, probed by infrared scattering scanning near-field optical nano-spectroscopy (IR *s*-SNONS), to map local variations in the local polymer morphology. Specifically, they probe the high-frequency symmetric and antisymmetric stretching modes of PTFE. Experimentally, the symmetric and antisymmetric CF₂ stretch modes have frequencies of approximately 1160 cm⁻¹ and 1220 cm⁻¹, respectively, as determined from FTIR and electron energy loss spectroscopy at room temperature.⁵²

Figure 4.3A shows a schematic representation of the IR *s*-SNONS setup. The bottom image in Figure 4.3A displays a three-dimensional image of the edge of a sample of a melted PTFE bead approximately $10 \mu\text{m}$ in diameter, with the bead center approximately $4 \mu\text{m}$ above the top corner of the image. The low (dark) areas correspond to the gold substrate, while elevated areas are PTFE. Figure 4.3B shows two example spectra probed at different regions of the sample. Blue corresponds to regions of greater thickness (height of PTFE on substrate), and red corresponds to regions of lesser thickness. For the remainder of this Chapter, we refer to the height/altitude of the PTFE sample above the substrate as its topography, in analogy to landforms on Earth, i.e. mountains and valleys.

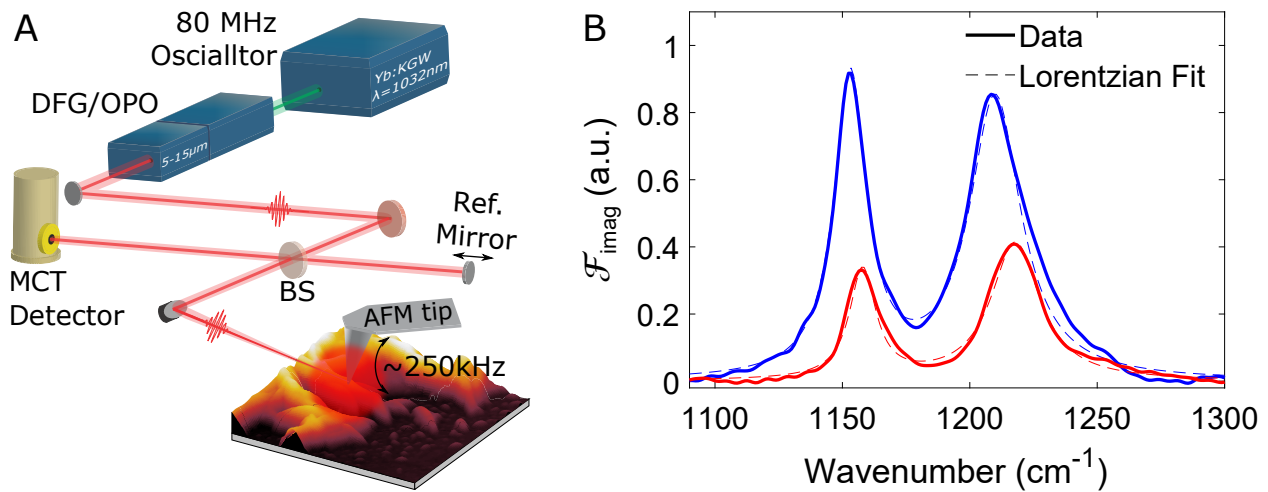


FIGURE 4.3: Experimental setup and results. These images are adapted with permission from our collaborators. (A) Schematic representation of the infrared scattering scanning near-field optical nano-spectroscopy (IR *s*-SNONS) setup. Of importance for this Chapter is the bottom-most image showing the sample (orange-yellow) on top of a gold substrate. The square base region shown is about $3 \mu\text{m} \times 3 \mu\text{m}$ in size, and PTFE stacks to roughly $0.5 \mu\text{m}$ at the highest points. (B) Example experimental vibrational spectra for the symmetric and antisymmetric stretching modes of PTFE, probed at different regions of the sample. Blue corresponds to thicker regions (high topography) of PTFE (brighter yellow in panel A), and red corresponds to thinner regions (low topography) of PTFE (darker orange and black in panel A).

A closer inspection of the topography (unpublished, not shown) shows that the melted PTFE organizes in hundreds of nanometer-wide elongated strands within the bulk of the bead, and forms smaller aggregates as the PTFE transitions to the bare substrate. The isolated PTFE aggregates, in most cases, are also elongated in one direction and extend in

size from several hundred nanometers down to sizes below the resolution of the atomic force microscopy (AFM) scan. The observation of a micro-scale substructure in the PTFE beads is independent of the temperature and duration during the melting process and is therefore not an effect of incomplete melting. The formation of similar structures in melted PTFE has also been observed in the past.⁹⁰

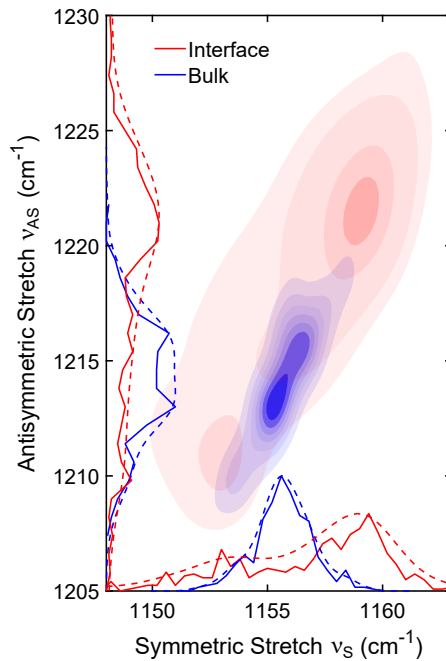


FIGURE 4.4: Experimental correlation plot for the symmetric and antisymmetric vibrational modes of a sample of melted PTFE on a gold substrate. The image at the bottom of Figure 4.3A shows the topography of the sample. Systematically, regions of higher topography correspond to lower frequencies, and regions of lower topography correspond to higher frequencies for both modes. Higher topography regions are denoted as bulk-like (blue), and lower topography regions are labeled as interface-like (red).

Figure 4.4 shows the main results of our collaborators' spatio-spectral *s*-SNOM experiments on melted PTFE beads on a template-stripped gold surface. Low topographical regions correspond to the interface between the PTFE and gold substrate, and high topographical regions correspond to bulk-like regions. Across all regions of the sample, we see spectral variations of approximately 25 cm^{-1} for the antisymmetric modes and approximately 15 cm^{-1} for the symmetric modes. Higher topographies typically corresponding to lower-frequency modes, and lower topographies typically correspond to higher-frequency

modes. Because the experimental setup is beyond the scope of this Chapter and the corresponding data are currently unpublished, we omit the remainder of the details pertaining to the experiment.

4.3.2 Theory

The positive correlation between the symmetric and antisymmetric mode frequencies cannot be explained through typical means, such variations in temperature near the 13_6 to 15_7 phase transition (experimental data omitted). Furthermore, this implies that local heterogeneities in a sample of PTFE caused by these temperature changes are likely only minor contributors to the data as well. To uncover the mechanism of these correlated shifts, we employ density functional theory (DFT) based vibrational-exciton modeling, the latter of which has been used successfully for molecular systems with cylindrical symmetries similar to PTFE.^{91–94} We choose to start with DFT because we ultimately want a predictive framework, and calculating the electronic structure from first principles is the best way to ensure this. We then construct a model exciton Hamiltonian description from the DFT results, which allows us to scale up the calculation beyond what DFT will typically allow, in particular for a study of the vibrational modes of a system.

4.3.2.1 DFT Calculations

We first take the structures for the isolated 13_6 and 15_7 helices provided by Quarti *et al.*⁵¹ and construct an appropriate unit cell for each. We choose to study the isolated strands instead of the bulk strands since performing the required normal-mode analyses of the bulk strands would be far more computationally intensive for such large molecules. Likewise, we aim to gain a qualitative understanding of the interactions between molecules here, not necessarily a quantitative one, so long as we find decent agreement between our DFT-generated vibrational spectra for the isolated strands and the experimental spectra.

After constructing the unit cells, we then geometrically relax the degrees of freedom (strand length and atomic positions) according to the details presented in section 4.6. Figures 4.1-4.2 show the results for the structures. From here, we employ density functional perturbation theory to calculate the normal modes for each type of strand. From these normal modes, we then compute the absorption spectrum, which we discuss in section 4.3.2.3.

4.3.2.2 Vibrational-Exciton Hamiltonian

To construct a theoretical model for the C–F oscillator vibrations in PTFE that we can compare with DFT, we begin by deriving an expression for the Hamiltonian. We can identify three distinct energy parameters for the PTFE molecules if we conform to a local-mode basis: (1) an unperturbed frequency for an isolated C–F oscillator, (2) interactions between C–F oscillators corresponding to the same carbon atom, and (3) interactions between C–F oscillators corresponding to different carbon atoms. We make such distinction between *intra-* and *inter*-carbon oscillators because the intra-carbon oscillators are directly connected to each other, giving rise to a significant mechanical coupling not present for inter-carbon oscillators (Figure 4.5).

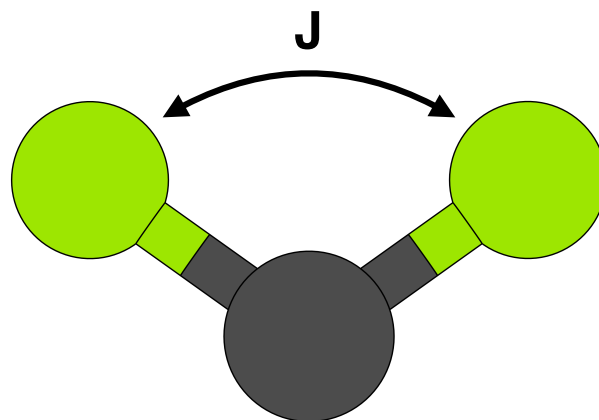


FIGURE 4.5: Closeup view of one unit of CF_2 in a strand of PTFE. Because the left and right C–F oscillators are connected to the same carbon atom, the motion of one oscillator influences the motion of the other, giving rise to a mechanical coupling between the oscillators. We call the mechanical coupling J .

We show the intended effect of turning on these interactions in Figure 4.6. In the absence of any interactions (Figure 4.6A), only one peak is visible in the spectrum: the diagonal elements of the Hamiltonian, which are the same for each C–F oscillator. Upon turning on the intra-carbon interactions, we find the results in Figure 4.6B, where the formerly single peak splits into two distinct modes, the local CF_2 symmetric and antisymmetric modes. These peaks need not exist with the same height. Turning on the inter-carbon interactions yields results seen in Figure 4.6C, where the peak positions and peak heights have further split.

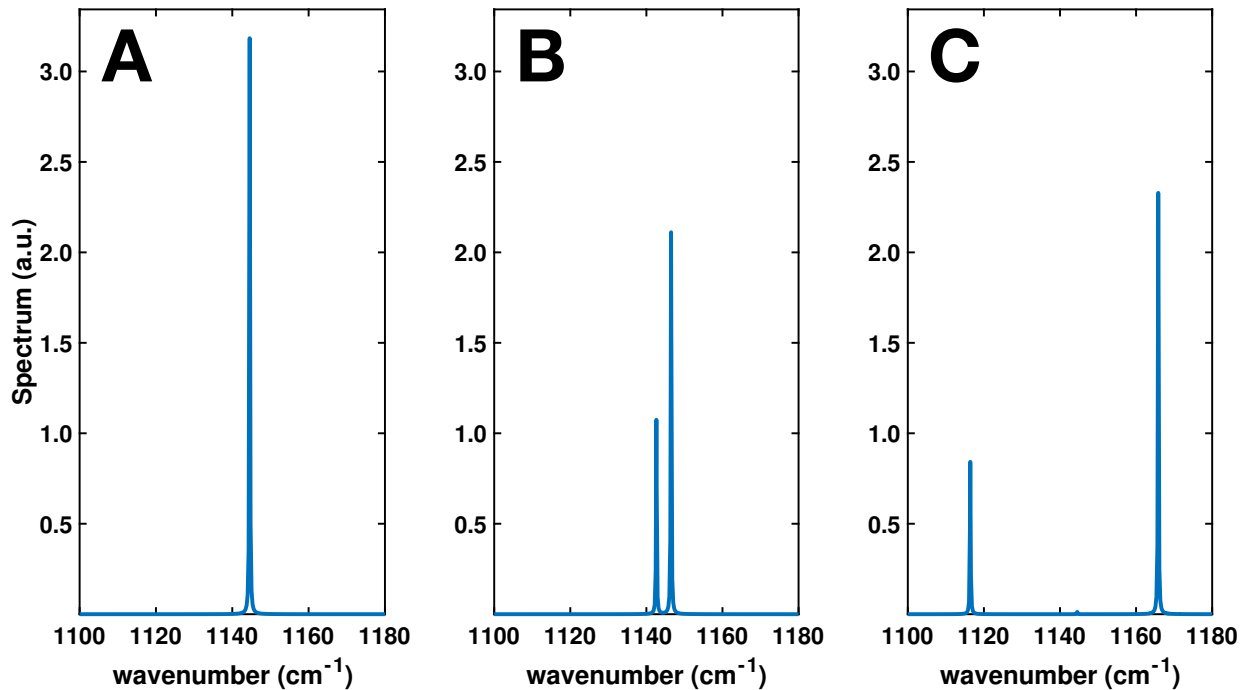


FIGURE 4.6: Turning on interactions in a vibrational-exciton model. (A) No interactions between any oscillators. (B) Only intra-carbon oscillator couplings are allowed. (C) All interactions between intra- and inter-carbon oscillators are included. The peak positions in the fully-interacting case shown are slightly different than experiment (by roughly 50 cm^{-1}) because of inaccuracies in the DFT calculations we employ. The relative peak positions (split by roughly 50 cm^{-1}), which are more important than the absolute positions, are similar to experiment.

We begin with the individual CF_2 units for deriving the Hamiltonian. We write down a form of the local-mode Hamiltonian, in the spirit of E. B. Wilson's GF method,⁹⁵ for a

single unit of CF_2 ,

$$H_{\text{Mech}}^{(1 \text{ } CF_2)} \approx \frac{1}{2} \sum_{s,t=1}^2 (p_s g_{st} p_t + q_s f_{st} q_t), \quad (4.1)$$

where s and t define our basis, which we choose to be the individual (local) C–F oscillators; q_s is a linear coordinate that corresponds to the s th local oscillator’s vibrational coordinate; p_s is the momentum conjugate to q_s ; f_{st} is the Hessian of the potential energy, V ; and g_{st} is, in general, a tensor evaluated at the minimum of V . For C–F oscillators attached to the same carbon atom, the off-diagonal kinetic terms are non-zero, as are the off-diagonal potential terms. Together, they give rise to the mechanical coupling, J (Figure 4.5).

Eq. 4.1 is completely classical; however, if we promote the expression to a second-quantized formalism, we find that $q_s \propto a_s^\dagger + a_s$ and $p_s \propto a_s^\dagger - a_s$, where a_s^\dagger (a_s) is the bosonic creation (annihilation) operator for a vibrational excitation of the s th C–F oscillator. Therefore, if we limit our analysis to single-particle excitations only, we will arrive at the normal-ordered form of

$$p_i p_j \propto q_i q_j \propto a_i^\dagger a_j + a_j^\dagger a_i \quad (4.2)$$

for the H_{Mech} of all CF_2 pairs. This yields

$$H_{\text{Mech}} = \omega_0 \sum_\ell a_\ell^\dagger a_\ell + \frac{J}{2} \sum_{\substack{\ell, \ell' \neq \ell \\ intra}} (a_\ell^\dagger a_{\ell'} + a_{\ell'}^\dagger a_\ell) \quad (4.3)$$

in the quantum mechanical case for any number of CF_2 groups where only intra-carbon interactions are included. J is the mechanical coupling “through-bond” between intra-carbon oscillators (Figure 4.5), and ω_0 is the non-interacting C–F oscillator frequency. We write our Hamiltonian in units where $\hbar = 1$.

Limiting our discussion to the single-particle space means our theory falls within the realm of linear response. An external force that disturbs the system at frequency ω will

elicit a response back at frequency ω . We discuss the details of the linear response formalism later in this Chapter (section 4.3.2.3), but for now we motivate our choice by examining the time-evolution of the annihilation operator \tilde{a}_α in the eigenstate basis:¹⁵

$$\frac{d\tilde{a}_\alpha(t)}{dt} = -i\omega_\alpha \tilde{a}_\alpha(t). \quad (4.4)$$

The corresponding solution to this equation is

$$\tilde{a}_\alpha(t) = \tilde{a}_\alpha e^{-i\omega_\alpha t}. \quad (4.5)$$

Fourier-like integrals with this operator will yield responses at frequency ω_α . Consider instead a two-particle term

$$\frac{dA_\alpha(t)}{dt} = \frac{d(\tilde{a}_\alpha(t)\tilde{a}_\alpha(t))}{dt} = -2i\omega_\alpha \tilde{a}_\alpha(t)\tilde{a}_\alpha(t) \quad (4.6)$$

such that

$$\frac{dA_\alpha(t)}{dt} = A_\alpha e^{-2i\omega_\alpha t}. \quad (4.7)$$

Such a process falls outside the realm of linear response and should not have a bearing on the measured vibrational spectrum since the phonons in DFT are calculated in the harmonic approximation.

We now move to the interaction term between inter-carbon oscillators, which we call the “through-space” coupling. For long-range interactions between dipoles and neglecting the polarizabilities of the C–F oscillators in response to an applied electric field, the strongest force between them takes the form of a dipole-dipole interaction.^{96,97} Defining such an interaction for our strands of PTFE is necessary because of the arrangement of oscillators within the molecules. Figure 4.7 shows an angled view of the 13₆ strand of PTFE, clearly

illustrating the near-parallel arrangement of dipoles twisting around the structure. These relative near-parallel orientations will yield large dipole-dipole couplings, which ultimately will give rise to the existence of the delocalized normal modes in our model Hamiltonian.

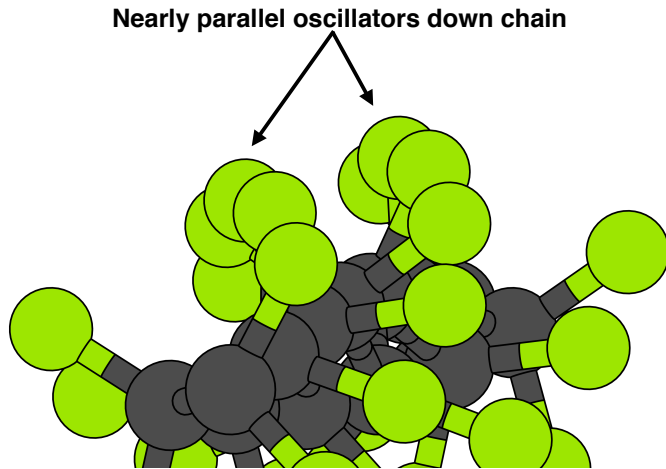


FIGURE 4.7: Angled view of a helical PTFE molecule. The periodic axis of the molecule is parallel to a line drawn through the center region in gray, the carbon atoms. Because of the helical symmetry of the molecule, C–F oscillators that twist around the chain are nearly parallel to each other, which enhances the dipole-dipole coupling between these oscillators. Oscillations of the local C–F modes will couple with those of other C–F modes, giving rise to the delocalized normal modes.

The dimension-full *classical* dipole-dipole interaction is

$$V^{(\mu\mu)} = \frac{1}{2} \sum_{\ell,m \neq \ell} \boldsymbol{\mu}_\ell \cdot \mathbf{T}_{\ell m} \cdot \boldsymbol{\mu}_m, \quad (4.8)$$

where $\mathbf{T}_{\ell m} = \frac{1 - 3\hat{\mathbf{r}}_{\ell m}\hat{\mathbf{r}}_{\ell m}}{4\pi\epsilon r_{\ell m}^3}$ is a rank-2 tensor containing the orientational and distance-dependent information of the interaction; $\mathbf{r}_{\ell m} = \mathbf{r}_\ell - \mathbf{r}_m = r_{\ell m}\hat{\mathbf{r}}_{\ell m}$; and $\epsilon = \epsilon_0\epsilon_r$, where ϵ_0 is the vacuum permittivity, and ϵ_r is the dielectric constant of the material. We must now construct a quantum operator from this classical expression.

To do so, we expand the dipole term to lowest order in q_ℓ since we are solving for the normal modes where this approximation is acceptable. Thus,

$$\boldsymbol{\mu}_\ell \approx \boldsymbol{\mu}_\ell^{(0)} + \tilde{\mathbf{d}}_\ell q_\ell = \boldsymbol{\mu}_\ell^{(0)} + \mathbf{d}_\ell(a_\ell^\dagger + a_\ell), \quad (4.9)$$

where we have defined $\tilde{\mathbf{d}}_\ell = \frac{\partial \boldsymbol{\mu}_\ell}{\partial q_\ell}$ and replaced the vibrational coordinates with their creation/annihilation operator forms. From here, we limit our expression to the single-particle excitation space. We also invoke the commutation relation for bosons, $[a_\ell, a_m^\dagger] = \delta_{\ell m}$, to cast our final expression in normal-ordered form. The result is

$$\begin{aligned} V^{(\mu\mu)} &= \frac{1}{2} \sum_{\ell, m \neq \ell} \mathbf{d}_\ell \cdot \mathbf{T}_{\ell m} \cdot \mathbf{d}_m (a_\ell^\dagger a_m + a_m^\dagger a_\ell) \\ &= \frac{1}{2} \sum_{\ell, m \neq \ell} V_{\ell m} (a_\ell^\dagger a_m + a_m^\dagger a_\ell). \end{aligned} \quad (4.10)$$

To simplify Eq. 4.10, we define $\mathbf{d}_\ell = d_\ell \hat{\mathbf{\mu}}_\ell$ such that all derivative terms are proportional to the initial dipole orientation. The scalar value is real and can be either positive or negative. Since all oscillators are identical, we set $|d_\ell| = |d|$ for all oscillators. This simplification is necessary for fitting the model spectrum to the DFT spectrum. Our model then corresponds purely to the vibrational stretches of the PTFE molecule.

Because $V_{\ell m}$ contains constants that will be present for all terms, we redefine this variable to extract a third fit parameter. First,

$$\mathbf{T}_{\ell m} = \frac{\tilde{\mathbf{T}}_{\ell m}}{4\pi\epsilon x_0^3}, \quad (4.11)$$

where $\tilde{\mathbf{T}}_{\ell m} = \frac{1 - 3\hat{\mathbf{r}}_{\ell m} \cdot \hat{\mathbf{r}}_{\ell m}}{(r_{\ell m}/x_0)^3}$ is dimensionless and x_0 is some characteristic unit of length. We then have

$$V_{\ell m} = \frac{|d|^2}{4\pi\epsilon x_0^3} \hat{\mathbf{\mu}}_\ell \cdot \tilde{\mathbf{T}}_{\ell m} \cdot \hat{\mathbf{\mu}}_m = \lambda \tilde{V}_{\ell m}, \quad (4.12)$$

where $\lambda = \frac{|d|^2}{4\pi\epsilon x_0^3}$. We thus arrive at the following second-quantized Hamiltonian:

$$H = \omega_0 \sum_\ell a_\ell^\dagger a_\ell + \frac{J}{2} \sum_{\substack{\ell, \ell' \neq \ell \\ intra}} (a_\ell^\dagger a_{\ell'} + a_{\ell'}^\dagger a_\ell) + \frac{\lambda}{2} \sum_{\substack{\ell, m \neq \ell \\ inter}} \tilde{V}_{\ell m} (a_\ell^\dagger a_m + a_m^\dagger a_\ell). \quad (4.13)$$

When we evaluate the Hamiltonian, we take periodic conditions into account by wrapping coordinates back around for distances greater than $L/2$, where L is the length of the PTFE strand. This means we effectively limit unique interactions in our model over distances of $L/2$. We do not perform an Ewald summation when evaluating our model Hamiltonian.

4.3.2.3 Linear Response Theory

In our model, we invoke linear response theory to solve for the vibrational spectrum. For a general external driving force $K(t)$ and a conjugate observable A , we first write down the Hamiltonian H_t at time t ,

$$H_t = H - AK(t). \quad (4.14)$$

We then define the general response function

$$\chi_{AB}(t) = \frac{1}{i} \langle [A(0), B(t)] \rangle, \quad (4.15)$$

which allows us to write down a relation for the response $\delta B(t)$ of the system as

$$\delta B(t) = \int_{-\infty}^t dt' K(t') \chi_{AB}(t-t'). \quad (4.16)$$

This expression is a convolution of the external force and the response function.

For describing the vibrational spectrum of a molecule, this expression turns into a relation for the polarization of a dielectric material,

$$\mathbf{P}(t) = \int_{-\infty}^t dt' \mathbf{E}(t') \chi(t-t') = \int_{-\infty}^t dt' \mathbf{E}(t-t') \chi(t'). \quad (4.17)$$

Fourier transforming this expression yields

$$\mathbf{P}(\omega) = \int_{-\infty}^{\infty} dt e^{-i\omega t} \mathbf{P}(t) = \mathbf{E}(\omega) \chi(\omega), \quad (4.18)$$

which is the expected expression from classical electrostatics⁹⁶ up to the usual inclusion of the vacuum permittivity, ϵ_0 . We will find that the imaginary part of the susceptibility, $\chi(\omega)$, gives rise to the absorption spectrum.

For describing the vibrational spectrum, we start from the response function

$$\chi(t) \propto \frac{1}{i} \langle [\boldsymbol{\mu}(0), \boldsymbol{\mu}(t)] \rangle \quad (4.19)$$

where $\boldsymbol{\mu}$, the total dipole moment of the sample, is the relevant quantity for describing the polarization. We leave off all constant terms in this expression, besides i , since we normalize our final spectrum at the end. We define $C(t) = \langle \boldsymbol{\mu}(0) \boldsymbol{\mu}(t) \rangle$, which we can split into its real and imaginary parts,

$$C(t) = C'(t) + iC''(t). \quad (4.20)$$

Upon evaluating Eq. 4.19, we find $\chi(t) \propto C''(t)$, where

$$C''(t) = \frac{C(t) - C(-t)}{2i}. \quad (4.21)$$

To calculate $\chi(t)$, we first evaluate

$$C(t) = \langle 0 | \boldsymbol{\mu}(0) e^{iHt} \boldsymbol{\mu}(0) e^{-iHt} | 0 \rangle = \sum_{\alpha} e^{i\omega_{\alpha} t} \langle 0 | \boldsymbol{\mu} | \alpha \rangle \langle \alpha | \boldsymbol{\mu} | 0 \rangle, \quad (4.22)$$

where $|\alpha\rangle$ is an eigenstate of the Hamiltonian, i.e. a normal mode, and $|0\rangle$ is the ground state (no excitations) to which we reference all states' energies. We then have

$$\chi(t) \propto \frac{1}{i} \sum_{\alpha} (e^{i\omega_{\alpha}t} - e^{-i\omega_{\alpha}t}) \langle 0 | \mu | \alpha \rangle \langle \alpha | \mu | 0 \rangle. \quad (4.23)$$

To calculate the spectrum from the response function, we follow the formalism put forth by Kubo⁹⁸ and define the Fourier-Laplace transform

$$f(\omega) = \int_0^{\infty} dt e^{-i\omega t} f(t). \quad (4.24)$$

To perform this transform, we must first evaluate the Laplace transform

$$\mathcal{L}[\chi(t)] = \int_0^{\infty} dt e^{-zt} \chi(t), \quad (4.25)$$

where $z = \sigma + i\omega$. We then take the limit

$$\lim_{\sigma \rightarrow 0^+} \mathcal{L}[\chi(t)] = \chi(\omega), \quad (4.26)$$

where $\chi(\omega)$ is the susceptibility. This transformation is important for enforcing causality.

Starting from Eq. 4.25, we must perform a sum of integrals of the type

$$\int_0^{\infty} e^{\pm i\omega_{\alpha}t - zt} dt = \frac{\pm i}{\omega_{\alpha} \pm iz}. \quad (4.27)$$

If we substitute $z = \sigma + i\omega$ and take the limit as σ goes to 0 from the right, we arrive at

$$\chi(\omega) \propto \sum_{\alpha} \left(\frac{1}{\omega_{\alpha} - \omega + i0^+} + \frac{1}{\omega_{\alpha} + \omega - i0^+} \right) \langle 0 | \mu | \alpha \rangle \langle \alpha | \mu | 0 \rangle. \quad (4.28)$$

This expression is, in general, complex, so we split it into real and imaginary parts according to Kubo,⁹⁸

$$\chi(\omega) = \chi'(\omega) - i\chi''(\omega). \quad (4.29)$$

Because the time-domain response function is odd, we calculate the dissipative/absorptive part from $\chi''(\omega)$, which is the negative imaginary component of $\chi(\omega)$.⁹⁸ Doing so yields

$$\chi''(\omega) \propto \sum_{\alpha} \left(\delta(\omega - \omega_{\alpha}) - \delta(\omega + \omega_{\alpha}) \right) \langle 0 | \boldsymbol{\mu} | \alpha \rangle \langle \alpha | \boldsymbol{\mu} | 0 \rangle. \quad (4.30)$$

The first term of Eq. 4.30 represents the absorption spectrum that comes from the correlation function $C(t)$. For the remainder of this Chapter, we limit our discussion to the absorption spectrum, $C(\omega)$:

$$C(\omega) \propto \sum_{\alpha} \delta(\omega - \omega_{\alpha}) \langle 0 | \boldsymbol{\mu} | \alpha \rangle \langle \alpha | \boldsymbol{\mu} | 0 \rangle. \quad (4.31)$$

We ignore all common factors for the rest of this Chapter since we take care of them by normalizing the spectra $C(\omega)$ to a specified area at the end.

To compute the DFT absorption spectrum, we express the dipole operator as $\boldsymbol{\mu} = \sum_{\alpha} \boldsymbol{\mu}_{\alpha}$ and expand each term to first order in the normal mode coordinates Q_{α} :

$$\boldsymbol{\mu}_{\alpha} \approx \boldsymbol{\mu}_0 + \frac{\partial \boldsymbol{\mu}}{\partial Q_{\alpha}} Q_{\alpha} = \boldsymbol{\mu}_0 + \mathbf{d}_{\alpha} Q_{\alpha}. \quad (4.32)$$

We substitute $Q_{\alpha} \propto \tilde{a}_{\alpha}^{\dagger} + \tilde{a}_{\alpha}$, where $\tilde{a}_{\alpha}^{\dagger}$ (\tilde{a}_{α}) is the creation (annihilation) operator for normal mode α , yielding the final expression after restricting our calculation to single-particle excitations,

$$C(\omega) \propto \sum_{\alpha} \mathbf{d}_{\alpha} \mathbf{d}_{\alpha} \delta(\omega - \omega_{\alpha}). \quad (4.33)$$

If we take the isotropic part of the resulting rank-2 tensor, we arrive at

$$C(\omega) \propto \sum_{\alpha} |\mathbf{d}_{\alpha}|^2 \delta(\omega - \omega_{\alpha}). \quad (4.34)$$

Now we turn to the local-mode representation, which is necessary for applying our fit between the vibrational-exciton model and the DFT results. We first express the total dipole moment in terms of the local C–F oscillator dipoles, $\boldsymbol{\mu}(t) = \sum_{\ell} \boldsymbol{\mu}_{\ell}(t) = \sum_{\ell} e^{iHt} \boldsymbol{\mu}_{\ell} e^{-iHt}$, where H corresponds to the equilibrium Hamiltonian, Eq. 4.13. We use the Taylor expansion from earlier, Eq. 4.9, for $\boldsymbol{\mu}_{\ell}$. To evaluate the required matrix elements, we must transform the local-mode coordinates to the normal-mode representation. To do so, we first define a unitary transformation of the creation and annihilation operators:

$$a_{\ell}^{\dagger} = \sum_{\alpha} \tilde{a}_{\alpha}^{\dagger} U_{\alpha\ell}^{\dagger} \quad (4.35)$$

$$a_{\ell} = \sum_{\alpha} U_{\ell\alpha} \tilde{a}_{\alpha}. \quad (4.36)$$

We then enforce that the columns of the unitary matrices are the eigenvectors, thus diagonalizing the Hamiltonian. We can now evaluate

$$\langle 0 | a_{\ell} | \alpha \rangle = \sum_{\alpha'} \langle 0 | U_{\ell\alpha'} \tilde{a}_{\alpha'} | \alpha \rangle = U_{\ell\alpha}, \quad (4.37)$$

which yields,

$$C(\omega) \propto \sum_{\ell,m} \sum_{\alpha} \delta(\omega - \omega_{\alpha}) \hat{\boldsymbol{\mu}}_{\ell} \hat{\boldsymbol{\mu}}_m U_{\ell\alpha} U_{\alpha m}^{\dagger}. \quad (4.38)$$

If we approximate the spectrum using the isotropic part, we arrive at

$$C(\omega) \propto \sum_{\ell,m} \sum_{\alpha} \delta(\omega - \omega_{\alpha}) \text{Tr} [\hat{\boldsymbol{\mu}}_{\ell} \hat{\boldsymbol{\mu}}_m U_{\ell\alpha} U_{\alpha m}^{\dagger}], \quad (4.39)$$

where we take the trace of the resulting tensor. The indices ℓ and m denote the local oscillators. The column vectors of U are the eigenvectors of the Hamiltonian.

With the derived model spectrum, we make one final assertion. The polarization, Eq. 4.17, is proportional to the susceptibility, $\chi(t)$, which in the local-mode basis takes the form

$$\chi(t) \propto \sum_{\ell,m} \langle [\boldsymbol{\mu}_\ell(0), \boldsymbol{\mu}_m(t)] \rangle. \quad (4.40)$$

The polarization, $\mathbf{P}(t)$, is thus a local operator that can be decomposed in terms of spatially local time-correlation functions of the dipole operators. From the above relation, we define a local polarization $\mathbf{P}_\ell(t)$ for the ℓ th oscillator in the system, such that

$$\mathbf{P}(t) = \sum_\ell \mathbf{P}_\ell(t). \quad (4.41)$$

It follows from the linear response formalism that we can split up the absorption spectrum, $C(\omega)$, in the same fashion. This yields

$$C(\omega) = \sum_\ell C_\ell(\omega). \quad (4.42)$$

Thus, in the local-mode representation, we have derived a spatially-resolved IR spectrum, on a per-oscillator basis, that we can use to simulate the experimental setup (Figure 4.3A).

4.4 Results and Discussion

4.4.1 Model Fits of DFT Data

Using Eq. 4.34 and 4.39 directly, we fit the DFT results to the model Hamiltonian for both the 13_6 and 15_7 conformations of PTFE. To fit the DFT spectrum, we first verify that both the model Hamiltonian and DFT-computed phonon results produce two distinct, dominant peaks in their spectra corresponding to the symmetric (S) and antisymmetric

(AS) stretching modes. All other peak heights are negligible in relation to the two dominant frequencies. We use $\sigma = 4 \text{ cm}^{-1}$ corresponding to the real part of the Fourier-Laplace transform to smooth the peaks and aid the fit. We found results that were nearly identical to those using $\sigma = 1 \text{ cm}^{-1}$, which is quite strict. Upon using the larger σ for calculating the DFT spectrum, we find the results in Table 4.1.

Strand	S mode (cm^{-1})	AS mode (cm^{-1})
13₆	1116.4	1165.8
15₇	1119.6	1169.8

TABLE 4.1: Symmetric (S) and antisymmetric (AS) peak positions from DFT after employing $\sigma = 4 \text{ cm}^{-1}$ in the Fourier-Laplace transform. All peak positions are shifted in absolute terms by roughly 50 cm^{-1} relative to experiment. The relative splitting between peaks, $\sim 50 \text{ cm}^{-1}$, matches well with the experimental splitting of $\sim 60 \text{ cm}^{-1}$.

We perform three fits in total: (1) an individual fit of the isolated 13_6 DFT spectrum to the model Hamiltonian spectrum, (2) an individual fit of the isolated 15_7 DFT spectrum to the model Hamiltonian spectrum, and (3) a “global” fit of the interaction parameters J and λ for both the 13_6 and 15_7 spectra; we allow ω_0 to float between the strands since this is just an arbitrary center peak between the frequencies. The first two fits allow for all three fit parameters (ω_0 , J , λ) to be different between the two conformers. While the 13_6 and 15_7 helices are very similar in structure, previous work by Quarti *et al.*⁵¹ argues that interactions in bulk PTFE are effectively weaker for the 15_7 phase relative to the 13_6 phase. They rationalize this conclusion through structural differences between the two phases since bulk 13_6 PTFE is pseudo-hexagonal, while bulk 15_7 PTFE is perfectly hexagonal. This distinction could lead to an increase in helical-reversal defects for the 15_7 strand because of the perfect hexagonal packing.⁵¹ Such defects are known to occur more often in 15_7 PTFE,^{53,54,89} so the conclusions stated by Quarti *et al.* have merit. In this work, we work with individual strands of PTFE in tetragonal boxes, so such structural differences present in bulk will not be captured. However, if intermolecular interactions are indeed weaker for 15_7 PTFE for reasons other than bulk packing, then we want to allow our theory to capture

such differences in the isolated cases. We include the third “global” fit to force the coupling parameters to be identical between the strands to compare with the isolated cases.

When fitting our spectra, we only include the relevant S/AS modes in the fits since the intensities for all other modes are negligible. We perform the fits such that the area of each spectrum (DFT and model) is the same and equal to one. Figure 4.8 shows the results of the

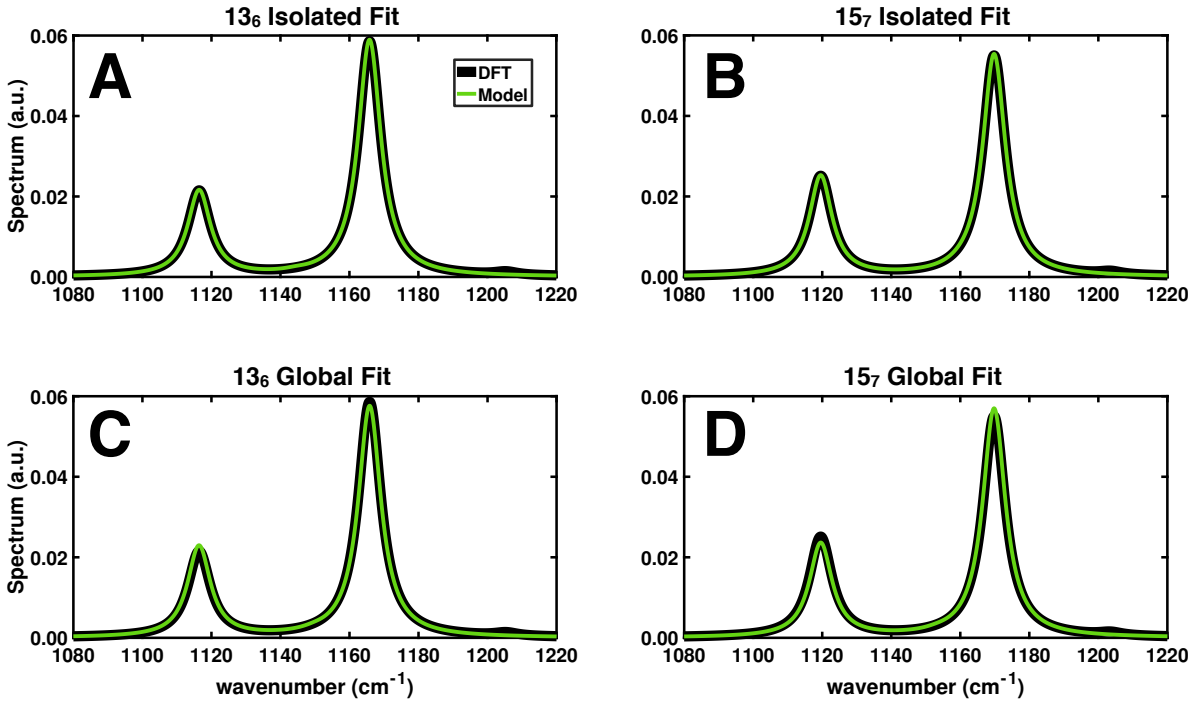


FIGURE 4.8: Vibrational spectra, $C(\omega)$, for different conformers and fits of PTFE. We show the DFT spectrum as a thick black line and overlay the model spectrum as a thinner green line. For both 13_6 fits, the S mode frequency is 1116.4 cm^{-1} , and the AS mode frequency is 1165.8 cm^{-1} . For both 15_7 fits, the S mode frequency is 1119.6 cm^{-1} , and the AS mode frequency is 1169.8 cm^{-1} . (A) 13_6 spectrum corresponding to a fit of the 13_6 periodic strand. (B) 15_7 spectrum corresponding to a fit of the 15_7 periodic strand. (C) 13_6 spectrum corresponding to a global fit of the coupling parameters of both the 13_6 and 15_7 strands. (D) 15_7 spectrum corresponding to a global fit of the coupling parameters of both the 13_6 and 15_7 strands.

model fits to the DFT spectra. In Figure 4.8, we show the negligibly-peaked intensities that we do not include in the fitting procedure to illustrate that both the DFT and model spectra are almost entirely dominated by the S and AS stretching modes, as previously discussed.

According to Figure 4.8, the fits for the isolated spectra are nearly perfect and yield the best agreement between the vibrational-exciton Hamiltonian and DFT. The global fits

of the coupling parameters yield results that closely approximate the DFT spectra of both strands, with small deviations in the relative peak heights present. Table 4.2 summarizes the fit parameters for all fit variations. We evaluate λ using $x_0 = 1 \text{ \AA}$. We see that the dipole-dipole coupling of the individual 15_7 fit is roughly half as strong as that of the individual 13_6 fit. On the other hand, the mechanical coupling is stronger by about a factor of eight in the individual 15_7 spectrum compared to that of the 13_6 fit. Lastly, the global fits produce, more or less, an average of the coupling strengths of the two isolated fits.

Fit	$\omega_0 (\text{cm}^{-1})$	$J (\text{cm}^{-1})$	$\lambda (\text{cm}^{-1})$
Isolated 13_6	1144.6	-1.9	116.7
Isolated 15_7	1145.7	-15.1	50.5
Global 13_6	1143.7	-7.3	89.3
Global 15_7	1146.5	-7.3	89.3

TABLE 4.2: Fit parameters for the helical conformations of PTFE. The values for λ correspond to setting $x_0 = 1 \text{ \AA}$ in Eq. 4.12.

4.4.2 Local Spectra Calculations

A simple way to probe if local environmental differences contribute to the spectral differences in our collaborators' samples of PTFE is to construct a small, finite ensemble (i.e. a bundle) of strands of PTFE, completely isolated from the rest of the universe by vacuum spacing. This will allow us to invoke our local expressions, Eq. 4.41-4.42, and test from a purely molecular and electrostatic standpoint if locally-varying spectral signatures exist. An arrangement of a finite bundle of PTFE would yield distinct bulk-like, interface-like, and intermediate regions within the sample. If we sum up all local spectra, $C_\ell(\omega)$, for a specific strand, we will arrive at the total local spectrum for that strand of PTFE.

Figure 4.9 shows a cross section of such an ensemble, with dots representing infinite strands of PTFE whose periodic axes are oriented perpendicular to the page. We approximate the 13_6 helix of PTFE to have the same molecular arrangement (perfectly hexagonal) as the 15_7 strand in this example. Since we are not forming a full crystal phase, we assume

this distinction will be negligible. As such, we will not be able to comment on the claims presented by Quarti *et al.*⁵¹ in terms of the structural differences between the two crystalline phases. We also neglect handedness in this calculation: all strands are of the same handedness, which matches that of the strands studied by Quarti *et al.*⁵¹ Finally, we separate strands by 5.7 Å to approximate the experimental separation of bulk PTFE.⁵³

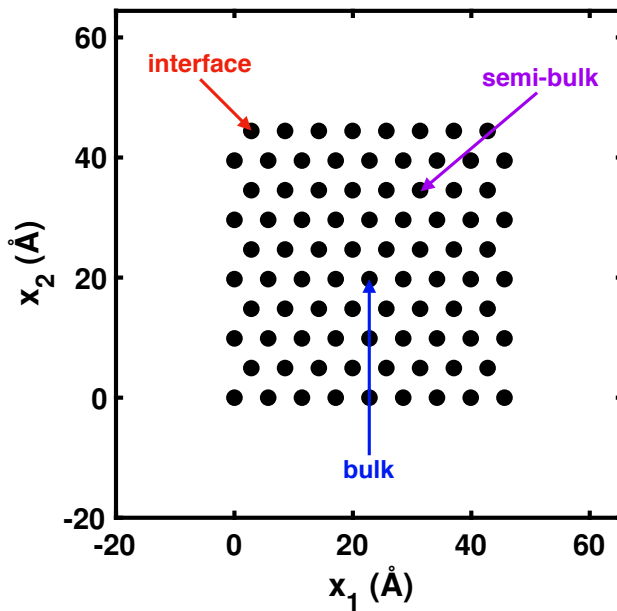


FIGURE 4.9: Cross section of a bundle of parallel PTFE strands for which we calculate their local spectra. Each solid dot represents a strand of PTFE oriented perpendicular to the page. All strands are separated from each other by 5.7 Å and placed on a perfectly-hexagonal lattice. No helical-reversal defects or relative helicity differences are included. All strands are of the same handedness. In all future spectral plots, the interface regions will correspond to red lines, the semi-bulk regions to various shades of purple, and the bulk regions to blue. We denote the plane perpendicular to the lengths of the PTFE strands by the axes x_1 and x_2 .

This system represents an analogy to the experimental setup presented by our collaborators. While they probe distinct regions of thousands of C–F oscillators,⁵² we can probe the local spectra of the individual strands (26 – 30 oscillators) in our sample. We can do this by taking the sum, Eq. 4.42, only over individual strands at a time. Thus, we will probe the spectra of strands that exist in different molecular environments. If the high topographical regions in Figure 4.4A correspond to “bulk-like” regions, then we expect the center-most strands in Figure 4.9 to correspond to the lowest-frequency S and AS modes. Likewise, we

expect the outer-most strands in Figure 4.9 to correspond to the highest-frequency S and AS modes, which will compare with the low topographical regions of 4.4A.

Figure 4.10 shows the results of the local spectra calculations for all fits we perform. Spectra in blue correspond to the inner-most bulk-like strands, red to the outer-most interface-like regions, and a gradient from blue to red for intermediate strands. We use a value of $\sigma = 16 \text{ cm}^{-1}$ to wash out spectra with double peaks, which makes it easier to assign peak positions. Across all simulations, the interface regions yield peak positions at higher frequencies relative to the bulk-like regions. The strongest variations in the local spectra between bulk- and interface-like strands occur for the ensemble of 13_6 strands calculated using the 13_6 isolated fit, Figure 4.10A. The weakest variations occur for the ensemble of 15_7 strands calculated using the 15_7 isolated fit, Figure 4.10B. The global fits, Figure 4.10C and D, yield nearly identical results and represent, approximately, an average of the two isolated fits.

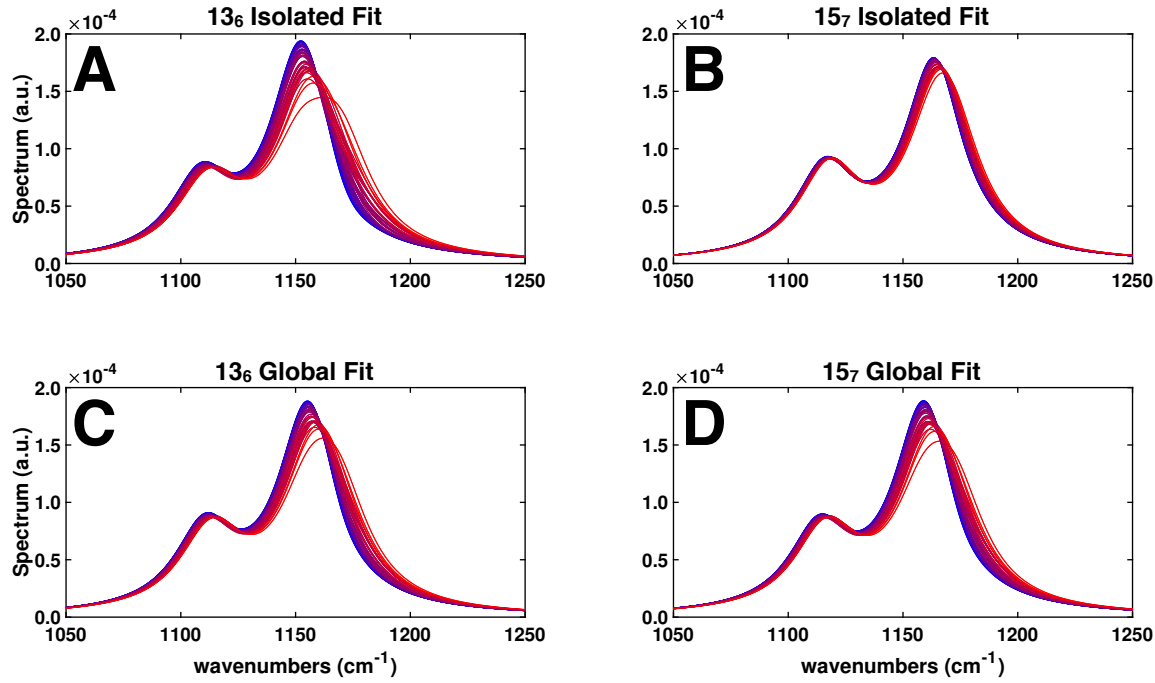


FIGURE 4.10: Local spectra calculations for the strands at the positions shown in Figure 4.9. The panels here correspond to the fits described in Figure 4.8. Spectra denoted by red lines correspond to strands on the outer interface-like regions, purple to strands in the semi-bulk regions, and blue to the strands in the center bulk-like regions.

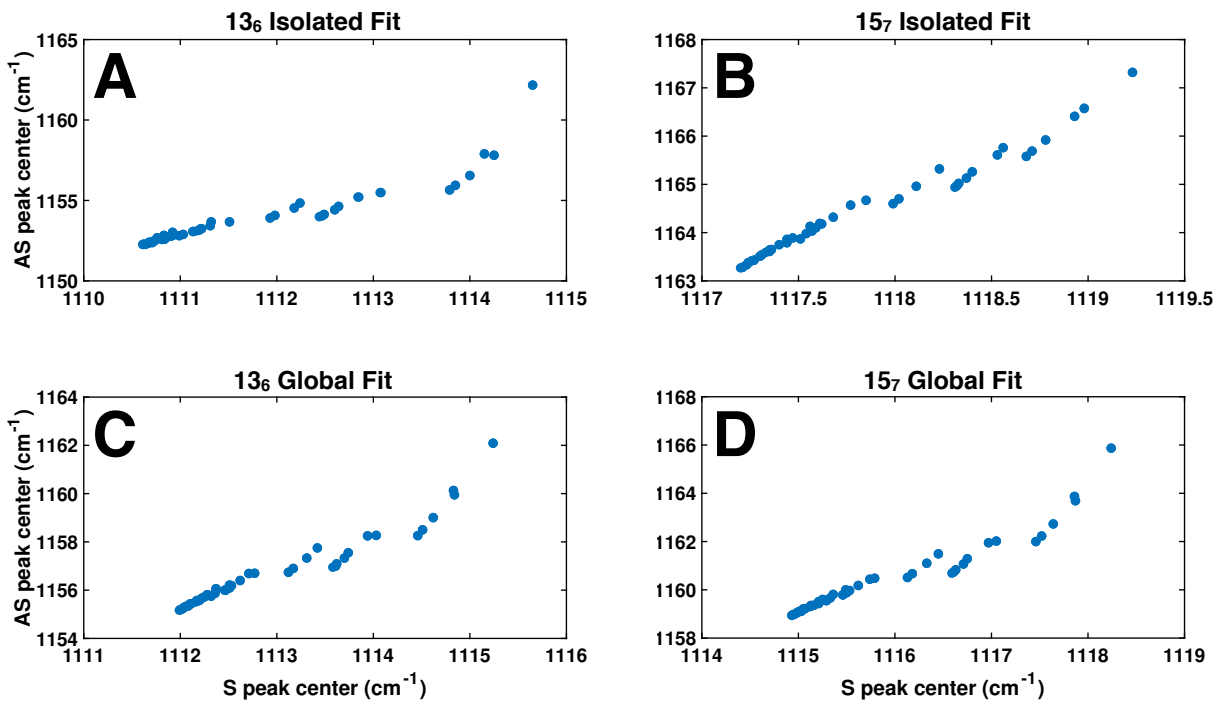


FIGURE 4.11: Summary of the peak positions in Figure 4.10. We plot the AS frequencies as a function of the S frequencies. We see clear signs of positive correlation between these modes, with the interface regions occurring at higher frequencies, and the bulk regions occurring at lower frequencies. The calculations that come closest to the experimental results correspond to the 13₆ isolated fit.

Figure 4.11 shows a plot of the peak positions for the AS modes as a function of the S modes from the local spectra calculations in Figure 4.10. The labels are consistent between the two figures. These plots show more clearly the trending positive shift in frequencies for both modes, and similar to the experimental data (Figure 4.4B), we find that the AS modes shift higher than do the S modes across all fits. For the calculations corresponding to the 13₆ isolated fit (Figure 4.11A), the AS frequencies shift higher by $\sim 10\text{ cm}^{-1}$, relative to the $\sim 4\text{ cm}^{-1}$ shift of the S frequencies. For the calculations corresponding to the 15₇ isolated fit (Figure 4.11B), the AS frequencies shift higher by $\sim 4\text{ cm}^{-1}$, relative to the $\sim 2\text{ cm}^{-1}$ shift of the S frequencies. For the calculations corresponding to both global fits (Figure 4.11C and D), the AS frequencies shift higher by $\sim 7\text{ cm}^{-1}$, relative to the $\sim 3\text{ cm}^{-1}$ shift of the S frequencies. In all cases, the ratio is roughly 2:1, consistent with the experimental data. Thus, we show that local variations in *only* the molecular environment explain the

positively-correlated shifts seen by our collaborators. This effect is electrostatic in origin since inter-carbon oscillators only interact through the dipole-dipole interaction in our model.

4.5 Conclusions

In summary, we use a combination of density functional theory calculations and theoretical modeling to explain the correlated spectral variations in mesoscopic samples of PTFE seen by our collaborators. We first calculate the vibrational modes of isolated strands of PTFE from first principles, and we then map this vibrational problem onto an essentially electrostatic model. In this model of the vibrational excitations, we show that the polarization, $\mathbf{P}(t)$, of the sample of PTFE can be broken up into discrete local contributions, $\mathbf{P}_\ell(t)$, for each local C–F oscillator in the ensemble. Because of this, we show that oscillators in the middle of a bundle of PTFE experience different electric fields than those on the exterior, and the frequencies in the corresponding local spectra shift accordingly. If we sum up the contributions for all oscillators one strand at a time, we find that PTFE molecules in interface regions show correlated higher-frequency shifts of both the symmetric and anti-symmetric stretching modes relative to those of strands in bulk-like positions. We therefore show that the correlated shifts seen by our collaborators are electrostatic in origin and are independent of temperature and other experimental details.

4.6 Computational Methods

We used the Vienna Ab initio Simulation Package (VASP)^{73–78} to compute the DFT results. Our calculations employed the projector augmented wave method and the exchange-correlation functional with the Perdew-Burke-Ernzerhof (PBE) generalized gradient approximation.^{77,78} We used the standard C and F pseudopotentials supplied by VASP, which treat explicitly the $(2s)^2(2p)^4$ electrons for both potentials. For sampling the Brillouin zone, we

used four k-points along the reciprocal lattice vector conjugate to the length of the PTFE strands and one k-point in the other two directions.

We set the plane-wave cutoff to 1040 eV, or 2.6 times the default cutoff. We used this large basis set because it converged the energy to less than 1 meV/atom, which we demanded to ensure accurate calculations. We required an electronic convergence of 10^{-7} eV and a minimum of 10 electronic steps when minimizing the electronic structure. Because we calculate the phonon spectrum for our strands of PTFE, we set the precision-mode to accurate and adjusted the fine FFT grids to reduce the noise in the forces. We required a final force convergence of 5×10^{-5} eV/ \AA for the atomic positions of both the 13_6 and 15_7 helical conformations.

Before relaxing the atomic positions to the desired force convergence, we first relaxed the length of each PTFE strand by allowing the unit cell lattice constant in that direction to change. We modified and employed the function `constr_cell_relax.F` supplied with VASP to restrict a full geometry relaxation (atomic positions, cell shape, cell volume) to change *only* the atomic positions and the desired lattice constant. The results for the lengths are shown in Figures 4.1-4.2. We required a force convergence of 10^{-4} eV/ \AA for the 13_6 helix and 10^{-3} eV/ \AA for the 15_7 helix for this “restricted-full” relaxation. We stopped at these force cutoffs due to complications from Pulay stress, which was still present even at a 1040 eV plane-wave cutoff.

We used the nonlinear least-squares algorithm `lsqnonlin` in MATLAB to fit each DFT-calculated spectrum to the model Hamiltonian spectrum. We ensured that the minimizer arrived at the output state: “Optimization completed because the size of the gradient is less than the value of the optimality tolerance” which we set to the default value. We also employed “central” finite differences, which is more accurate than the default “forward” setting.

Chapter 5

Future Work: Phonon Modes Assisting Trapped-Hole Diffusion in CdS and CdSe Nanocrystals

5.1 Introduction

In Chapters 2-3, we calculated approximate ground-state adiabatic electronic structures for CdS and CdSe nanocrystal surfaces. We then transformed the adiabatic solutions into diabatic representations and, through small polaron theory and Marcus theory, connected the site-to-site tunneling matrix elements in the diabatic representations to an effective one-dimensional diffusion constant, which we then compared with experiment.^{30,32,33} It is remarkable that, especially in Chapter 3, we found matrix elements that were *quantitatively* consistent with experimental data, even though none of those calculations included any explicit dynamics.

In this Chapter, we propose the next phase of the trapped-hole diffusion project: to determine the phonon modes that assist surface-trapped hole diffusion. To do so, we propose to perform Born-Oppenheimer molecular dynamics at finite temperature, below the materials' melting points, to evolve both the electronic structures and atomic configurations in time. Calculating the phonon modes directly is an intractable task for the system sizes we wish to consider, but allowing our systems to evolve in time is equivalent to allowing the crystals to vibrate according to their fundamental frequencies — the phonon modes.

5.2 Methods

5.2.1 Spin-Boson Hamiltonian

The general system-bath Hamiltonian for a system with internal coupling and a bath with no internal coupling is

$$\mathcal{H} = H_0 + V_S + V_{SB}, \quad (5.1)$$

where $H_0 = H_S + H_B$ is diagonal and comprises the bare system and bath Hamiltonians, respectively; V_S is the internal system coupling, and V_{SB} is the system-bath coupling. At finite temperature for CdS or CdSe nanocrystals, the bath Hamiltonian takes the form of the phonon modes since the crystal vibrations at finite temperature can be decomposed into these modes.

For a generic two-level system composed of a donor (D) and acceptor (A) state that are not eigenstates of the system Hamiltonian and are not, in general, orthogonal or degenerate, the general Hamiltonian terms are⁹⁹

$$H_0 = E_A|A\rangle\langle A| + E_D|D\rangle\langle D| + \sum_{\nu} \omega_{\nu} a_{\nu}^{\dagger} a_{\nu}, \quad (5.2)$$

$$V_S = t_{AD}|A\rangle\langle D| + t_{DA}|D\rangle\langle A| \quad (5.3)$$

$$V_{SB} = \sum_{\nu} \left(a_{\nu}^{\dagger} + a_{\nu} \right) \left(\lambda_{\nu}^{AA}|A\rangle\langle A| + \lambda_{\nu}^{AD}|A\rangle\langle D| + \lambda_{\nu}^{DA}|D\rangle\langle A| + \lambda_{\nu}^{DD}|D\rangle\langle D| \right), \quad (5.4)$$

where we use units corresponding to $\hbar = 1$. The operator a_{ν}^{\dagger} (a_{ν}) is the creation (annihilation) operator for phonon mode ν . For cases in which the acceptor/donor states share negligible overlap, the third term can be simplified to⁹⁹

$$V_{SB} = \sum_{\nu} \left(a_{\nu}^{\dagger} + a_{\nu} \right) \left(\lambda_{\nu}^A|A\rangle\langle A| + \lambda_{\nu}^D|D\rangle\langle D| \right). \quad (5.5)$$

Wannier orbitals are mutually orthogonal by construction; furthermore, in a real nanocrystal system, surface lattice sites corresponding to hole traps are sufficiently far apart, roughly one nanometer, such that orbital overlap should be negligible. Thus, Eq. 5.5 is valid for our description of trapped-hole diffusion in CdS and CdSe.

Because of the two-level nature of the system, this Hamiltonian description is sometimes called the “spin-boson” model to reflect a two-state system connected to a bath of bosons. Furthermore, with the simplification we made for V_{SB} , the full Hamiltonian, Eq. 5.1, is precisely a small polaron Hamiltonian (Chapter 2), written only for the two-level system involved in a single hopping event.

We can then rearrange terms and enforce that the equilibrium system states are degenerate, $E_0 = E_A = E_D$, which is what we find in Chapters 2 and 3 for the relevant diabatic states. This yields

$$\begin{aligned} \mathcal{H} = & \left[E_0 + \sum_{\nu} \lambda_{\nu}^A (a_{\nu}^{\dagger} + a_{\nu}) \right] |A\rangle\langle A| + \left[E_0 + \sum_{\nu} \lambda_{\nu}^D (a_{\nu}^{\dagger} + a_{\nu}) \right] |D\rangle\langle D| \\ & + t_{AD}|A\rangle\langle D| + t_{DA}|D\rangle\langle A| + \sum_{\nu} \omega_{\nu} a_{\nu}^{\dagger} a_{\nu} \end{aligned} \quad (5.6)$$

where we see clearly the effect the phonon bath has on the diabatic states. Within this small polaron limit, the on-site energies of the orbitals fluctuate in time due to finite-temperature fluctuations of the underlying lattice about its equilibrium geometry.

The absolute energy scales are irrelevant; only the difference between the acceptor/donor states is important. We thus define

$$\epsilon_A = E_0 + \sum_{\nu} \lambda_{\nu}^A (a_{\nu}^{\dagger} + a_{\nu}) \quad (5.7)$$

$$\epsilon_D = E_0 + \sum_{\nu} \lambda_{\nu}^D (a_{\nu}^{\dagger} + a_{\nu}) \quad (5.8)$$

$$\Sigma = \frac{\epsilon_A + \epsilon_D}{2} \quad (5.9)$$

$$\Delta = \epsilon_A - \epsilon_D, \quad (5.10)$$

where Σ is an arbitrary center frequency between the two diabatic states and can be subtracted off from the total Hamiltonian without loss of generality. This leaves

$$\mathcal{H} = \frac{\Delta}{2}|A\rangle\langle A| - \frac{\Delta}{2}|D\rangle\langle D| + t_{AD}|A\rangle\langle D| + t_{DA}|D\rangle\langle A| + \sum_{\nu}\omega_{\nu}a_{\nu}^{\dagger}a_{\nu}. \quad (5.11)$$

Clearly, the only fluctuating system quantity influenced by the dynamics is the energy-gap term, Δ . Furthermore, due to the degeneracy of the surface orbitals relevant for trapped-hole diffusion, we find

$$\Delta = \sum_{\nu}\left(\lambda_{\nu}^A - \lambda_{\nu}^D\right)\left(a_{\nu}^{\dagger} + a_{\nu}\right). \quad (5.12)$$

The energy-gap operator is influenced entirely by the difference of the electron–phonon coupling terms. Figure 5.1 shows an illustration of the diabatic energy levels at equilibrium compared to some time t .

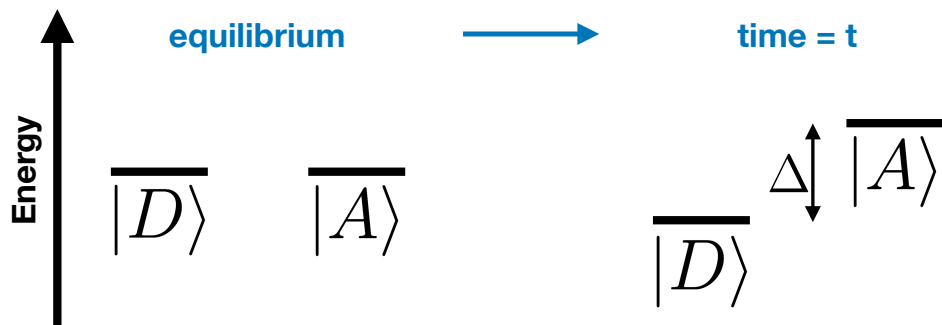


FIGURE 5.1: Energy level diagram of the diabatic donor and acceptor states, $|D\rangle$ and $|A\rangle$, respectively. At equilibrium, their energies are degenerate, and the energy-gap term is zero. At time t , the vibrations of the crystal at finite temperature can drive the diabatic energies apart, yielding a finite energy gap Δ .

In the spirit of linear response, typically appropriate for a normal mode analysis, the relevant dynamical quantity for characterizing trapped-hole diffusion is the energy-gap correlation function

$$C(t) = \langle\Delta(0)\Delta(t)\rangle, \quad (5.13)$$

where $C(t)$ is, as usual, complex and can be broken up into its real and imaginary parts,

$$C(t) = C'(t) + iC''(t). \quad (5.14)$$

The average $\langle \Delta(0)\Delta(t) \rangle$ is taken with respect to the ground state (no phonon excitations), i.e. the equilibrium wave function.

Following our formalism for the vibrational spectrum of PTFE in Chapter 4, evaluating Eq. 5.13 formally requires an expansion over the normal modes of the system since Δ only depends on the phonon creation/annihilation operators. For large surface slabs even half the size of the $2 \times 2 \times 8$ slabs we employ in Chapters 2-3, calculating the phonon spectrum is a near-impossible feat. In principle, one could parallelize the calculation over a large number of cores to ensure the calculation completes in due time; however, performing a phonon calculation requires a determination of the equilibrium structure as close as possible to the true minimum. This requires very accurate forces, converged to the order 10^{-4} eV/Å or better, typically, which is very difficult to achieve for a surface slab. Furthermore, even if we could achieve such a force convergence, there is no guarantee for such a large system that we will find the global minimum, which could spell problems for a brute-force phonon calculation, like what we performed in Chapter 4.

If we assume for a moment we could calculate the normal modes directly using density functional theory, we would formally evaluate the expression for $C(t)$, similar to our approach with PTFE in Chapter 4, and limit to the single-particle excitation space upon promoting the expression to second quantization. This yields

$$C(t) = \sum_{\nu} e^{i\omega_{\nu} t} \left(\lambda_{\nu}^A - \lambda_{\nu}^D \right)^2, \quad (5.15)$$

where we have used the Heisenberg operator

$$\Delta(t) = e^{iH_{vib}t} \Delta(0) e^{-iH_{vib}t}. \quad (5.16)$$

H_{vib} is the vibrational Hamiltonian corresponding to the phonon bath since the phonons are the relevant states influencing the energy-gap fluctuations (Eq. 5.12).

A useful task for quantifying the effect of the phonon bath on the system Hamiltonian is to calculate the Fourier transform of this correlator,

$$C(\omega) = \int_{-\infty}^{\infty} dt e^{-i\omega t} C(t) = 2\pi \sum_{\nu} \left(\lambda_{\nu}^A - \lambda_{\nu}^D \right)^2 \delta(\omega - \omega_{\nu}). \quad (5.17)$$

This is a task we can perform numerically for any $C(t)$, which is especially important since we will not be able to calculate the phonon modes directly, and we will not have a formal expression for Eq. 5.15. This new correlation function has a few interesting properties. First,

$$C(\omega) = C'(\omega) + C''(\omega) \quad (5.18)$$

where $C(\omega)$ is real, and

$$C'(\omega) = \frac{C(\omega) + C(-\omega)}{2} \quad (5.19)$$

$$C''(\omega) = \frac{C(\omega) - C(-\omega)}{2} \quad (5.20)$$

are the real symmetric and antisymmetric parts, respectively. $C(\omega)$ is often called the “spectral density” of the bath states.⁹⁹ Second, with these definitions, we can immediately calculate the reorganization energy from the antisymmetric part of the spectral density,⁸⁵

$$\lambda = \frac{1}{\pi} \int_0^{\infty} d\omega \frac{C''(\omega)}{\omega}. \quad (5.21)$$

We then write down

$$C''(\omega) = \pi \sum_{\nu} \left(\lambda_{\nu}^A - \lambda_{\nu}^D \right)^2 \left(\delta(\omega - \omega_{\nu}) - \delta(\omega + \omega_{\nu}) \right). \quad (5.22)$$

Upon substitution into Eq. 5.21, we find only the positive frequencies yield non-zero contributions. We put \hbar back into the equations to arrive at the dimension-full

$$\lambda = \sum_{\nu} \frac{(\lambda_{\nu}^A - \lambda_{\nu}^D)^2}{\hbar\omega_{\nu}}, \quad (5.23)$$

which is precisely the reorganization energy we state in Chapter 2.

5.2.2 Molecular Dynamics

We cannot evaluate Eq. 5.17, and thus Eq. 5.23, directly if we cannot calculate the vibrational Hamiltonian. Furthermore, even if we could calculate the vibrational Hamiltonian, we could not extract the electron–phonon coupling terms without fitting to experimental data, which was our approach for the vibrational spectrum of PTFE (Chapter 4).

However, we *can* simulate the effect of a phonon bath by running molecular dynamics at some finite temperature below the melting point and allowing the electronic structure and nuclear configurations to evolve in time. The energy-gap operator, Δ , will oscillate in time according to the motion of the atoms, the latter of which is governed by the fundamental normal modes. Therefore, we aim to calculate $\Delta(t)$ explicitly at each point in time without knowing the normal modes, and from this, evaluate the reorganization energy, Eq. 5.21. In doing so, not only will we extract an approximate reorganization energy corresponding to the crystal part of the total reorganization, but we will also probe the most important phonon modes and extract their corresponding electron–phonon couplings.

Calculating $\Delta(t)$ without the phonon modes requires a trick. Because the formal evaluation of Eq. 5.13 involves an average over the equilibrium wave function, we propose that we can use the equilibrium unitary transformations, $\{U(\mathbf{k})\}$, obtained during the Wannier localization procedure in Chapter 3 to transform the adiabatic solutions to a diabatic representation at each time-step in the simulation. Therefore, our goal is to perform Born–Oppenheimer molecular dynamics to generate a set of adiabatic energies — the single-particle

eigenvalues — at each time-step, and we will then transform the adiabatic electronic structure at each step to a diabatic representation consistent with the equilibrium wave function. Upon running for a sufficiently long time T , we can numerically calculate Eq. 5.17 and then Eq. 5.21.

Appendix A

Supplementary Information for Chapter 2: On the Nature of Trapped-Hole States in CdS Nanocrystals and the Mechanism of Their Diffusion*

A.1 Derivation of the Diffusion Constants, D_{\parallel} and D_{\perp}

We begin with a hole state located at site m as described in Chapter 2. Here, we define this site m to be at the position (i, j) , where i denotes the x -component and j denotes the y -component, and i and j take on discrete, integer values (Figure A.1). In Figure A.1, we define the crystal c -axis and orthorhombic x - y plane exactly as they are in Chapter 2, with the crystal c -axis coinciding with the orthorhombic y -axis. We have rotated the lattice in the x - y plane clockwise by 90 degrees with respect to what is shown in Chapter 2 (“Top View” of Figure 2.1B, and Figure 2.4B) so that the x - and y -axis are now positioned in the typical fashion.

Utterback *et al.*³⁰ discovered that surface-trapped holes in CdS nanorods execute a diffusive random walk at room temperature. The equation governing the time evolution of a random walker starting at position $m = (i, j)$ and moving to any of its 8 nearest- or

*Adapted with permission from Cline, R. P.; Utterback, J. K.; Strong, S. E.; Dukovic, G.; and Eaves, J. D. *J. Phys. Chem. Lett.* **2018**, *9*, 3532–3537. (Copyright © 2018, American Chemical Society).

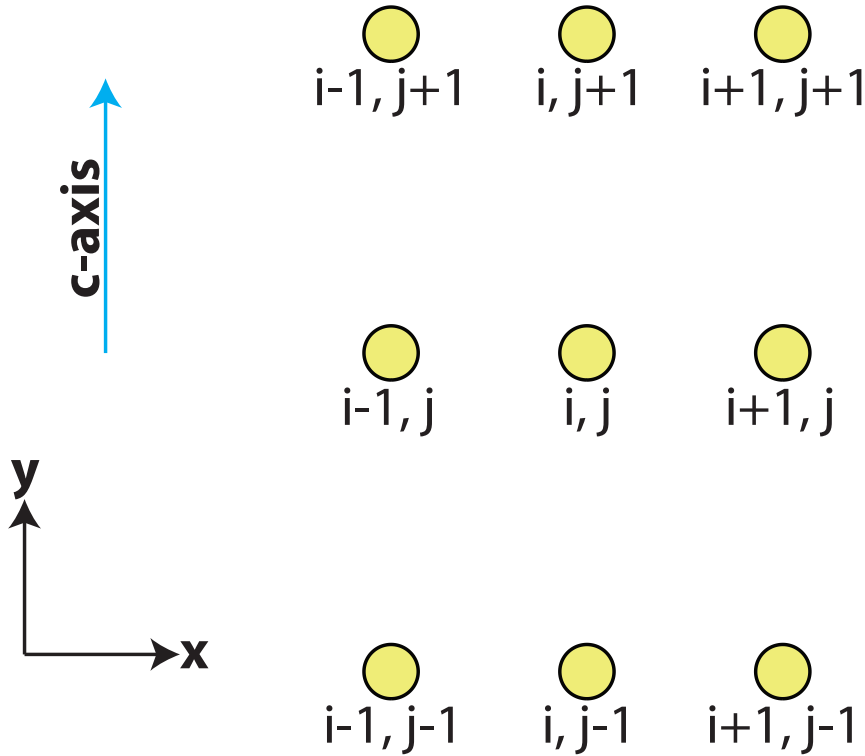


FIGURE A.1: Schematic of the surface sulfur sites. A hole located at position (i, j) can jump to any of its nearest- and next-nearest-neighbors. Nearest-neighbors include $(i \pm 1, j)$ in the horizontal direction and $(i, j \pm 1)$ in the vertical direction. Next-nearest-neighbors include the remaining positions: $(i \pm 1, j \pm 1)$. The crystal c -axis and orthorhombic x - y plane are defined exactly as they are in Chapter 2. We have rotated the lattice in the x - y plane clockwise by 90 degrees with respect to what is shown in Chapter 2 (Figure 2.1B, and Figure 2.4B) so that the x - and y -axis are now positioned in textbook fashion (horizontal x , vertical y).

next-nearest-neighbors is

$$\begin{aligned} \frac{dP_{i,j}(t)}{dt} = & k_{\perp} \left[P_{i+1,j}(t) + P_{i-1,j}(t) - 2P_{i,j}(t) \right] \\ & + k_{\parallel} \left[P_{i,j+1}(t) + P_{i,j-1}(t) - 2P_{i,j}(t) \right] \\ & + k' \left[P_{i+1,j+1}(t) + P_{i-1,j-1}(t) - 2P_{i,j}(t) \right] \\ & + k' \left[P_{i+1,j-1}(t) + P_{i-1,j+1}(t) - 2P_{i,j}(t) \right], \end{aligned} \quad (\text{A.1})$$

where $P_{i,j}(t)$ is the probability of finding a hole at position $m = (i, j)$ at time t ; k_{\perp} , k_{\parallel} , and k' are the rates corresponding to the possible paths of motion (see Figure 2.4B in Chapter

2). We define nearest-neighbors to be “on axis” in both dimensions at the positions $(i \pm 1, j)$ and $(i, j \pm 1)$, and we define next-nearest-neighbors to be “off axis” at positions $(i \pm 1, j \pm 1)$. In what follows, we derive the solution to Eq. A.1 using approximation techniques and arrive at an anisotropic two-dimensional diffusion equation with two uncoupled diffusion constants, D_{\parallel} and D_{\perp} . The approach we take here follows the derivation for one-dimensional diffusion presented in Ref. [100].

We first convert to a probability density $\mathcal{P}(x, y, t)$ by introducing a unit of area, $dA = \alpha\epsilon = \xi\epsilon^2$, such that

$$P_{i,j}(t) = \mathcal{P}(x, y, t)dA, \quad (\text{A.2})$$

where x and y describe the positions i and j , respectively. The lengths, α and ϵ , correspond to the DFT-relaxed lattice spacings between sulfur atoms in the x - and y -directions, respectively, and their values are $\alpha = 4.2040 \text{ \AA}$ and $\epsilon = 6.8417 \text{ \AA}$. The quantity $\xi = \alpha/\epsilon$ is a fixed aspect ratio of the lattice spacings on the rectangular lattice. We now convert Eq. A.1 to a diffusion equation for the probability density, $\mathcal{P}(x, y, t)$. Using the aspect ratio, ξ , to put all lengths in terms of ϵ , we find

$$\begin{aligned} \partial_t \mathcal{P}(x, y, t) &= k_{\perp} \left[\mathcal{P}(x + \xi\epsilon, y, t) + \mathcal{P}(x - \xi\epsilon, y, t) - 2\mathcal{P}(x, y, t) \right] \\ &\quad + k_{\parallel} \left[\mathcal{P}(x, y + \epsilon, t) + \mathcal{P}(x, y - \epsilon, t) - 2\mathcal{P}(x, y, t) \right] \\ &\quad + k' \left[\mathcal{P}(x + \xi\epsilon, y + \epsilon, t) + \mathcal{P}(x - \xi\epsilon, y - \epsilon, t) - 2\mathcal{P}(x, y, t) \right] \\ &\quad + k' \left[\mathcal{P}(x + \xi\epsilon, y - \epsilon, t) + \mathcal{P}(x - \xi\epsilon, y + \epsilon, t) - 2\mathcal{P}(x, y, t) \right]. \end{aligned} \quad (\text{A.3})$$

Our focus is to capture diffusion along the y -axis to compare with the results presented in Ref. [30]; therefore, we want to expand each term in Eq. A.3 asymptotically in ϵ . For

any point (x, y) , this yields

$$\mathcal{P}(x, y, t) = \mathcal{P}^{(0)}(x, y, t) + \epsilon \mathcal{P}^{(1)}(x, y, t) + \epsilon^2 \mathcal{P}^{(2)}(x, y, t) + \dots, \quad (\text{A.4})$$

where the $\{\mathcal{P}^{(i)}\}$ are analytic functions. In the derivation to come, we only take Eq. A.4 out to first order in ϵ for reasons that will soon become clear. Since the $\{\mathcal{P}^{(i)}\}$ are analytic functions in x and y , they also have Taylor series expansions close to (x, y) . For this derivation, we only need to take each Taylor expansion out to second-order; all odd-ordered terms cancel after substitution into Eq. A.3. For compactness, we will temporarily suppress the time variable, t . Substituting Eq. A.4 into Eq. A.3 and Taylor expanding each relevant term to second-order, we find

$$\begin{aligned} \partial_t \mathcal{P}(x, y) &\approx \partial_t \left[\mathcal{P}^{(0)}(x, y) + \epsilon \mathcal{P}^{(1)}(x, y) \right] \\ &\approx k_{\perp} \left[\xi^2 \epsilon^2 \partial_x^2 \mathcal{P}^{(0)}(x, y) + \epsilon \left(\xi^2 \epsilon^2 \partial_x^2 \mathcal{P}^{(1)}(x, y) \right) \right] \\ &\quad + k_{\parallel} \left[\epsilon^2 \partial_y^2 \mathcal{P}^{(0)}(x, y) + \epsilon \left(\epsilon^2 \partial_y^2 \mathcal{P}^{(1)}(x, y) \right) \right] \\ &\quad + k' \left[2\xi^2 \epsilon^2 \partial_x^2 \mathcal{P}^{(0)}(x, y) + 2\epsilon^2 \partial_y^2 \mathcal{P}^{(0)}(x, y) + \epsilon \left(2\xi^2 \epsilon^2 \partial_x^2 \mathcal{P}^{(1)}(x, y) + 2\epsilon^2 \partial_y^2 \mathcal{P}^{(1)}(x, y) \right) \right]. \end{aligned} \quad (\text{A.5})$$

It is notable that the second-order cross terms from the Taylor expansions cancel due to the symmetry of the problem and do not appear in Eq. A.5. Upon rescaling time¹⁰⁰ as $\tau = \epsilon^2 t$ and collecting like terms, we arrive at

$$\partial_{\tau} \mathcal{P}^{(0)}(x, y, \tau) \approx \left[k_{\perp} \xi^2 \partial_x^2 + k_{\parallel} \partial_y^2 + k' (2\xi^2 \partial_x^2 + 2\partial_y^2) \right] \mathcal{P}^{(0)}(x, y, \tau) \quad (\text{A.6})$$

$$\partial_{\tau} \mathcal{P}^{(1)}(x, y, \tau) \approx \left[k_{\perp} \xi^2 \partial_x^2 + k_{\parallel} \partial_y^2 + k' (2\xi^2 \partial_x^2 + 2\partial_y^2) \right] \mathcal{P}^{(1)}(x, y, \tau). \quad (\text{A.7})$$

The above expressions illustrate that $\mathcal{P}^{(0)}(x, y, \tau)$ and $\mathcal{P}^{(1)}(x, y, \tau)$ have the same form, with $\mathcal{P}^{(1)}(x, y, \tau)$ providing higher-order corrections to the full $\mathcal{P}(x, y, \tau)$. Therefore, to *lowest order* in ϵ , the distribution $\mathcal{P}^{(0)}(x, y, \tau)$ captures the relevant physics for diffusion on

a rectangular lattice. We do not asymptotically expand to higher orders because this would involve terms that correspond to the fast fluctuations of the lattice spacing. We assume such fluctuations average out for surface-trapped hole diffusion over the length-scales of the nanorods studied by Utterback *et al.*³⁰ Putting the unscaled time, t , back into Eq. A.6, we arrive at the final two-dimensional diffusion equation,

$$\begin{aligned}\partial_t \mathcal{P}^{(0)}(x, y, t) &= \left[k_{\perp} \alpha^2 \partial_x^2 + 2k' \alpha^2 \partial_x^2 + k_{\parallel} \epsilon^2 \partial_y^2 + 2k' \epsilon^2 \partial_y^2 \right] \mathcal{P}^{(0)}(x, y, t) \\ &= \left[D_{\perp} \partial_x^2 + D_{\parallel} \partial_y^2 \right] \mathcal{P}^{(0)}(x, y, t),\end{aligned}\quad (\text{A.8})$$

which depends on two uncoupled diffusion constants:

$$D_{\perp} = \alpha^2(k_{\perp} + 2k') \quad (\text{A.9})$$

$$D_{\parallel} = \epsilon^2(k_{\parallel} + 2k'). \quad (\text{A.10})$$

Here, D_{\perp} governs diffusion around the waist of a nanorod, and D_{\parallel} governs diffusion down the c -axis of a nanorod. Utterback *et al.*³⁰ observed trapped-hole diffusion along the c -axis of their CdS nanorods, and from their experimental data, they calculated an upper bound for the corresponding diffusion constant, D_{\parallel} . They did not put a bound on D_{\perp} , and such an estimate is currently unknown; therefore, the focus of this work is dedicated only to D_{\parallel} . Lastly, because the value of D_{\parallel} depends on the lattice spacing between surface sulfur atoms in the crystal c -direction, we replace ϵ from Eq. A.10 with the letter c in Chapter 2, yielding the final reported equation,

$$D_{\parallel} = c^2(k_{\parallel} + 2k'). \quad (\text{A.11})$$

A.2 Crystal Structure / VASP Convergence Details

A.2.1 Bulk Cell Parameters

The CdS bulk unit cell comprises four atoms with the following fractional positions: $(0, 0, 0)$ and $(\frac{1}{3}, \frac{2}{3}, \frac{1}{2})$ for Cd; $(0, 0, 0.37715)$ and $(\frac{1}{3}, \frac{2}{3}, 0.87715)$ for S.¹⁰¹ We define the corresponding unit cell with lattice parameters $a = 4.136$ and $c = 6.713$ and the vectors $(a, 0, 0)$, $(-\frac{a}{2}, \frac{a\sqrt{3}}{2}, 0)$, and $(0, 0, c)$. These definitions yield a wurtzite crystal structure. Using these parameters, we construct a $2 \times 2 \times 2$ bulk supercell and a $3 \times 3 \times 4$ bulk supercell. We will discuss the reasons for the latter bulk cell in the coming sections (section A.2.4). We create all variants of surface “slab” supercells from these two bulk cells. All VASP (Vienna *Ab initio* Simulation Package)^{73–78} calculations presented are non spin-polarized, and we enforce a 520 eV plane-wave energy cutoff (1.9 times the default). All k-point meshes are centered at the Γ -point. All structural relaxations make use of the conjugate gradient algorithm.

A.2.2 Bulk Convergence Details

For the $2 \times 2 \times 2$ supercell, we use a $6 \times 6 \times 4$ k-point mesh, which converges the energy to less than 0.01 meV/atom relative to the most dense k-point mesh we considered, a $24 \times 24 \times 16$ mesh. We achieve similar convergence for the $3 \times 3 \times 4$ supercell by using a $4 \times 4 \times 2$ k-point mesh. We relax all degrees of freedom (ionic positions, cell volume, and cell shape) for each bulk supercell and employ the tetrahedron method with Blöchl corrections as the method of smearing. For bulk CdS, this method is variational since no partial occupancies appear in the band structure. We use an additional support grid for the evaluation of augmentation charges, in combination with “high” precision and an augmentation-charge cutoff energy of 520 eV, to reduce the noise in the forces. We find “high” precision works better than the more modern “accurate” precision by providing the smallest noise in forces for bulk CdS at a 520 eV plane-wave cutoff. Using these settings, we require strict cutoffs of 1×10^{-4} eV/ \AA for the force convergence and 1×10^{-9} eV for the energy convergence of each ionic step.

A.2.3 $(10\bar{1}0)$ Surface Slab Parameters

According to Sun and Ceder,⁶⁴ one can define the $(10\bar{1}0)$ Miller-Bravais facet of a hexagonal/wurtzite cell with a simple orthorhombic cell by performing a symmetry transform of the old hexagonal coordinates. Such a transformation is useful because defining a surface slab cell with completely orthorhombic coordinates minimizes k-point dispersion errors during a calculation.⁶⁴ Furthermore, this transformation makes band structure and density of states (DOS) calculations unambiguous in terms of k-point sampling. Indeed, previous work by Rantala *et al.*⁶² defined a CdS $(10\bar{1}0)$ surface with an orthorhombic cell. Using the code presented by Sun and Ceder,⁶⁴ we successfully transform the coordinates of the DFT-relaxed bulk supercells to orthorhombic coordinates, and with the z -axis perpendicular to the $(10\bar{1}0)$ facet. Here and in Chapter 2, we refer to the dimensions of the surface slabs using the new orthorhombic x - y - z coordinates instead of the original wurtzite a - b - c coordinates. The various surface slab sizes we consider are as follows:

- two $2 \times 2 \times 8$ surfaces (symmetric and asymmetric),
- one $2 \times 2 \times 3$ surface (asymmetric),
- one $3 \times 4 \times 3$ surface (asymmetric),

where the symmetric and asymmetric labels correspond to the passivation/relaxation scheme we employ (see section A.2.5).

We vary the thickness and relaxation scheme between slabs to test for convergence of the surface geometry, which is important for achieving convergence of the tunneling matrix elements (results in Table A.1). We only report on the $2 \times 2 \times 8$ symmetric surface slab in Chapter 2. As evident from the dimensionalities, we construct all $2 \times 2 \times N$ surface slabs from the DFT-relaxed $2 \times 2 \times 2$ bulk supercell, and we construct the thin, wide $3 \times 4 \times 3$ surface slab from the DFT-relaxed $3 \times 3 \times 4$ bulk supercell. The mismatch of the indices between the $3 \times 4 \times 3$ surface slab and the $3 \times 3 \times 4$ bulk supercell arises from the change

to orthorhombic coordinates, where the wurtzite c -axis (third index for the bulk supercell) coincides with the orthorhombic y -axis (second index for the surface slab).

A.2.4 $3 \times 4 \times 3$ “Anti-Aliased” Surface Slab

The purpose of constructing a wide $3 \times 4 \times 3$ surface slab (3×4 surface, 3 layers in thickness) is to determine if wave function aliasing is an issue for the Wannier localization procedure. We use a $3 \times 4 \times 3$ slab instead of a $3 \times 3 \times 3$ slab because pseudohydrogen passivation (see section A.2.5) introduces fractional electrons per individual species, and a $3 \times 4 \times 3$ slab guarantees that the total electron count is a whole number. The concern for the wave function aliasing effect is that the distances between nearest-neighbor sulfur atoms on the surface are roughly $L/2$ apart in the $2 \times 2 \times N$ slabs, where L is the length of the slab cell in either the x - or y -direction. This $L/2$ separation is the greatest distance two neighboring surface sulfur atoms can be from each other in the $2 \times 2 \times N$ periodic system, suggesting that unphysical interactions with their periodic images may occur. Because of this, one could conclude that the periodic copies of the electron density calculated by VASP lead to unphysical delocalization of the final diabatic states. This would lead to artificially high values of the tunneling matrix elements presented in Chapter 2, thereby implying diffusion is “fast” relative to the actual value. Our findings for the $3 \times 4 \times 3$ surface slab, located in Table A.1, suggest that wave function aliasing is not an issue since the calculated tunneling matrix elements are nearly identical to those of the $2 \times 2 \times 3$ slab, which was relaxed using comparable settings (see Table A.1).

A.2.5 Pseudohydrogen Passivation and Ionic Relaxation Scheme

For all surface slabs, we begin by capping all surface cadmium and sulfur atoms with their respective pseudohydrogen (PH) species. We relax the positions of the PH atoms until the forces they experience fall below 10 meV/Å to ensure proper passivation and to ensure all slabs start from similar initial conditions. From here, we construct the symmetric and

asymmetric cases as follows. For the symmetric $2 \times 2 \times 8$ case (Figure A.2A), we uncap all sulfur atoms on both surfaces, leaving only the surface cadmium atoms passivated. We

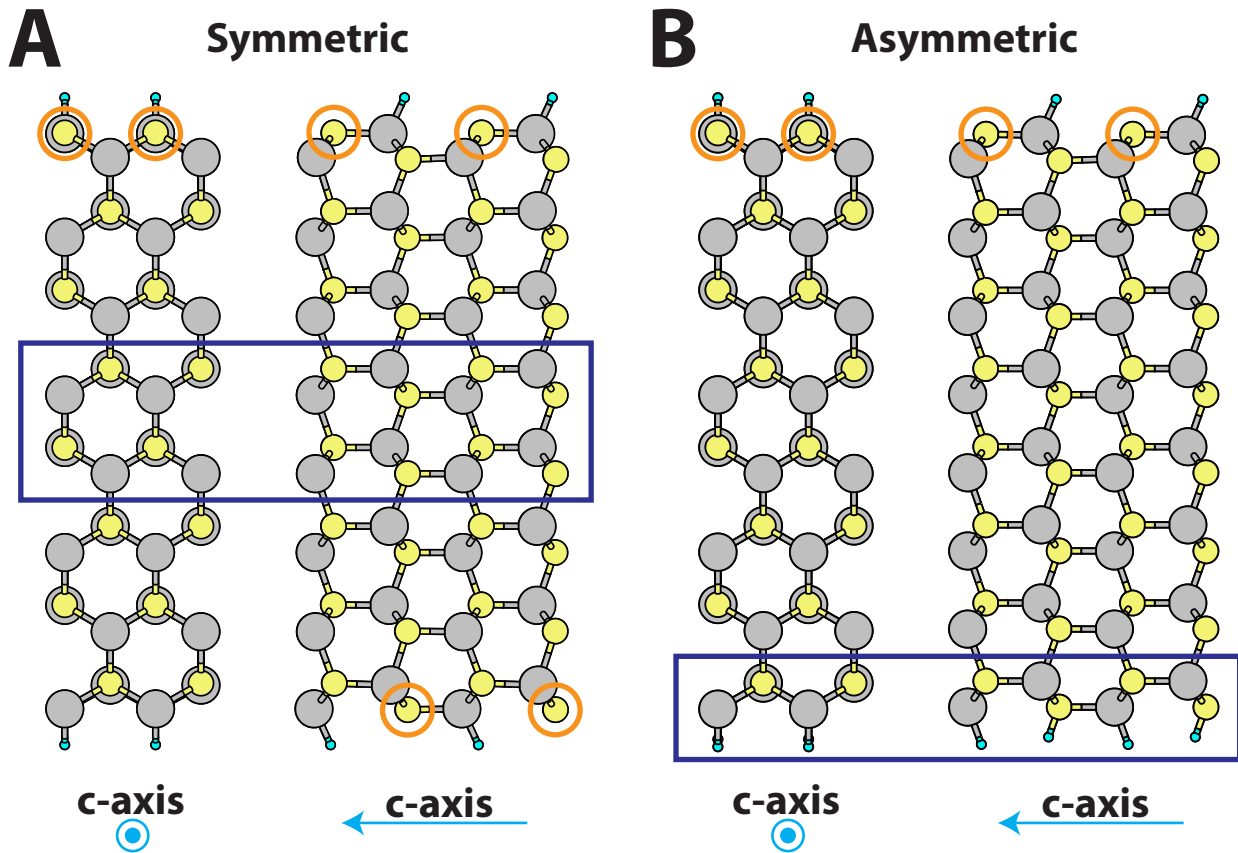


FIGURE A.2: Side views of $2 \times 2 \times 8$ symmetric and asymmetric surface slabs. Cadmium atoms are gray, sulfur atoms are yellow, and pseudohydrogen (PH) passivants are blue. Surface sulfur atoms are labeled with orange circles. The regions boxed in dark blue contain the fixed, “bulk-like” atoms. (A) The symmetric slab. Only the surface cadmium atoms are passivated in the slab, leaving all surface sulfur atoms undercoordinated by 1 bond. The boxed region contains 2 layers of CdS. (B) The asymmetric slab. PH atoms passivate all cadmium and sulfur atoms on the bottom surface. Cadmium atoms on the top surface are also passivated, while sulfur atoms on the top surface are undercoordinated by 1 bond. The boxed region contains 1 layer of PH atoms and 1 layer of CdS. The thinner asymmetric slabs (not shown) follow the same passivation scheme as the $2 \times 2 \times 8$ asymmetric slab.

hold the middle 2 layers of CdS fixed at their initial positions and relax all other atoms in a “middle-out” manner, thereby simulating surface-like behavior at both ends. For all asymmetric surface variants (Figure A.2B), we keep full passivation on the bottom surface to completely eliminate surface states arising from that layer. On the top surface, we remove all sulfur-capped PH species and leave the cadmium passivation intact, thus simulating the

presence of hole states on the top surface only. We enforce that the bottom layer of PH and the adjacent layer of CdS represent the “bulk-like” part of the system during relaxation by keeping their positions fixed at all times. We allow all other atoms to relax. We do not charge the system or account for differences in geometry between the uncharged and charged systems for any calculation. Thus, we employ the Condon and frozen orbital approximations for all calculations.

A.2.6 Surface Convergence Details

For the slab calculations, we turn symmetrization protocols off except for $\Psi(\mathbf{k}) = \Psi^*(-\mathbf{k})$, where $\Psi(\mathbf{k})$ is the Bloch state at wave vector \mathbf{k} . This corresponds to setting ISYM = 0 in VASP. During relaxations, we require a force convergence cutoff of 10 meV/Å and an energy convergence cutoff of 1×10^{-6} eV for each ionic step. We employ Gaussian smearing during geometry relaxations, keeping the cell shape and volume fixed. The tetrahedron method is not viable for our surface slab relaxations because of partial occupancies in the band structure that arise from the undercoordinated sulfur atoms at the surface. We again use an additional support grid for the evaluation of augmentation charges. For all calculations except the $2 \times 2 \times 8$ surfaces, we use “accurate” precision because this minimizes the noises in the forces. For the $2 \times 2 \times 8$ variants, however, we find the “high” precision tag with an augmentation-charge cutoff energy of 750 eV provides the best accuracy in the forces.

Keeping the previous settings fixed, we carry out numerous convergence tests for the tunneling matrix elements, t_{\perp} , t_{\parallel} , and t' , using the slabs mentioned in section A.2.3. To test for convergence for each slab, we vary the k-point density and the smearing width since partial occupancies arise in the band structure near the Fermi energy, E_F . These partial occupancies require that we carefully sample the Brillouin zone to achieve the most accurate ground-state surface geometry. The results, summarized in Table A.1, show that the matrix elements are fairly insensitive to the k-point mesh and smearing width choices we considered,

implying that our lowest-quality choices are adequate for finding the approximate ground-state surface structure. This is especially evident in the results for the symmetric $2 \times 2 \times 8$ slab, where all variants yield $|t_{\parallel}| \approx |t'| \approx 3$ meV and $|t_{\perp}| \approx 80$ meV. The calculated lower bound on the reorganization energy, $\lambda \geq 1$ eV, is the same for all calculations presented in Table A.1. We use 293 K as the definition for room temperature when calculating λ .

surface	k-points	smearing (meV)	$ t_{\perp} $ (meV)	$ t_{\parallel} $ (meV)	$ t' $ (meV)
$2 \times 2 \times 3$	$6 \times 4 \times 1$	50	79.1	2.2	3.6
	$8 \times 5 \times 1$	2	79.1	2.5	3.4
	$12 \times 8 \times 1$	2	79.1	2.5	3.4
$2 \times 2 \times 8(s)$	$6 \times 4 \times 1$	50	80.0	3.0	2.9
	$8 \times 5 \times 1$	10	79.8	2.9	3.0
	$8 \times 5 \times 1$	2	79.8	2.9	3.0
$2 \times 2 \times 8(a)$	$6 \times 4 \times 1$	50	79.8	2.9	2.9
	$8 \times 5 \times 1$	2	79.6	3.2	2.8
	$3 \times 4 \times 3$	4 \times 2 \times 1	79.4	2.2	3.6

TABLE A.1: Calculated tunneling matrix elements for the surface slabs. We test convergence of the matrix elements by employing various k-point meshes and Gaussian smearing widths during structural relaxations. The (s) and (a) labels for the $2 \times 2 \times 8$ surfaces denote symmetric and asymmetric, respectively. All other surfaces are asymmetric by default.

A.3 Wannier Localization Procedure

A.3.1 Wannier90: A Brief Description

Wannier90 converts the adiabatic plane-wave results to maximally localized Wannier functions (MLWFs) through a series of unitary transformations of the original Bloch states. Wannier90 quantifies the degree of localization by calculating the spatial “spread” of the orbitals, which the code minimizes to generate the MLWFs. The spread takes on units of Å². Details and additional information on these topics can be found in the Wannier90 manual and various references.^{69,79,80,82}

A.3.2 Convergence Criteria

For our system and choice of MLWF basis (sulfur-centered sp^3 orbitals), and if we include all adiabatic states as inputs to minimize selection bias, Wannier90 must complete two phases: “disentanglement” and “Wannierisation.” The former extracts the optimal subspace of states from the original DFT calculation for building the MLWFs, and the latter maximally localizes these states. For all calculations, we use the default disentanglement convergence criteria supplied by Wannier90: disentanglement terminates when the fractional change between successive iterations in the spread is less than $1 \times 10^{-10} \text{ \AA}^2$ for 3 iterations. For the Wannierisation phase, we enforce a convergence of $1 \times 10^{-11} \text{ \AA}^2$ over 10 successive iterations for the fractional change in the spread. We find that convergence is most stable when we construct sulfur-centered sp^3 orbitals throughout the entire structure. In fact, doing so leads directly to the first tight-binding Hamiltonian, \mathcal{H}_{TB} , discussed in Chapter 2.

A.3.3 The Outer and Inner Energy Windows

The two most important tunable parameters that determine how the spread is minimized are the “outer” and “inner” energy windows. The outer window should encompass any states believed to contribute to the desired diabatic picture, and the inner window should encompass only the states that need to be reproduced exactly after Wannier localization. The inner window is often called the “frozen” window for this reason. For all calculations, we set the outer window to include all states with energies $E - E_F < 0.2$ eV. This choice excludes all conduction bands that exist at energies $E - E_F > 0.2$ since we find that the conduction bands do not aid in constructing the sp^3 orbital subspace.

Determining the inner window range is a much more delicate process that requires extensive testing since the choice of inner window may dramatically alter some of the desired properties. Because the hole states localized on surface sulfur atoms correspond to the top-most bands of the valence manifold, we know that we need to preserve, *at a minimum*, the electronic properties of the region between E_F and $E_F + 0.2$ eV. Therefore, we set the initial

inner window to encompass the states in this region. Since we define the inner window maximum to coincide with the outer window maximum, this value need not change if we must preserve all states between E_F and $E_F + 0.2$ eV. Thus, the inner window minimum, which has an upper bound equal to E_F , is the only unknown variable we still need to determine for our system.

In Chapter 2, we show that the hole states are well localized on the surface sulfur atoms; therefore, we use the spread of the converged nonbonding sp^3 orbitals in the system to determine the proper inner window minimum value for all calculations. We use this as a metric for the following reason: increasing the width of the inner window for a fixed outer window range will always increase the *total* spread since the inner window imposes a constraint on the final diabatic states; however, *individual* spreads need not follow this trend. As such, we hypothesize that some value of the inner window minimum will minimize the spreads of the nonbonding sp^3 orbitals within the manifold of all sulfur-centered sp^3 orbitals. Taking into account this information, we perform numerous Wannier localizations for all slabs starting with an inner window minimum value of E_F and scanning below to the nearest meV to determine the optimal value. For this work, an inner window width of about 1.6 eV, corresponding to an inner window minimum value of approximately $E_F - 1.4$ eV, leads to maximally-localized nonbonding sp^3 orbitals for all $2 \times 2 \times 8$ slabs. For the symmetric $2 \times 2 \times 8$ slab in particular, the nonbonding sp^3 orbitals attain final spreads of $\sim 1.6 \text{ \AA}^2$, and all sp^3 orbitals in the structure in general attain spreads between 1.6 and 2.1 \AA^2 .

A.4 Alternate Electronic Structure Comparisons

A.4.1 Fully-Passivated $2 \times 2 \times 8$ Surface Slab

In Chapter 2, we mention that passivating all surface sulfur and cadmium atoms with their respective PH species gives rise to “bulk-like” behavior. Figure A.3A shows a DOS

calculation for such a fully-passivated surface slab, which we construct by taking our final $2 \times 2 \times 8$ symmetric slab (10 meV smearing width, Table A.1) and then passivating the bare sulfur atoms. We relax the positions of these PH species, holding all other atoms fixed, to ensure complete passivation of the surface sulfur dangling bonds. In this DOS, we notice no states exist immediately above the “Fermi” level, E_F , which here is defined as the energy at

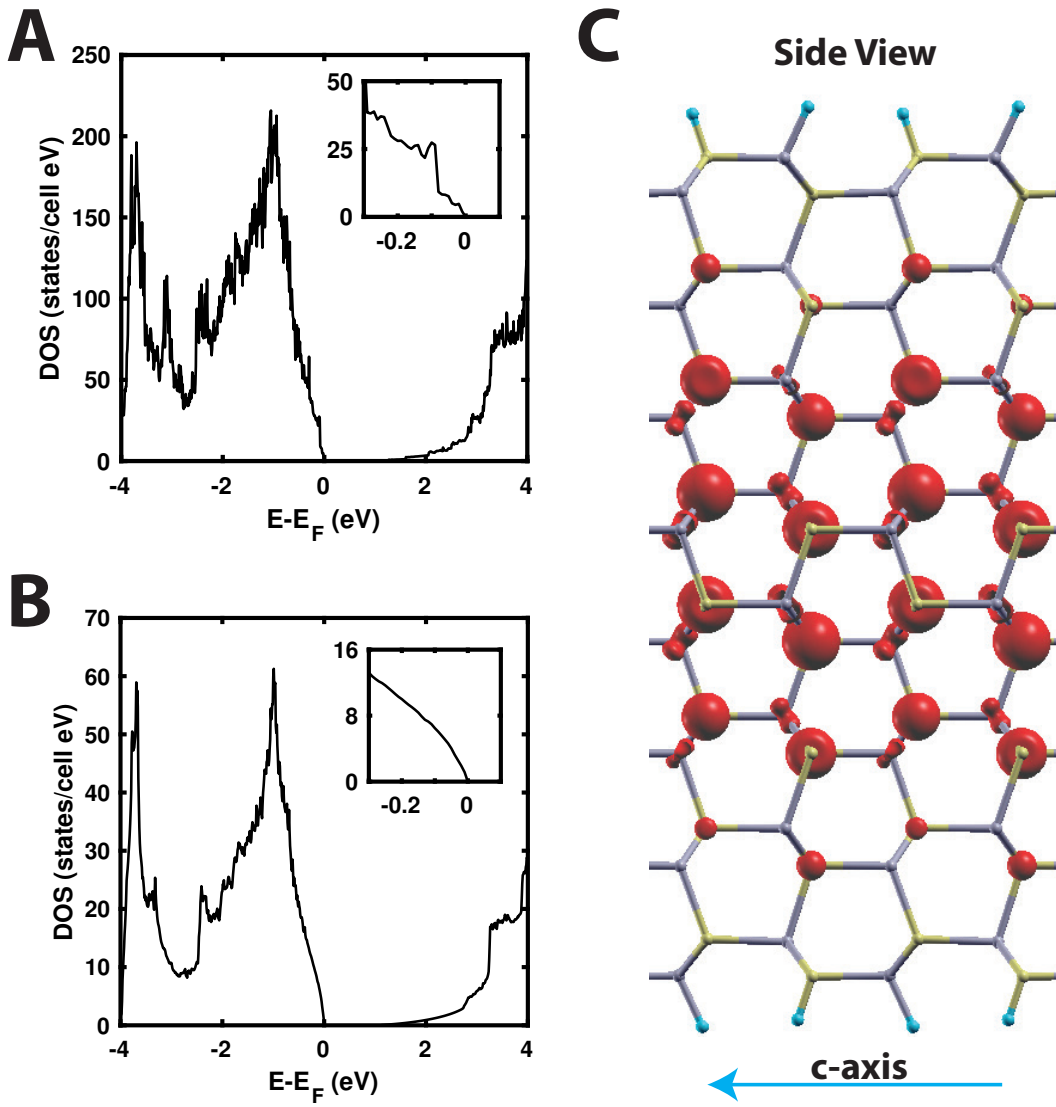


FIGURE A.3: (A) Total DOS within the range $E_F \pm 4$ eV for a fully-passivated $2 \times 2 \times 8$ surface slab, showing the elimination of states beyond E_F . (B) Total DOS within the range $E_F \pm 4$ eV for the $2 \times 2 \times 2$ bulk supercell. Qualitatively, there is virtually no difference between the two DOS calculations. (C) Fully-passivated $2 \times 2 \times 8$ surface slab electron density (red) at the valence maximum (between the range $E_F - 0.025$ eV and E_F).

the valence band maximum. *All* states below E_F are fully occupied and *all* states above E_F are completely unoccupied; no partial occupancies exist with this passivation scheme. To compare with bulk CdS, we calculate the DOS for the relaxed $2 \times 2 \times 2$ bulk supercell, shown in Figure A.3B. As evident, there is qualitatively no difference in the DOS between the fully-passivated surface slab and a bulk cell. We verify these results by inspecting the electron density for the surface slab within 25 meV below E_F . The results (Figure A.3C) show that all of the electron density in this energy range resides in the bulk of the material, *delocalized* throughout most of the structure, with no discernible states localized to the surface sulfur atoms.

A.4.2 Asymmetric $2 \times 2 \times 8$ Surface Slab

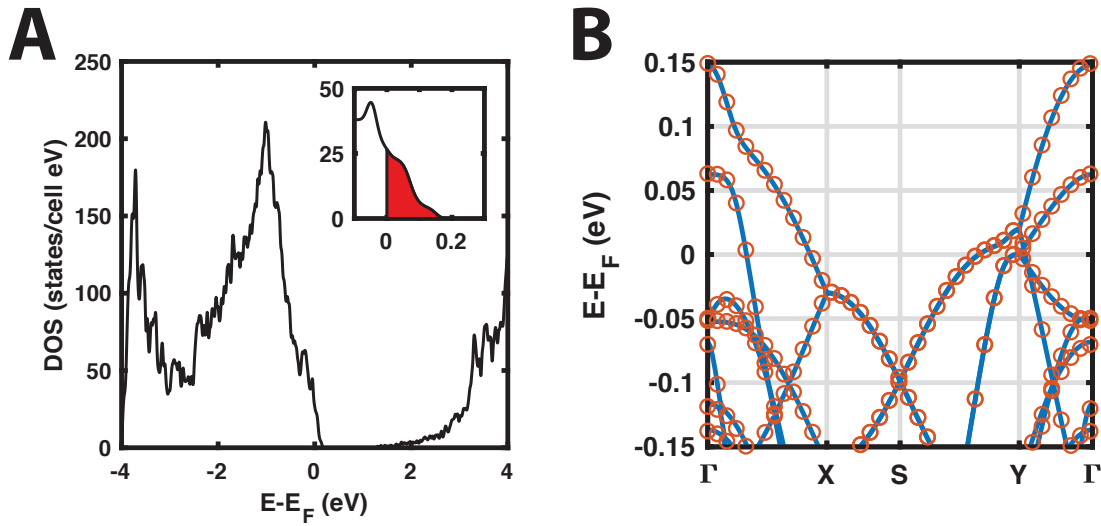


FIGURE A.4: (A) Total DOS within the range $E_F \pm 4$ eV for the $2 \times 2 \times 8$ asymmetric slab relaxed using an $8 \times 5 \times 1$ k-point mesh. We see qualitatively similar results as those described in Chapter 2. (B) Band structure calculation for the $2 \times 2 \times 8$ asymmetric slab. Again, we find qualitatively similar results with those found in Chapter 2.

Here, we compare the calculations presented in Chapter 2 for the converged $2 \times 2 \times 8$ symmetric slab to those of a $2 \times 2 \times 8$ asymmetric slab, whose final positions were calculated using an $8 \times 5 \times 1$ k-point mesh and a smearing width of 2 meV. The results for the DOS (Figure A.4A) reveal that the asymmetric and symmetric variants yield qualitatively the

same DOS, with a region between E_F and $E_F + 0.2$ eV containing bands that are mostly unoccupied. E_F here is exactly as it is in Chapter 2: the energetic point at which bands are exactly 50% occupied. An electron density calculation of the states between E_F and $E_F + 0.2$ eV for the asymmetric slab gives the same result as seen in Chapter 2, so we do not show that result here for the asymmetric slab. Figure A.4B shows the corresponding band structure for the $2 \times 2 \times 8$ asymmetric slab. Like with the DOS, we find qualitative agreement between this band structure and the one found in Chapter 2 (Figure 2.3) for the symmetric slab.

Appendix B

Supplementary Information for Chapter 3: Surface-Trapped Hole Diffusion in CdS and CdSe: The Superexchange Mechanism[†]

B.1 DFT Parameters / Convergence Details for CdSe

We discussed the parameters and convergence details for CdS in section A.2 of Appendix A. We focus solely on CdSe for the discussion of the DFT parameters here. All VASP (Vienna Ab initio Simulation Package)^{73–78} calculations presented are not spin-polarized, and we enforce a 510 eV plane-wave energy cutoff (1.85 times the default). All k-point meshes are centered at Γ . All structural relaxations make use of the conjugate gradient algorithm.

B.1.1 Bulk Calculations

We begin with a CdSe bulk unit cell corresponding to a wurtzite crystal structure, as we did in Chapter 2 for CdS. After an initial pre-convergence stage, we construct a $2 \times 2 \times 2$ bulk supercell from this unit cell. For the $2 \times 2 \times 2$ supercell, we sample the Brillouin zone with an $8 \times 8 \times 5$ k-point mesh, which converges the energy to less than 0.01 meV/atom relative to the most dense k-point mesh we considered, an $18 \times 18 \times 12$ mesh. We relax all

[†]Adapted with permission from Cline, R. P.; and Eaves, J. D. Surface-Trapped Hole Diffusion in CdS and CdSe: The Superexchange Mechanism, *submitted for publication*.

degrees of freedom (ionic positions, cell volume, and cell shape) for each bulk supercell, and we use the tetrahedron method with Blöchl corrections as the method of smearing since bulk CdSe is a pure semiconductor. To reduce the noise in the forces, we employ an additional support grid for the evaluation of augmentation charges, in combination with the “high” precision mode and an augmentation-charge cutoff energy of 440 eV. Using these settings, we enforce strict cutoffs of 1×10^{-6} eV/Å for the force convergence and 5×10^{-11} eV for the energy convergence of each ionic step. Upon final relaxation, the wurtzite lattice constants are as follows: $A = 8.782$ Å and $C = 14.337$ Å for the $2 \times 2 \times 2$ supercell, which equates to single-cell constants of $a = 4.391$ Å and $c = 7.169$ Å. We create all variants of surface “slab” supercells from this relaxed bulk $2 \times 2 \times 2$ cell.

B.1.2 Surface Slab Calculations

B.1.2.1 Surface Slab Construction

As in our previous work for CdS (Chapter 2), we use the code presented by Sun and Ceder in their work⁶⁴ to transform the coordinates of the DFT-relaxed bulk CdSe supercells from wurtzite to orthorhombic coordinates. We set the orthorhombic z -axis perpendicular to the $(10\bar{1}0)$ facet, which corresponds to the lowest-energy surface for both CdS and CdSe.⁶² Work by Rosenthal *et al.*⁴⁴ suggests that all six radial surfaces of the nanorods studied by Utterback *et al.*^{30,32,33} are the same and correspond to this facet.

Using these transformed coordinates, we construct two $2 \times 2 \times 8$ CdSe surface slabs — one symmetric and one asymmetric — where the symmetric and asymmetric labels correspond to the passivation/relaxation scheme we employ (see section B.1.2.2). When referring to the dimensions of the surface slabs, we use the new orthorhombic x – y – z coordinates as opposed to the wurtzite crystal a – b – c coordinates. We only report on the symmetric surface slab in Chapter 3, similar to our approach in Chapter 2. For both slabs, we separate periodic images of the slab in the z -direction by a vacuum spacing of roughly 21 Å in length.

B.1.2.2 Passivation/Relaxation Schemes

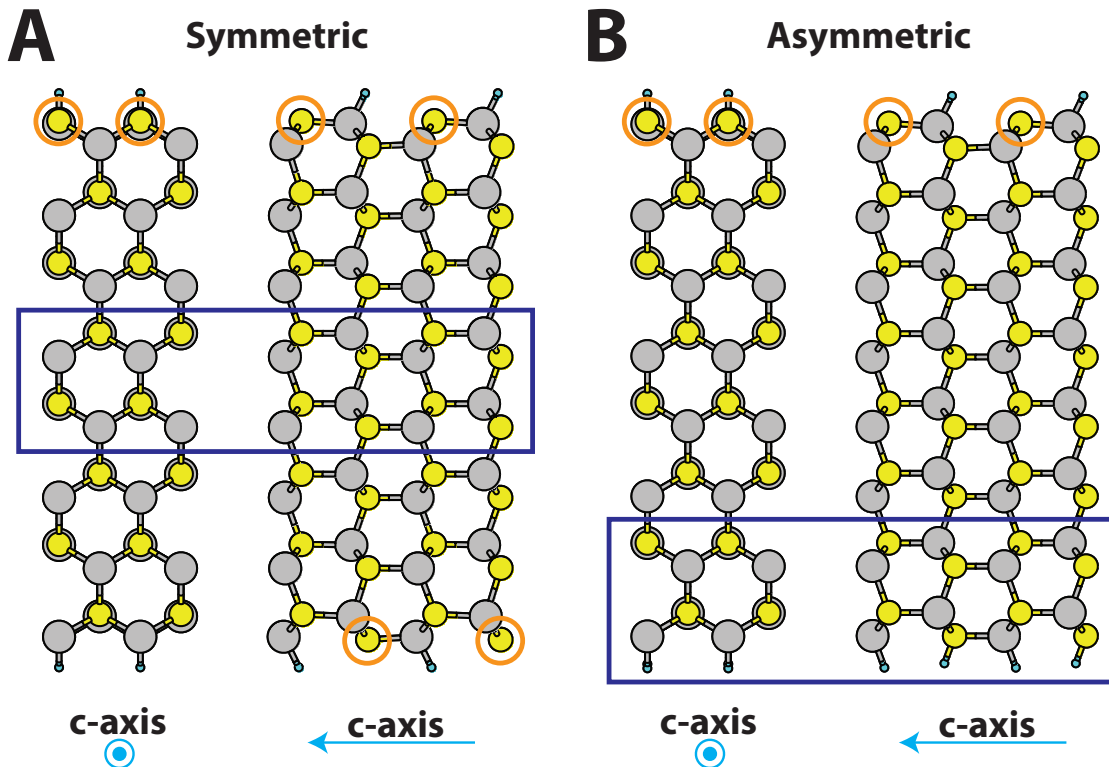


FIGURE B.1: Side views of the geometrically-relaxed $2 \times 2 \times 8$ symmetric and asymmetric CdSe slabs. Cadmium atoms are gray, selenium atoms are yellow, and pseudohydrogen (PH) atoms are blue. We use orange circles to identify the surface selenium atoms. The atoms enclosed by dark-blue boxes represent the bulk-like layers. For both slab variants, we passivate all surface cadmium atoms with the appropriate PH species. (A) For the symmetric surface slab, we do not passivate any other atom, and we hold the positions of the middle 2 layers of atoms fixed. (B) For the asymmetric surface slab, we additionally passivate the selenium atoms on the bottom layer with the appropriate PH species, and we hold the bottom 2 layers of CdSe fixed. We allow the bottom PH layer to relax to ensure proper passivation of the adjacent CdSe layer, but we still label this region as “bulk-like” since the accompanying CdSe atoms are in their bulk positions for all calculations.

For all surface slabs, we cap all surface cadmium atoms with the “H1.5” pseudohydrogen (PH) species. The “1.5” label indicates the electron count and nuclear charge are both equal to 1.5. This passivation scheme is sufficient for creating a symmetric slab (Figure B.1A). To ensure we retain a bulk-like region throughout all calculations, we hold the middle 2 layers of the symmetric CdSe slab fixed at their initial positions and relax all other atoms in a “middle-out” manner, thereby simulating surface-like behavior at both ends.

For the asymmetric $2 \times 2 \times 8$ case (Figure B.1B), we *additionally* cap all selenium atoms on the bottom surface with the “H.5” PH species, where the “.5” label indicates the electron count and nuclear charge are both equal to 0.5. To ensure we retain a bulk-like region throughout all calculations, we hold the 2 layers of CdSe adjacent to the bottom PH layer fixed at their initial positions, and we relax all other atoms. We allowed the bottom PH layer to relax to ensure proper passivation of the bottom CdSe surface. This is a slight modification from our previous method. Thus, the only true surface of interest is the top surface.

B.1.2.3 Convergence Details

For the DFT slab calculations, we turn symmetrization protocols off ($\text{ISYM} = 0$), as we did for CdS in Chapter 2, and we sample the two-dimensional Brillouin zone with an $8 \times 5 \times 1$ k-point mesh. During geometry relaxations, we require an energy convergence cutoff of 1×10^{-7} eV for each ionic step and a force convergence cutoff of 2 meV/ \AA for all movable (non-bulk) atoms. We keep the cell shape and volume fixed, and we employ Gaussian smearing to deal with partial occupancies. For the symmetric slab, relaxing the ionic positions in this manner ensures the constraint forces on the ions in the fixed central layers fall to zero to within accepted tolerance (12 meV/ \AA). To reduce the noise in the forces, we set the precision mode to “accurate” and again employ an additional support grid for the evaluation of augmentation charges.

B.1.2.4 Miscellaneous

We do not explicitly calculate any excited-state wave functions or properties for this work. We infer them from the relaxed DFT ground state by assuming the nuclear coordinates and electronic structure (i.e. the orbitals/band structure) remain fixed before and after electronic excitation. These assumptions correspond to the Condon and frozen orbital approximations, respectively.

B.2 Wannier-Basis Hamiltonian

This section describes the calculation of the Hamiltonian in the Wannier-orbital basis. This section does not represent a complete breakdown of the Wannier-orbital formalism, so we refer the reader to Ref. [69, 79, 80, 82] for any missing details. This also applies to subsequent sections describing the Wannier-orbital formalism.

A key result of the Wannier localization process is the calculation of unitary matrices, $\mathbf{U}^{\text{tot}(\mathbf{k})}$, which minimize the orbital spread functional.^{69,79,80,82} In general,

$$\mathbf{U}^{\text{tot}(\mathbf{k})} = \mathbf{U}^{\text{dis}(\mathbf{k})} \mathbf{U}^{\text{wan}(\mathbf{k})}, \quad (\text{B.1})$$

where “wan” indicates the “wannierisation”⁷⁹ phase, “dis” indicates the “disentanglement”⁸⁰ phase, and “tot” indicates the total transformation. In Ref. [69, 79, 80, 82], $\mathbf{U}^{\text{wan}(\mathbf{k})}$ is simply called $\mathbf{U}^{(\mathbf{k})}$, and $\mathbf{U}^{\text{tot}(\mathbf{k})}$ is never explicitly defined. We make such distinctions here for added clarity.

The Wannier90 code performs a disentanglement phase whenever the number of desired Wannier orbitals is less than the number of input bands. When the number of Wannier orbitals equals the number of input bands, there is no disentanglement phase, which is equivalent to setting $\mathbf{U}^{\text{dis}(\mathbf{k})} = \mathbf{1}$. The wannierisation phase is always performed, and corresponds to the full minimization of the orbital spread functional.

Once we have the unitary transformations, we first evaluate the Hamiltonian in the rotated Bloch basis,

$$H^{(W)}(\mathbf{k}) = (\mathbf{U}^{\text{tot}(\mathbf{k})})^\dagger H(\mathbf{k}) \mathbf{U}^{\text{tot}(\mathbf{k})}, \quad (\text{B.2})$$

where $H(\mathbf{k})$ is a diagonal matrix containing the eigenvalues at wave vector \mathbf{k} as computed by DFT. The (W) superscript emphasizes that these rotated Bloch states constitute the basis used to construct the Wannier orbitals. We then Fourier transform this expression over a

Bravais lattice vector, $\mathbf{R} = \mathbf{R} - \mathbf{R}'$, to find

$$H_{mn}(\mathbf{R} - \mathbf{R}') = \frac{1}{N_k} \sum_{\mathbf{k}} e^{-i\mathbf{k}\cdot(\mathbf{R}-\mathbf{R}')} H_{mn}^{(W)}(\mathbf{k}), \quad (\text{B.3})$$

where m and n are Wannier orbital indices, and N_k is the number of k-points sampled in the DFT calculation. The vectors, \mathbf{R} , are themselves Bravais lattice vectors and are provided as an output of the Wannier localization procedure, and the set $\{\mathbf{R}'\}$ is an identical copy of $\{\mathbf{R}\}$.

It is straightforward to see from Eq. B.3 that setting $\mathbf{R}' = (0, 0, 0)$ yields

$$H_{mn}(\mathbf{R}) = \frac{1}{N_k} \sum_{\mathbf{k}} e^{-i\mathbf{k}\cdot\mathbf{R}} H_{mn}^{(W)}(\mathbf{k}), \quad (\text{B.4})$$

which are the matrix elements reported in Ref. [69]. This expression only connects orbitals in some translated cell centered at \mathbf{R} to the central (input) cell centered at $\mathbf{R}' = (0, 0, 0)$. Therefore, Eq. B.4 does not represent the complete Hamiltonian, which should couple orbitals in cells \mathbf{R} and \mathbf{R}' . However, this expression is still useful for determining uniqueness.

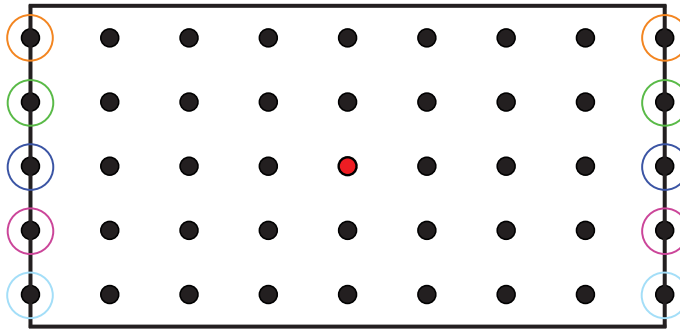


FIGURE B.2: Illustration of the real-space Wigner-Seitz (WS) supercell generated by Wannier90 for an orthorhombic input cell sampled with an $8 \times 5 \times 1$ k-point grid. Each dot represents a translation of the input cell structure in units of the cell's lattice definitions, with the red dot labeling the central cell, $\mathbf{R} = (0, 0, 0)$. Any point lying on the edge of this WS supercell is degenerate with exactly one point on the opposing edge. In particular, points encircled by the same color yield identical Hamiltonian matrix elements (Eq. B.4), and are thus degenerate with each other.

In practice, all \mathbf{R} exist in the interior and up to the surface of a Wigner-Seitz (WS) supercell as determined by the Wannier90 code (Figure B.2).^{69,79,80,82} All \mathbf{R} in the interior

are unique and non-degenerate. If a particular \mathbf{R} exists on the boundary of this WS supercell, it will be degenerate with at least one other \mathbf{R} on the boundary. Such \mathbf{R} vectors then yield identical Hamiltonian matrix elements, Eq. B.4. The exact degree of degeneracy depends on the symmetry and dimensionality of the supercell, as well as the complexity of the input crystal structure.

B.3 Mapping onto the Fano-Anderson Problem

The single-particle Fano-Anderson problem can be described with the following second-quantized Hamiltonian:

$$H_{FA} = \epsilon_s c_s^\dagger c_s + \sum_k E_k a_k^\dagger a_k + \sum_k V_{s,k} c_s^\dagger a_k + h.c., \quad (\text{B.5})$$

where c_s^\dagger (c_s) is the creation (annihilation) operator for the discrete impurity state $|s\rangle$, a_k^\dagger (a_k) the creation (annihilation) operator for continuum state $|k\rangle$, ϵ_s the energy of state $|s\rangle$, E_k the energy of state $|k\rangle$, and $V_{s,k}$ the amplitude of transition for a continuum particle hopping onto the impurity. The reverse process — an impurity particle hopping into the continuum — is contained within $h.c.$, which represents all Hermitian conjugate terms. In matrix form, this corresponds to

$$\mathbf{H}_{\text{FA}} \doteq \left(\begin{array}{c|cccc} \epsilon_s & V_{s,k_1} & V_{s,k_2} & V_{s,k_3} & \cdots \\ \hline V_{k_1,s}^\dagger & E_{k_1} & & & \\ V_{k_2,s}^\dagger & & E_{k_2} & & \\ V_{k_3,s}^\dagger & & & E_{k_3} & \\ \vdots & & & & \ddots \end{array} \right). \quad (\text{B.6})$$

Our model electronic Hamiltonian for any pair of orbitals on the surface for either CdS or CdSe has the form,

$$\mathbf{H} \doteq \left(\begin{array}{c|c} \mathbf{P}\mathbf{H}\mathbf{P} & \mathbf{P}\mathbf{H}\mathbf{Q} \\ \hline \mathbf{Q}\mathbf{H}\mathbf{P} & \mathbf{Q}\mathbf{H}\mathbf{Q} \end{array} \right), \quad (\text{B.7})$$

where \mathbf{P} and \mathbf{Q} are the projection operators defined in Chapter 3. To cast this Hamiltonian in the form of Eq. B.5-B.6, we must diagonalize the $\mathbf{P}\mathbf{H}\mathbf{P}$ and $\mathbf{Q}\mathbf{H}\mathbf{Q}$ blocks. Doing so yields

$$\mathbf{H} \doteq \left(\begin{array}{c|c} \mathbf{H}_S & \mathbf{V} \\ \hline \mathbf{V}^\dagger & \mathbf{H}_B \end{array} \right), \quad (\text{B.8})$$

where

$$\mathbf{H}_S = \mathbf{U}_S^\dagger \mathbf{P}\mathbf{H}\mathbf{P} \mathbf{U}_S, \quad (\text{B.9})$$

$$\mathbf{V} = \mathbf{U}_S^\dagger \mathbf{P}\mathbf{H}\mathbf{Q} \mathbf{U}_B, \quad (\text{B.10})$$

$$\mathbf{H}_B = \mathbf{U}_B^\dagger \mathbf{Q}\mathbf{H}\mathbf{Q} \mathbf{U}_B, \quad (\text{B.11})$$

and \mathbf{U}_S (\mathbf{U}_B) is the matrix of column vectors corresponding to the eigenstates of the system (bath) blocks.

B.4 Effect of Wannier Localization Scheme and Orbital Energies on Green's Function Analysis

The diagonal elements of Eq. B.3 — when $\mathbf{R} - \mathbf{R}' = (0, 0, 0)$ and $m = n$ — correspond to the on-site energies (OSEs) of the resulting Wannier orbitals, and are represented by ϵ_0 in Chapter 3. The values for these energies need not be the same across various localization protocols, and this effect can have potentially serious consequences for the Green's function

formalism we adopt. In particular, if the OSEs of the relevant surface nonbonding orbitals (NBOs) fluctuate significantly due to uncontrollable error, the Green’s function for the pair of $|\pm\rangle$ states involved in a single hopping event might not find a corresponding pair of stable, bound dressed $|\tilde{\pm}\rangle$ states that exist outside of the continuum’s range of energy.

In this section, we compare the orbital OSEs of the relevant surface states (the non-bonding sp^3 orbitals) for different Wannier localization procedures, and we rationalize the methodology we take in Chapter 3. We focus our attention on CdS for most of this section because the effects we discuss here affect the Green’s function analysis for system more strongly. See section B.4.3 for a brief comment on CdSe and how those results compare.

B.4.1 Wannier Localization with Disentanglement for CdS

In our previous work (Chapter 2), we employed the disentanglement procedure corresponding to the “entangled bands” methodology⁸⁰ within the Wannier90 code to find the optimal set of localized sulfur-centered sp^3 orbitals. We included all bands with energies $E - E_{Fermi} < 0.2$ eV as inputs for the calculation, and we let the code “pick out” the aforementioned sp^3 subspace as the final output. For this particular setup, the disentanglement procedure is necessary because the cadmium d-orbital bands, as well as the H1.5 s-orbital bands, exist between the sulfur s- and p-orbital bands that are required for building the sp^3 subspace. Figures B.6-B.9 in section B.4.2 illustrate this point further, along with a more complete description of those figures.

The disentanglement procedure is convenient, and sometimes necessary, because it allows the user to select all bands that *might* contribute to the desired subspace without manually deciding beforehand which bands to include or exclude. This freedom, however, comes at a cost: the resulting subspace of sp^3 bands need not match any of the input bands.⁸⁰ Because of this issue, a user-defined energy window, called the “frozen” window, can be supplied to preserve a portion of the input eigenvalues during the localization procedure. As discussed in Appendix A (section A.3.3), we determined an optimal width of roughly 1.6 eV for this frozen

window for CdS because this yielded the most-localized surface NBOs given the constraint that the eigenvalues between 0 and 0.2 eV, at a minimum, must be preserved. Figure B.3 shows the valence-region band structure for CdS to illustrate this point further.

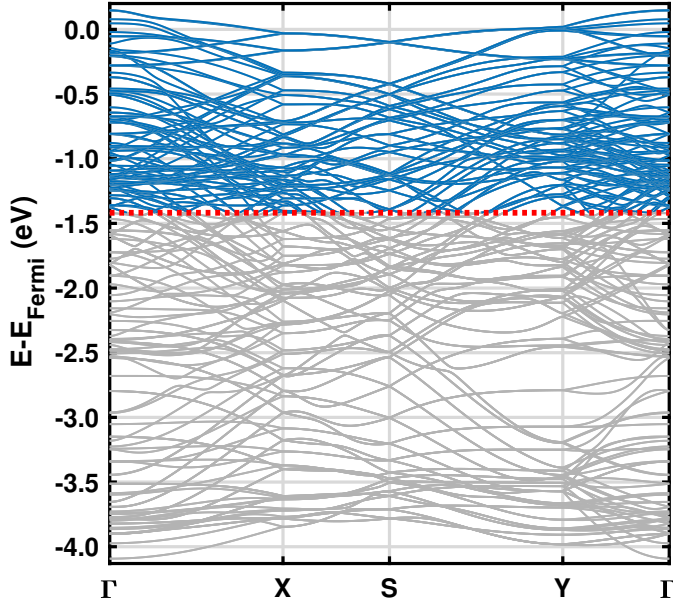


FIGURE B.3: DFT band structure for the symmetric $2 \times 2 \times 8$ CdS surface slab. We show only the valence and unoccupied states that occur just before the band gap, equating to 192 bands in total. The bands colored in blue are the frozen states, meaning they are preserved during the Wannier transformation. The bands in gray exist outside of the frozen window and are not preserved exactly. The red dotted line denotes the bottom edge of the frozen window. The top edge of the frozen window is set to just higher than the highest eigenvalue shown ($E - E_{Fermi} \approx 0.15$ eV < 0.2 eV).

While this approach was adequate for determining the direct Hamiltonian matrix elements between orbitals, the subject of Chapter 2, it requires one important modification here for calculating the superexchange corrections to these direct matrix elements. Namely, to achieve the most accurate description of superexchange relative to the parent DFT results, the entire valence region (all states in the range $-4.1 < E - E_{Fermi} < 0.2$ eV in Figure B.3) must be preserved during the localization procedure, as discussed in Chapter 3.

Upon increasing the frozen window width from 1.6 eV to the now-required 4.3 eV, we find that the orbital OSEs of the surface NBOs shift upward by nearly 0.5 eV in energy (Figure B.4). At first blush, this result seems to imply the OSEs corresponding to the smaller window

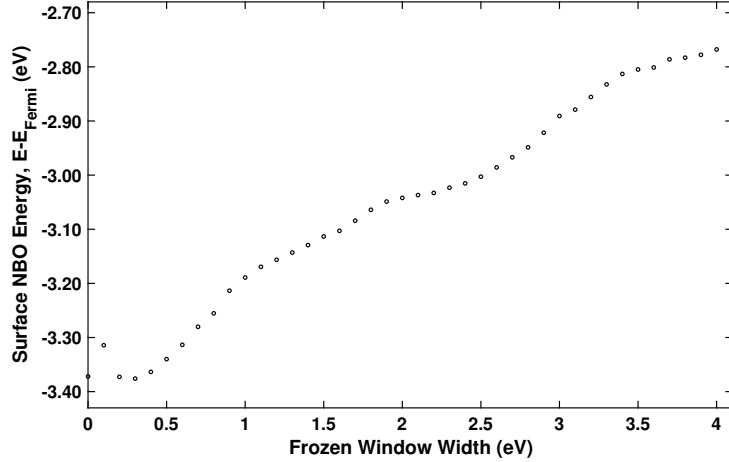


FIGURE B.4: Variation of the surface NBO energy (diagonal matrix element of Eq. B.3) across increasing frozen window widths for the symmetric CdS slab in Ref. [31]. Energies are shown with respect to the Fermi energy as calculated by DFT. We employed Wannier localization with disentanglement to extract only the sulfur-centered sp^3 -orbital subspace from all eigenstates with energies $E - E_{Fermi} < 0.2$ eV. The frozen window maximum is $E - E_{Fermi} \approx 0.15$ eV in all calculations, and the frozen window minimum sets the width.

are simply less accurate because less of the band structure is preserved during localization. However, it is important to realize that while the valence region is better preserved with a larger frozen window, it is also true that the low-lying sulfur s-orbital bands become *far* less accurate as the frozen window becomes wider (Figure B.5). This effect significantly influences the values of the OSEs since they are effectively a weighted average over the DFT eigenvalues (Eq. B.2 and B.3). Because parts of the resulting Wannier band structure will always be inaccurate relative to the input DFT band structure whenever disentanglement is used, it is difficult to conclude with any certainty which choice of frozen window width yields the most appropriate Hamiltonian description.

Because the Green's functions for the impurity states rely on the accuracy of these OSEs (specifically, the $E_{\pm} = \epsilon_0 \pm t$ term in the denominator), this disentanglement approach is far less reliable, in general, for evaluating superexchange corrections. In fact, for CdS it turns out that even a frozen window width of ~ 1 eV is too wide because of the positively-drifting OSEs. For frozen windows larger than ~ 1 eV wide, the Green's functions for some of the relevant undressed $|\pm\rangle$ states do not find corresponding (dressed) bound-state resonances

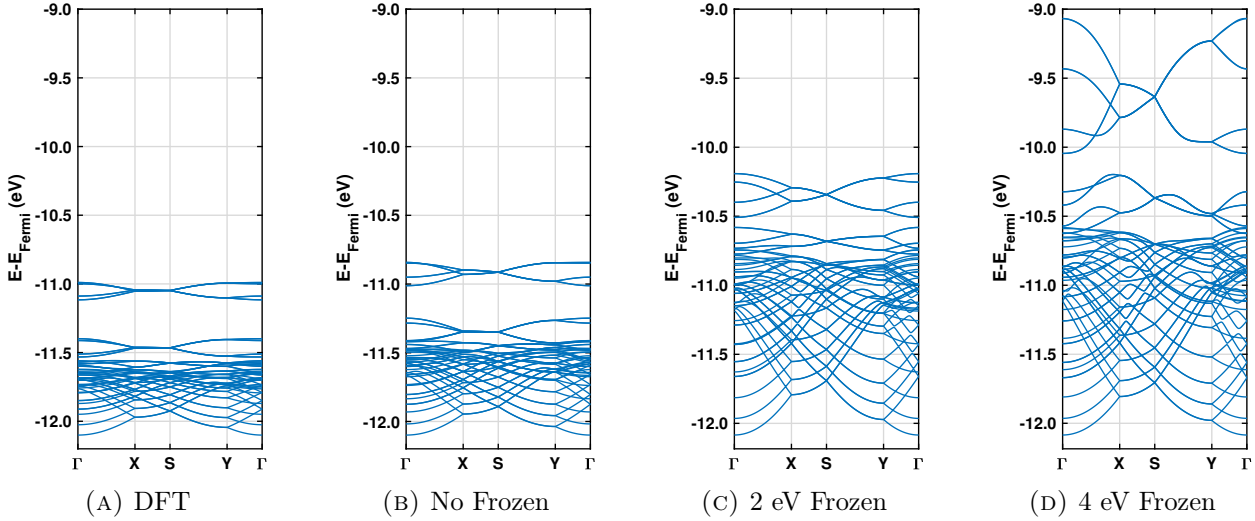


FIGURE B.5: Band structures for the symmetric CdS surface slab. We restrict the energy axis to show only the bands dominated by the sulfur s-orbital bands in all panels. Panel (A) shows the DFT band structure. The remaining panels correspond to the Wannier-basis band structures for the sulfur-centered sp^3 subspace, calculated using disentanglement and (B) no frozen window, (C) a frozen window width of 2 eV, and (D) a frozen window width of 4 eV. The frozen window maximum in the last 2 panels is $E - E_{Fermi} \approx 0.15$ eV).

outside of the continuum's energy range because the OSEs have drifted deeper into the continuum due to error.

There are two primary ways to avoid disentanglement when trying to find our desired sp^3 subspace. The first option involves performing a full localization, where we include all states with energies $E - E_{Fermi} < 0.2$ eV as inputs, and we desire the same number of orbitals as outputs. For a surface slab with over 20,000 (number of bands \times number of k-points) occupied Bloch states, this method suffers from very poor convergence speed: initial testing we conducted revealed our calculations could not reach default convergence even after 200,000 minimization steps.

The second option involves manually excluding certain band states — the bands dominated by the cadmium d orbitals — from the localization procedure entirely, followed by a full localization of the remaining band structure below $E - E_{Fermi} < 0.2$ eV. This second option is the approach we take in this work because, for both CdS and CdSe, the minimization takes roughly 3000 steps to reach a convergence cutoff that is ten times more strict than

the default. This convergence speed is remarkable considering over 10,000 states are still included as inputs in this second approach.

B.4.2 Wannier Localization without Disentanglement for CdS: The “Excluded Bands” Procedure

Since we exclude bands from the Wannier calculations entirely with this methodology, we call this approach the “excluded bands” procedure. In all future discussions, it is understood that we exclude, by default, the conduction band states with energies $E - E_{Fermi} > 0.2$ eV since those were not important even during the disentanglement protocol.

B.4.2.1 Excluded Bands

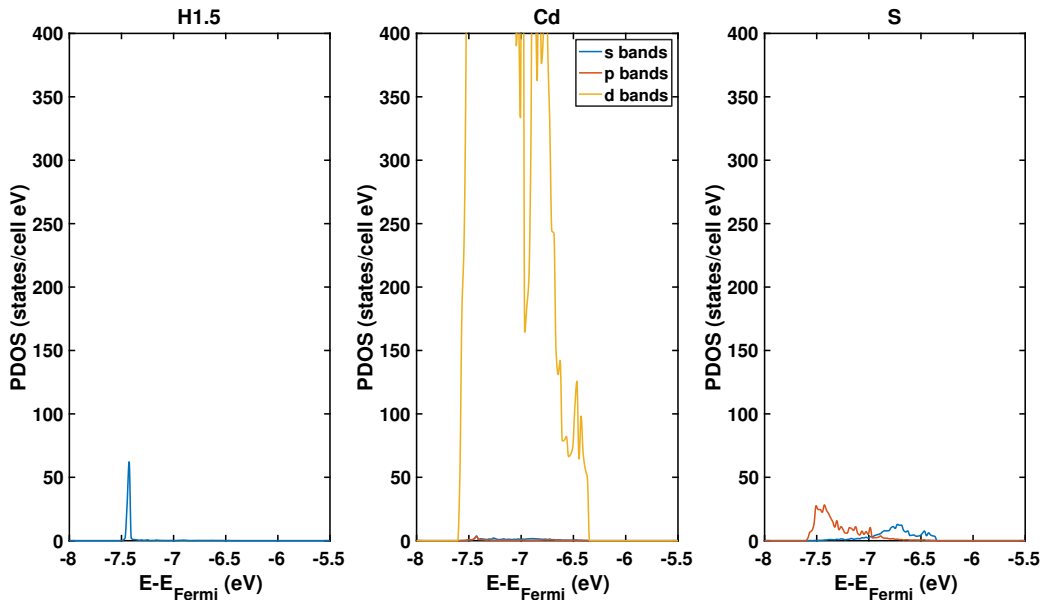


FIGURE B.6: Projected densities of states (PDOS) over the interval $-8 < E - E_{Fermi} < -5.5$ eV for all atoms in the symmetric CdS surface slab. The y -axis is truncated to 25% of the maximum value in this region. The cadmium d orbitals dominate the band structure over this energy range, motivating their removal from the Wannier localization step.

To circumvent the need for disentanglement when performing Wannier localization, we choose to explicitly remove all bands dominated by the cadmium d orbitals from the calculation. Our rationale for removing these states is two-fold. First, hole traps in both CdS

and CdSe nanocrystals are attributed in the literature to undercoordinated S or Se atoms within the nanoparticle.^{35–37,43,49} Second, if surface-trapped holes tunnel into the bulk of the material, we reason they will stay associated with these atoms because the valence region that spans 4 eV in either material is dominated by S/Se p-orbital bands.

To motivate this decision using DFT, we calculate the projected densities of states (PDOS) for all atoms in our surface slabs. Figure B.6 shows the PDOS corresponding to cadmium-dominated bands for CdS. We have truncated the y -axis to roughly 25% of the largest value of the PDOS for the cadmium d-orbital bands to compare with the PDOS for the H1.5 and sulfur atoms. Nearly all of the state density in this region corresponds to the metal d orbitals, suggesting the removal of these bands will incur minimal error.

B.4.2.2 Included Bands

For comparison, we show all other energy ranges over which the PDOS are non-zero in Figures B.7-B.9, in order of increasing energy. The bands contributing to these state densities are to be included in the Wannier localization procedure. These bands are dominated by the atomic orbitals of the non-cadmium atoms; however, there is some non-negligible contribution from the cadmium orbitals in these regions. Because of the non-zero contribution from the cadmium atoms in these regions of the band structure, we expect the final Wannier orbitals to be less localized than they would be if disentanglement were used. However, if this effect is small and if we localize all remaining states in the system, the trade-off with this approach is that there is no longer any need to define a frozen window. All input states by default will be exactly preserved.

To account for all remaining bands in the system, we perform Wannier localization using the states represented by Figures B.7-B.9. This requires we begin the localization procedure with the following initial guesses:

- four sp³ orbitals centered on each sulfur atom,
- one s orbital centered on each H1.5 atom.

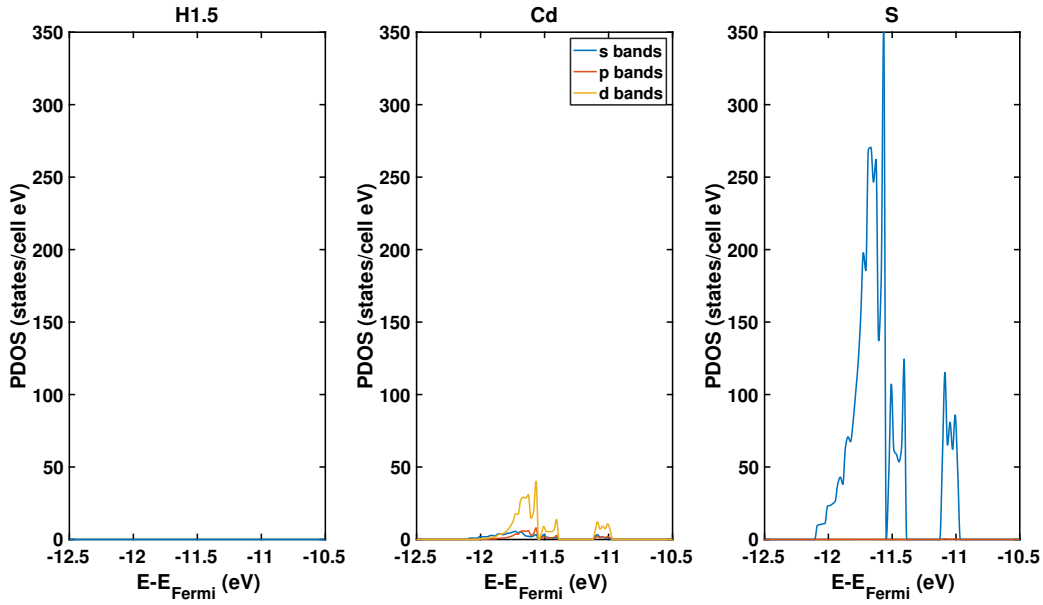


FIGURE B.7: PDOS over the interval $-12.5 < E - E_{Fermi} < -10.5$ eV for all atoms in the symmetric CdS surface slab.³¹ The sulfur s orbitals dominate the band structure over this energy range.

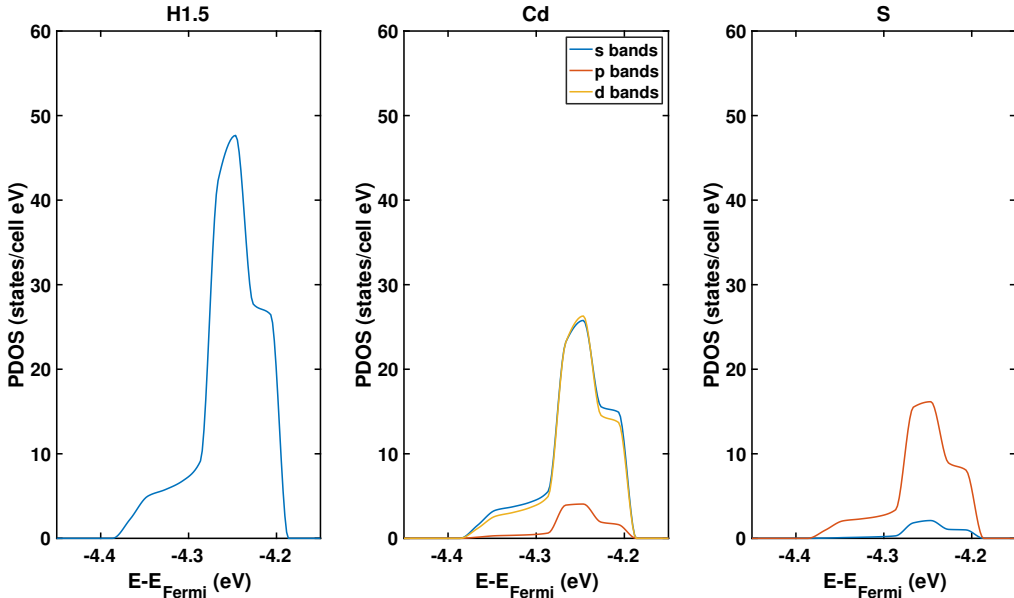


FIGURE B.8: PDOS over the interval $-4.45 < E - E_{Fermi} < -4.15$ eV for all atoms in the symmetric CdS surface slab.³¹ The H1.5 s orbitals dominate the band structure over this energy range.

Generating the first set of orbitals is ultimately the goal of the entire procedure, so we do not explain that choice further. We include the second set of orbitals simply because excluding them would incur an additional error in the final orbitals' degree of localization.

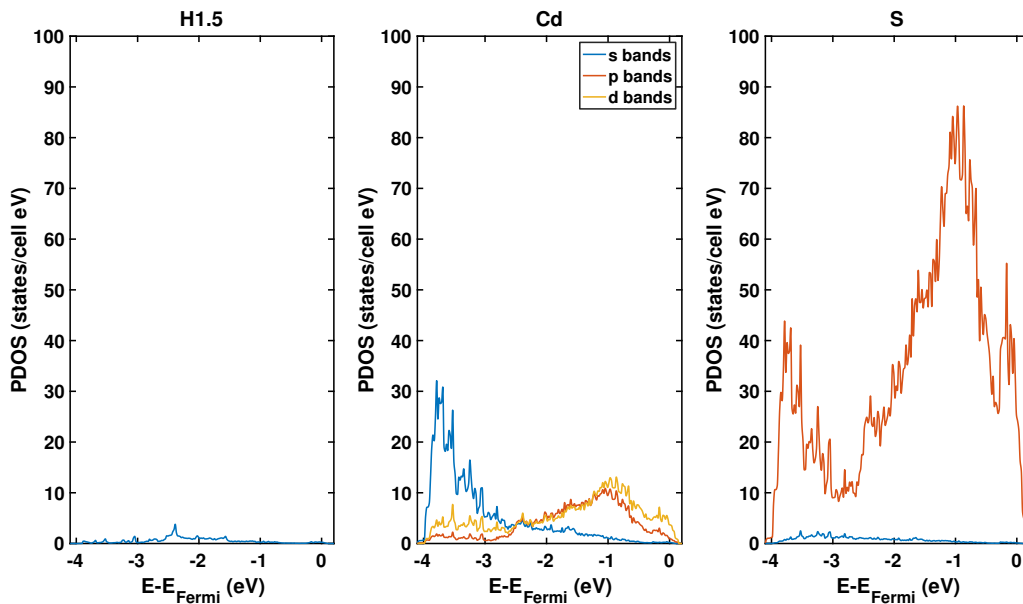


FIGURE B.9: PDOS over the interval $-4.1 < E - E_{Fermi} < 0.2$ eV for all atoms in the symmetric CdS surface slab.³¹ The sulfur p orbitals dominate the band structure over this energy range.

This error stems from the small, but non-zero, contribution of the H1.5 orbitals in the PDOS of the valence region (Figure B.9). This raises a source of ambiguity: one could exclude these H1.5-dominated bands as well and focus solely on generating the desired sp^3 orbital subspace. However, there are only 8 H1.5-dominated bands, compared to the 320 cadmium-dominated bands we excluded; therefore, including these 8 extra bands should not lead to a significant drop in computational speed.

Lastly, the keen eye may notice in Figure B.6 that there is non-zero s-orbital density corresponding to the H1.5 atoms in the cadmium-dominated bands we exclude. Therefore, the set of H1.5-centered s orbitals that we minimize will not represent the best, most-localized orbitals for those atoms since some of the information needed to maximally localize them has been removed. This is not an issue because characterizing these orbitals is not the goal of this procedure. Including these H1.5-centered s orbitals only serves to improve the minimization of the sulfur-centered sp^3 orbitals, since the PDOS corresponding to the H1.5 states is non-zero in the sulfur-dominated valence region (Figure B.9).

B.4.3 Wannier Localization without Disentanglement for CdSe

The description of the Wannier localization procedure for CdSe is practically identical to the above (section B.4.2). We exclude as few states as possible, only the intervening cadmium-dominated bands, and we localize everything else. Thus, within this constraint, we extract two orbital subspaces: (1) the desired subspace of selenium-centered sp^3 orbitals, and (2) an additional set of H1.5-centered s orbitals to help improve the sp^3 minimization. Figures B.10-B.13 summarize all PDOS results for CdSe, which has a very similar electronic structure compared to CdS. Just like with our results for CdS, we truncate the y -axis for the cadmium-dominated region (Figure B.10) to roughly 25% of the maximum value, so we can compare the PDOS across the different atoms in the surface slab.

B.4.3.1 Excluded Bands

Figure B.10 shows the PDOS corresponding to the cadmium-dominated bands for CdSe.

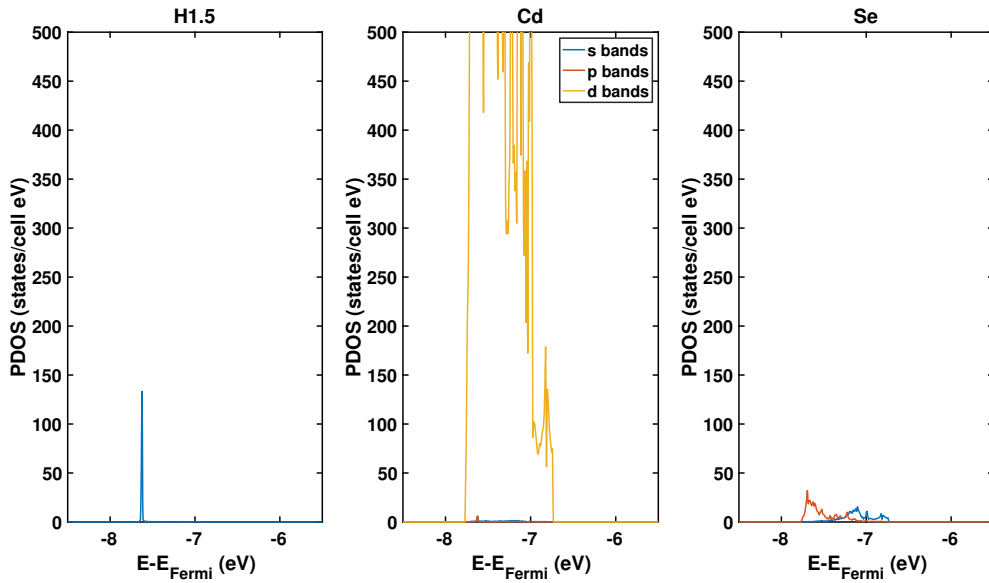


FIGURE B.10: PDOS over the interval $-8.5 < E - E_{Fermi} < -5.5$ eV for all atoms in the symmetric CdSe surface slab. The y -axis is truncated to 25% of the maximum value in this region. The cadmium d orbitals dominate the band structure over this energy range.

B.4.3.2 Included Bands

Figures B.11-B.13 shows all other non-zero PDOS.

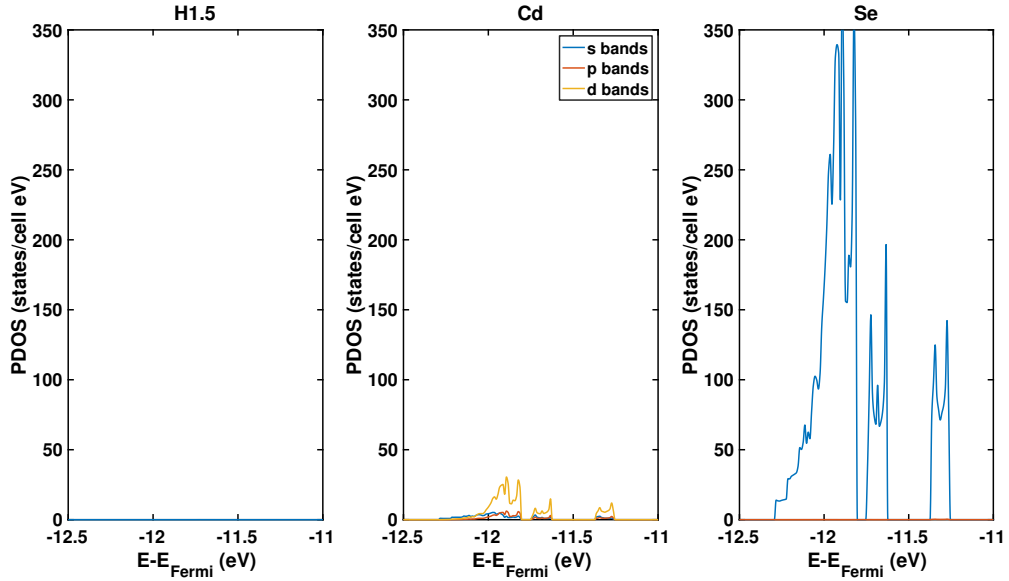


FIGURE B.11: PDOS over the interval $-12.5 < E - E_{Fermi} < -11$ eV for all atoms in the symmetric CdSe surface slab. The selenium s orbitals dominate the band structure over this energy range.

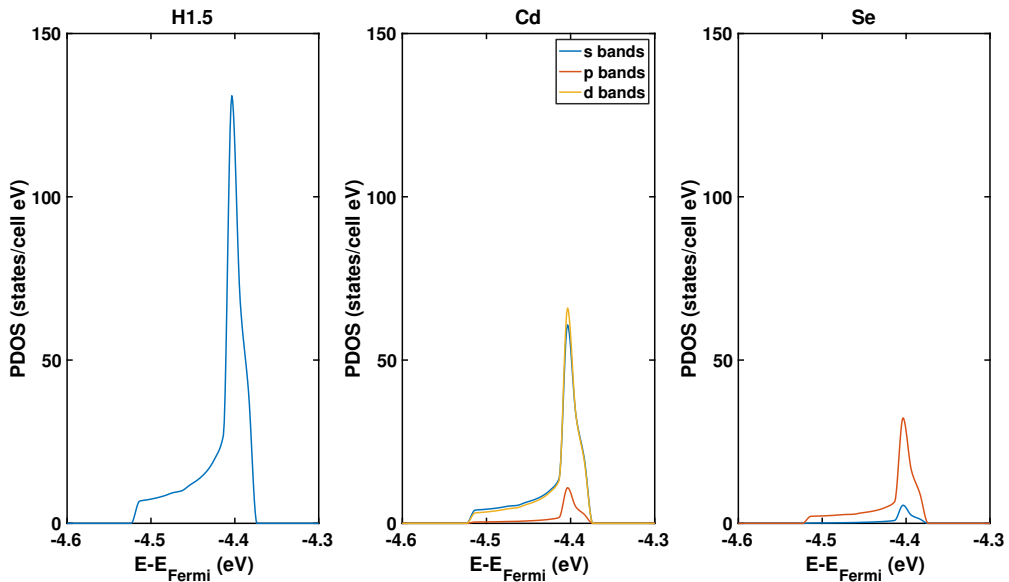


FIGURE B.12: PDOS over the interval $-4.6 < E - E_{Fermi} < -4.3$ eV for all atoms in the symmetric CdSe surface slab. The H1.5 s orbitals dominate the band structure over this energy range. Note that the densities in this PDOS are more strongly peaked relative to the densities in Figure B.8 for CdS because we achieve a stricter force convergence for the CdSe slab. Minor geometric asymmetries are slightly more pronounced in the CdS slab.

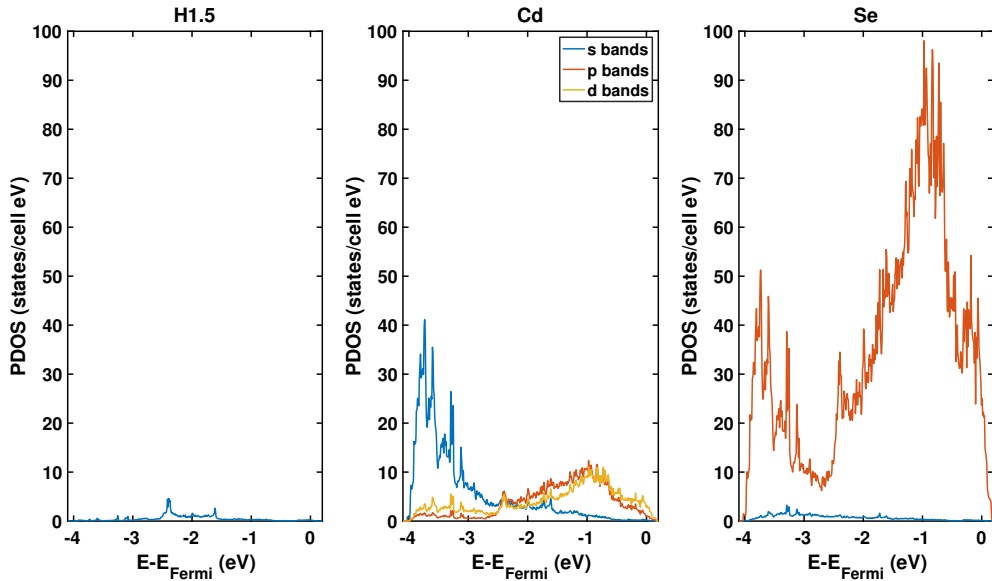


FIGURE B.13: PDOS over the interval $-4.1 < E - E_{Fermi} < 0.2$ eV for all atoms in the symmetric CdSe surface slab. The selenium p orbitals dominate the band structure over this energy range, motivating their inclusion into the Wannier localization step.

B.5 Wannier Localization Convergence Details

For both CdS and CdSe, we perform the Wannier localization step without disentanglement by excluding the cadmium-dominated bands from the calculations. Within this framework, we require that the total orbital spread as calculated by the Wannier90 code^{69,79,80,82} change by less than 10^{-11} Å² across 10 consecutive iterations. This is the same convergence we required in Chapter 2. Lastly, we set “guiding_centres = true” as recommended by the Wannier90 user manual in order to avoid local minima during the orbital minimization. We also employed this setting in Chapter 2, but we did not mention this detail explicitly.

B.6 Orbital Spread Comparison

In this section, we briefly compare the final spreads of the relevant NBOs between the disentanglement and “excluded bands” methodologies. For either methodology, Wannier90 determines the final orbitals are real, suggesting the global minimum was found in each case.

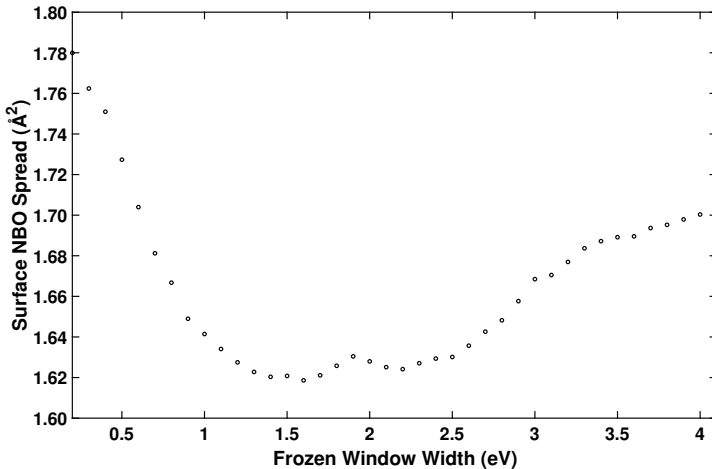


FIGURE B.14: Converged surface NBO spread as a function of frozen window width for the symmetric CdS surface slab. We show frozen window widths of 0.2 to 4.1 eV here. The smallest width we considered was approximately 0.15 eV, but we exclude that result from this plot since it does not affect our conclusions.

Figure B.14 shows the variation in the converged surface NBO spread for CdS for increasing frozen window widths. The smallest spread of roughly 1.62 \AA^2 occurs near a frozen window width of 1.6 eV. For comparison, the “excluded bands” approach that eliminates the need for disentanglement yields a final converged NBO spread of 1.78 \AA^2 . This spread is approximately equal to the largest spread from the scan in Figure B.14. Therefore, as predicted in section B.4, we find the NBO spreads are slightly larger when we remove the cadmium-dominated bands before performing Wannier localization. This slight increase in NBO spread is acceptable given we can now avoid any reliance on defining a frozen window.

Figure B.15 shows the variation in the converged surface NBO spread for CdSe for increasing frozen window widths. The smallest spread of roughly 1.90 \AA^2 occurs near a frozen window width of 1.6 eV. For comparison, the “excluded bands” approach that eliminates the need for disentanglement yields a final converged NBO spread of 2.08 \AA^2 . As with CdS, the slight increase in NBO spread is acceptable given we can now avoid any reliance on defining a frozen window.

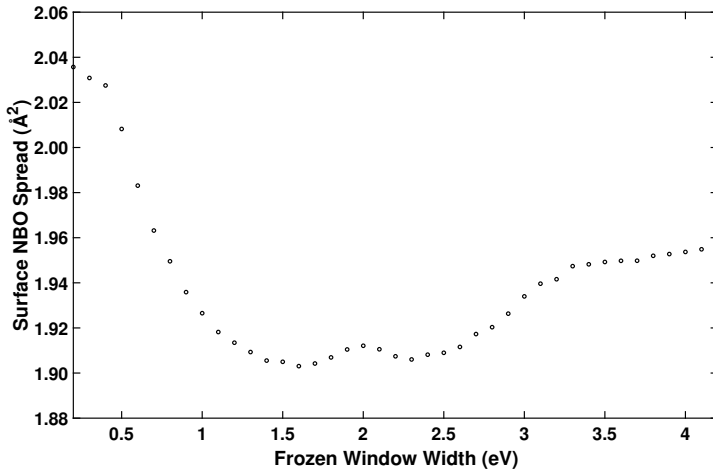


FIGURE B.15: Converged surface NBO spread as a function of frozen window width for the symmetric CdSe surface slab. We show frozen window widths of 0.2 to 4.1 eV here. The smallest width we considered was approximately 0.17 eV, but we exclude that result from this plot since it does not affect our conclusions.

B.7 Asymmetric CdS and CdSe Diffusion Results

In this section, we provide the superexchange results (Table B.1) for the asymmetric slab variants our CdS and CdSe surfaces. We refer the reader to Appendix A (section A.4.2) for the details on the asymmetric CdS slab. The details of the asymmetric CdSe slab are located in section B.1.2.2. As with the symmetric slabs, we exclude the cadmium-dominated bands from the Wannier localization step (see sections B.4.2 and B.4.3), and we construct Wannier orbitals from the remaining bands. We initialize the localization step with

- four sp³ orbitals centered on each selenium atom,
- one s orbital centered on each H1.5 atom.

These orbitals take care of all of the remaining bands. Despite this, one may wonder why we do not initialize with any orbitals on the H.5 atoms that passivate the chalcogen (S/Se) atoms on the bottom layer since the H.5 atoms add more electrons to the DFT calculation. It turns out the number of bands with energies $E - E_{Fermi} < 0.2$ eV is the same for the symmetric and asymmetric slab variants: before excluding the cadmium-dominated states, there are 584 bands in total at each k-point, and after excluding the cadmium-dominated

states, there are 264 bands in total at each k-point. Therefore, the H.5 atoms do not change the number of input states, which would have required modifying the Wannier localization procedure further. The electron count is different between the slabs by 2, but this effect only has a minor influence on the electronic filling across the highest-energy input bands.

System	t_{\parallel}	t'	σ_{\parallel}	σ'	$ V_{\text{eff}} $	$ \tilde{V}_{\text{eff}} $
CdS	-5.3	-4.6	44.5	33.4	8.4	56.5
CdSe	-8.6	-7.8	47.6	34.7	14.0	54.5

TABLE B.1: Relevant matrix elements (in meV) for trapped-hole diffusion in Cd-chalcogenide nanocrystals as calculated using the asymmetric slab variants. We define all terms here exactly as they are in Chapter 3. For both CdS and CdSe, all superexchange-inclusive terms outweigh the direct-only terms by roughly an order of magnitude. All couplings for both materials are nearly identical with the results presented in Chapter 3.

B.8 Perpendicular Couplings: Symmetric Slabs

In this section, we report on the coupling results (direct and superexchange) corresponding to the perpendicular hopping events in both CdS and CdSe. We limit our discussion to the symmetric slabs since the results for the asymmetric slabs are nearly identical. We reported on the direct perpendicular matrix elements for CdS in Appendix A (section A.2.6), though the Wannier-localization protocol we employed was different, as discussed earlier (section B.4). The perpendicular hopping event does not contribute to the data measured by Utterback *et al.*^{30,32,33} since the direction of travel is around the waists of the nanorods, not down their lengths (the crystal *c*-axis).

Table B.2 summarizes the results for all terms that involve the perpendicular-hop matrix elements. The elements t_{\perp} and σ_{\perp} are the direct and superexchange elements, respectively. Additionally, we calculate effective couplings

$$|V_{\text{eff}}^{\perp}|^2 = |t_{\perp}|^2 + 2|t'|^2 \quad (\text{B.12})$$

and

$$|\tilde{V}_{\text{eff}}^{\perp}|^2 = |\tilde{t}_{\perp}|^2 + 2|\tilde{t}'|^2 \quad (\text{B.13})$$

$$= |t_{\perp} + \sigma_{\perp}|^2 + 2|t' + \sigma'|^2. \quad (\text{B.14})$$

These effective couplings are analogous to those presented in Chapter 3, except these above correspond to the perpendicular diffusion constant, D_{\perp} , for which we derived an expression in Appendix A (section A.1). One detail of note concerns the completely constructive interference between t_{\perp} and σ_{\perp} . This helps to enhance the coupling along this direction, in contrast with the results for t_{\parallel} and σ_{\parallel} in Chapter 3.

System	t_{\perp}	σ_{\perp}	$ V_{\text{eff}}^{\perp} $	$ \tilde{V}_{\text{eff}}^{\perp} $
CdS	-39.9	-45.6	40.4	94.7
CdSe	-48.7	-56.9	50.0	112.4

TABLE B.2: Perpendicular-hop matrix elements, t_{\perp} and σ_{\perp} , between neighboring surface chalcogen sites in Cd-chalcogenide nanocrystals for the $2 \times 2 \times 8$ symmetric slab variants. Also shown are the effective coupling terms, V_{eff}^{\perp} and $\tilde{V}_{\text{eff}}^{\perp}$, corresponding to the perpendicular diffusion constant, D_{\perp} . All values are given in millielectronvolts (meV). These coupling terms do not contribute to the transient absorption data observed by Utterback *et al.*^{30,32,33}

Bibliography

- (1) Bloch, F. Über die Quantenmechanik der Elektronen in Kristallgittern. *Z. Phys.* **1929**, *52*, 555–600.
- (2) Wigner, E.; Seitz, F. On the Constitution of Metallic Sodium. *Phys. Rev.* **1933**, *43*, 804–810.
- (3) Wigner, E.; Seitz, F. On the Constitution of Metallic Sodium. II. *Phys. Rev.* **1934**, *46*, 509–524.
- (4) Slater, J. C. Wave Functions in a Periodic Potential. *Phys. Rev.* **1937**, *51*, 846–851.
- (5) Wannier, G. H. The Structure of Electronic Excitation Levels in Insulating Crystals. *Phys. Rev.* **1937**, *52*, 191–197.
- (6) Herring, C. A New Method for Calculating Wave Functions in Crystals. *Phys. Rev.* **1940**, *57*, 1169–1177.
- (7) Korringa, J. On the Calculation of the Energy of a Bloch Wave in a Metal. *Physica* **1947**, *13*, 392–400.
- (8) Kohn, W.; Rostoker, N. Solution of the Schrödinger Equation in Periodic Lattices with an Application to Metallic Lithium. *Phys. Rev.* **1954**, *94*, 1111–1120.
- (9) Phillips, J. C.; Kleinman, L. New Method for Calculating Wave Functions in Crystals and Molecules. *Phys. Rev.* **1959**, *116*, 287–294.
- (10) Ashcroft, N. W.; Mermin, N. D., *Solid State Physics*; Cengage Learning: Andover, MA, 1976.

- (11) Hohenberg, P.; Kohn, W. Inhomogeneous Electron Gas. *Phys. Rev.* **1964**, *136*, B864–B871.
- (12) Anderson, P. W. Absence of Diffusion in Certain Random Lattices. *Phys. Rev.* **1958**, *109*, 1492–1505.
- (13) NobelPrize.org. The Nobel Prize in Physics 1977. <https://www.nobelprize.org/prizes/physics/1977/summary/> (accessed July 30, 2020), 1977.
- (14) Kondo, J. Resistance Minimum in Dilute Magnetic Alloys. *Prog. Theor. Phys.* **1964**, *32*, 37–49.
- (15) Mahan, G. D., *Many-Particle Physics*, 3rd ed.; Kluwer Academic: New York, NY, 2000.
- (16) Wilson, K. G. The Renormalization Group: Critical Phenomena and the Kondo Problem. *Rev. Mod. Phys.* **1975**, *47*, 773–840.
- (17) NobelPrize.org. The Nobel Prize in Physics 1982. <https://www.nobelprize.org/prizes/physics/1982/summary/> (accessed July 30, 2020), 1982.
- (18) Brus, L. E. Electron–Electron and Electron–Hole Interactions in Small Semiconductor Crystallites: The Size Dependence of the Lowest Excited Electronic State. *J. Chem. Phys.* **1984**, *80*, 4403–4409.
- (19) Brus, L. Electronic Wave Functions in Semiconductor Clusters: Experiment and Theory. *J. Phys. Chem.* **1986**, *90*, 2555–2560.
- (20) Bawendi, M. G.; Steigerwald, M. L.; Brus, L. E. The Quantum Mechanics of Larger Semiconductor Clusters (“Quantum Dots”). *Annu. Rev. Phys. Chem.* **1990**, *41*, 477–496.
- (21) Peng, X.; Manna, L.; Yang, W.; Wickham, J.; Scher, E.; Kadavanich, A.; Alivisatos, A. P. Shape Control of CdSe Nanocrystals. *Nature* **2000**, *404*, 59–61.

- (22) Rossetti, R.; Nakahara, S.; Brus, L. E. Quantum Size Effects in the Redox Potentials, Resonance Raman Spectra, and Electronic Spectra of CdS Crystallites in Aqueous Solution. *J. Chem. Phys.* **1983**, *79*, 1086–1088.
- (23) Kamat, P. V. Quantum Dot Solar Cells. Semiconductor Nanocrystals as Light Harvesters. *J. Phys. Chem. C* **2008**, *112*, 18737–18753.
- (24) Nozik, A. J.; Beard, M. C.; Luther, J. M.; Law, M.; Ellingson, R. J.; Johnson, J. C. Semiconductor Quantum Dots and Quantum Dot Arrays and Applications of Multiple Exciton Generation to Third-Generation Photovoltaic Solar Cells. *Chem. Rev.* **2010**, *110*, PMID: 20945911, 6873–6890.
- (25) Talapin, D. V.; Lee, J.-S.; Kovalenko, M. V.; Shevchenko, E. V. Prospects of Colloidal Nanocrystals for Electronic and Optoelectronic Applications. *Chem. Rev.* **2010**, *110*, PMID: 19958036, 389–458.
- (26) Han, Z.; Qiu, F.; Eisenberg, R.; Holland, P. L.; Krauss, T. D. Robust Photogeneration of H₂ in Water Using Semiconductor Nanocrystals and a Nickel Catalyst. *Science* **2012**, *338*, 1321–1324.
- (27) Wilker, M. B.; Schnitzenbaumer, K. J.; Dukovic, G. Recent Progress in Photocatalysis Mediated by Colloidal II-VI Nanocrystals. *Isr. J. Chem.* **2012**, *52*, 1002–1015.
- (28) Dabbousi, B. O.; Rodriguez-Viejo, J.; Mikulec, F. V.; Heine, J. R.; Mattossi, H.; Ober, R.; Jensen, K. F.; Bawendi, M. G. (CdSe)ZnS Core–Shell Quantum Dots: Synthesis and Characterization of a Size Series of Highly Luminescent Nanocrystallites. *J. Phys. Chem. B* **1997**, *101*, 9463–9475.
- (29) Burda, C.; Chen, X.; Narayanan, R.; El-Sayed, M. A. Chemistry and Properties of Nanocrystals of Different Shapes. *Chem. Rev.* **2005**, *105*, 1025–1102.
- (30) Utterback, J. K.; Grennell, A. N.; Wilker, M. B.; Pearce, O. M.; Eaves, J. D.; Dukovic, G. Observation of Trapped-Hole Diffusion on the Surfaces of CdS Nanorods. *Nat. Chem.* **2016**, *8*, 1061–1066.

- (31) Cline, R. P.; Utterback, J. K.; Strong, S. E.; Dukovic, G.; Eaves, J. D. On the Nature of Trapped-Hole States in CdS Nanocrystals and the Mechanism of Their Diffusion. *J. Phys. Chem. Lett.* **2018**, *9*, 3532–3537.
- (32) Utterback, J. K.; Hamby, H.; Pearce, O. M.; Eaves, J. D.; Dukovic, G. Trapped-Hole Diffusion in Photoexcited CdSe Nanorods. *J. Phys. Chem. C* **2018**, *122*, 16974–16982.
- (33) Utterback, J. K.; Ruzicka, J. L.; Hamby, H.; Eaves, J. D.; Dukovic, G. Temperature-Dependent Transient Absorption Spectroscopy Elucidates Trapped-Hole Dynamics in CdS and CdSe Nanorods. *J. Phys. Chem. Lett.* **2019**, *10*, 2782–2787.
- (34) Wuister, S. F.; de Mello Donegá, C.; Meijerink, A. Influence of Thiol Capping on the Exciton Luminescence and Decay Kinetics of CdTe and CdSe Quantum Dots. *J. Phys. Chem. B* **2004**, *108*, 17393–17397.
- (35) Jasieniak, J.; Mulvaney, P. From Cd-Rich to Se-Rich – the Manipulation of CdSe Nanocrystal Surface Stoichiometry. *J. Am. Chem. Soc.* **2007**, *129*, 2841–2848.
- (36) Gómez-Campos, F. M.; Califano, M. Hole Surface Trapping in CdSe Nanocrystals: Dynamics, Rate Fluctuations, and Implications for Blinking. *Nano Lett.* **2012**, *12*, 4508–4517.
- (37) Wei, H. H.-Y.; Evans, C. M.; Swartz, B. D.; Neukirch, A. J.; Young, J.; Prezhdo, O. V.; Krauss, T. D. Colloidal Semiconductor Quantum Dots with Tunable Surface Composition. *Nano Lett.* **2012**, *12*, 4465–4471.
- (38) Peterson, M. D.; Cass, L. C.; Harris, R. D.; Edme, K.; Sung, K.; Weiss, E. A. The Role of Ligands in Determining the Exciton Relaxation Dynamics in Semiconductor Quantum Dots. *Annu. Rev. Phys. Chem.* **2014**, *65*, 317–339.
- (39) Busby, E.; Anderson, N. C.; Owen, J. S.; Sfeir, M. Y. Effect of Surface Stoichiometry on Blinking and Hole Trapping Dynamics in CdSe Nanocrystals. *J. Phys. Chem. C* **2015**, *119*, 27797–27803.

- (40) Gao, Y.; Peng, X. Photogenerated Excitons in Plain Core CdSe Nanocrystals with Unity Radiative Decay in Single Channel: The Effects of Surface and Ligands. *J. Am. Chem. Soc.* **2015**, *137*, 4230–4235.
- (41) Krause, M. M.; Kambhampati, P. Linking Surface Chemistry to Optical Properties of Semiconductor Nanocrystals. *Phys. Chem. Chem. Phys.* **2015**, *17*, 18882–18894.
- (42) Kilina, S. V.; Tamukong, P. K.; Kilin, D. S. Surface Chemistry of Semiconducting Quantum Dots: Theoretical Perspectives. *Acc. Chem. Res.* **2016**, *49*, 2127–2135.
- (43) Houtepen, A. J.; Hens, Z.; Owen, J. S.; Infante, I. On the Origin of Surface Traps in Colloidal II–VI Semiconductor Nanocrystals. *Chem. Mater.* **2017**, *29*, 752–761.
- (44) Rosenthal, S.; McBride, J.; Pennycook, S.; Feldman, L. Synthesis, Surface Studies, Composition and Structural Characterization of CdSe, Core/Shell and Biologically Active Nanocrystals. *Surf. Sci. Rep.* **2007**, *62*, 111–157.
- (45) Knowles, K. E.; Tice, D. B.; McArthur, E. A.; Solomon, G. C.; Weiss, E. A. Chemical Control of the Photoluminescence of CdSe Quantum Dot–Organic Complexes with a Series of Para-Substituted Aniline Ligands. *J. Am. Chem. Soc.* **2010**, *132*, 1041–1050.
- (46) Sadhu, S.; Patra, A. Relaxation Dynamics of Anisotropic Shaped CdS Nanoparticles. *J. Phys. Chem. C* **2011**, *115*, 16867–16872.
- (47) Utterback, J. K.; Wilker, M. B.; Brown, K. A.; King, P. W.; Eaves, J. D.; Dukovic, G. Competition Between Electron Transfer, Trapping, and Recombination in CdS Nanorod–Hydrogenase Complexes. *Phys. Chem. Chem. Phys.* **2015**, *17*, 5538–5542.
- (48) Klimov, V. I.; Schwarz, C. J.; McBranch, D. W.; Leatherdale, C. A.; Bawendi, M. G. Ultrafast Dynamics of Inter- and Intraband Transitions in Semiconductor Nanocrystals: Implications for Quantum-Dot Lasers. *Phys. Rev. B: Condens. Matter Mater. Phys.* **1999**, *60*, R2177–R2180.

- (49) Keene, J. D.; McBride, J. R.; Orfield, N. J.; Rosenthal, S. J. Elimination of Hole-Surface Overlap in Graded $\text{CdS}_x\text{Se}_{1-x}$ Nanocrystals Revealed by Ultrafast Fluorescence Upconversion Spectroscopy. *ACS Nano* **2014**, *8*, 10665–10673.
- (50) Wu, K.; Du, Y.; Tang, H.; Chen, Z.; Lian, T. Efficient Extraction of Trapped Holes from Colloidal CdS Nanorods. *J. Am. Chem. Soc.* **2015**, *137*, 10224–10230.
- (51) Quarti, C.; Milani, A.; Castiglioni, C. Ab Initio Calculation of the IR Spectrum of PTFE: Helical Symmetry and Defects. *J. Phys. Chem. B* **2013**, *117*, PMID: 23244728, 706–718.
- (52) Atkin, J. M.; Sass, P. M.; Teichen, P. E.; Eaves, J. D.; Raschke, M. B. Nanoscale Probing of Dynamics in Local Molecular Environments. *J. Phys. Chem. Lett.* **2015**, *6*, PMID: 26528865, 4616–4621.
- (53) Clark, E. S. The Molecular Conformations of Polytetrafluoroethylene: Forms II and IV. *Polymer* **1999**, *40*, 4659–4665.
- (54) Holt, D.; Farmer, B. Modeling of Helix Reversal Defects in Polytetrafluoroethylene: II. Molecular Dynamics Simulations. *Polymer* **1999**, *40*, 4673–4684.
- (55) Klimov, V.; Bolivar, P. H.; Kurz, H. Ultrafast Carrier Dynamics in Semiconductor Quantum Dots. *Phys. Rev. B: Condens. Matter Mater. Phys.* **1996**, *53*, 1463–1467.
- (56) Guyot-Sionnest, P.; Wehrenberg, B.; Yu, D. Intraband Relaxation in CdSe Nanocrystals and the Strong Influence of the Surface Ligands. *J. Chem. Phys.* **2005**, *123*, 074709.
- (57) Bullen, C.; Mulvaney, P. The Effects of Chemisorption on the Luminescence of CdSe Quantum Dots. *Langmuir* **2006**, *22*, 3007–3013.
- (58) Knowles, K. E.; McArthur, E. A.; Weiss, E. A. A Multi-Timescale Map of Radiative and Nonradiative Decay Pathways for Excitons in CdSe Quantum Dots. *ACS Nano* **2011**, *5*, 2026–2035.

- (59) Wu, K.; Zhu, H.; Liu, Z.; Rodríguez-Córdoba, W.; Lian, T. Ultrafast Charge Separation and Long-Lived Charge Separated State in Photocatalytic CdS-Pt Nanorod Heterostructures. *J. Am. Chem. Soc.* **2012**, *134*, 10337–10340.
- (60) Mooney, J.; Krause, M. M.; Saari, J. I.; Kambhampati, P. Challenge to the Deep-Trap Model of the Surface in Semiconductor Nanocrystals. *Phys. Rev. B: Condens. Matter Mater. Phys.* **2013**, *87*, 081201.
- (61) Kilina, S. V.; Neukirch, A. J.; Habenicht, B. F.; Kilin, D. S.; Prezhdo, O. V. Quantum Zeno Effect Rationalizes the Phonon Bottleneck in Semiconductor Quantum Dots. *Phys. Rev. Lett.* **2013**, *110*, 180404.
- (62) Rantala, T. T.; Rantala, T. S.; Lantto, V.; Vaara, J. Surface Relaxation of the $(10\bar{1}0)$ Face of Wurtzite CdS. *Surf. Sci.* **1996**, *352*, 77–82.
- (63) Widmer-Cooper, A.; Geissler, P. Orientational Ordering of Passivating Ligands on CdS Nanorods in Solution Generates Strong Rod–Rod Interactions. *Nano Lett.* **2014**, *14*, 57–65.
- (64) Sun, W.; Ceder, G. Efficient Creation and Convergence of Surface Slabs. *Surf. Sci.* **2013**, *617*, 53–59.
- (65) Deng, H.-X.; Li, S.-S.; Li, J.; Wei, S.-H. Effect of Hydrogen Passivation on the Electronic Structure of Ionic Semiconductor Nanostructures. *Phys. Rev. B: Condens. Matter Mater. Phys.* **2012**, *85*, 195328.
- (66) Zhang, Y.; Zhang, J.; Tse, K.; Wong, L.; Chan, C.; Deng, B.; Zhu, J. Pseudo-Hydrogen Passivation: A Novel Way to Calculate Absolute Surface Energy of Zinc Blende $(111)/(1\bar{1}\bar{1})$ Surface. *Sci. Rep.* **2016**, *6*, 20055.
- (67) Sakurai, J. J.; Napolitano, J., *Modern Quantum Mechanics*, 2nd ed.; Pearson: San Francisco, CA, 2011.
- (68) Weiss, U., *Quantum Dissipative Systems*, 3rd ed.; World Scientific: Singapore, 2008.

- (69) Mostofi, A. A.; Yates, J. R.; Lee, Y.-S.; Souza, I.; Vanderbilt, D.; Marzari, N. Wannier90: A Tool for Obtaining Maximally-Localised Wannier Functions. *Comput. Phys. Commun.* **2008**, *178*, 685–699.
- (70) Alexandrov, A. S.; Mott, S. N., *Polarons & Bipolarons*; World Scientific: Singapore, 1995.
- (71) Tachiya, M. Generalization of the Marcus Equation for the Electron-Transfer Rate. *J. Phys. Chem.* **1993**, *97*, 5911–5916.
- (72) Deskins, N. A.; Dupuis, M. Electron Transport via Polaron Hopping in Bulk TiO₂: A Density Functional Theory Characterization. *Phys. Rev. B: Condens. Matter Mater. Phys.* **2007**, *75*, 195212.
- (73) Kresse, G.; Hafner, J. *Ab Initio* Molecular Dynamics for Liquid Metals. *Phys. Rev. B: Condens. Matter Mater. Phys.* **1993**, *47*, 558–561.
- (74) Kresse, G.; Hafner, J. *Ab Initio* Molecular-Dynamics Simulation of the Liquid-Metal-Amorphous-Semiconductor Transition in Germanium. *Phys. Rev. B: Condens. Matter Mater. Phys.* **1994**, *49*, 14251–14269.
- (75) Kresse, G.; Furthmüller, J. Efficient Iterative Schemes for *Ab Initio* Total-Energy Calculations Using a Plane-Wave Basis Set. *Phys. Rev. B: Condens. Matter Mater. Phys.* **1996**, *54*, 11169–11186.
- (76) Kresse, G.; Furthmüller, J. Efficiency of *Ab-Initio* Total Energy Calculations for Metals and Semiconductors Using a Plane-Wave Basis Set. *Comput. Mater. Sci.* **1996**, *6*, 15–50.
- (77) Blöchl, P. E. Projector Augmented-Wave Method. *Phys. Rev. B: Condens. Matter Mater. Phys.* **1994**, *50*, 17953–17979.
- (78) Kresse, G.; Joubert, D. From Ultrasoft Pseudopotentials to the Projector Augmented-Wave Method. *Phys. Rev. B: Condens. Matter Mater. Phys.* **1999**, *59*, 1758–1775.

- (79) Marzari, N.; Vanderbilt, D. Maximally Localized Generalized Wannier Functions for Composite Energy Bands. *Phys. Rev. B: Condens. Matter Mater. Phys.* **1997**, *56*, 12847–12865.
- (80) Souza, I.; Marzari, N.; Vanderbilt, D. Maximally Localized Wannier Functions for Entangled Energy Bands. *Phys. Rev. B: Condens. Matter Mater. Phys.* **2001**, *65*, 035109.
- (81) Kokalj, A. Computer Graphics and Graphical User Interfaces as Tools in Simulations of Matter at the Atomic Scale. *Comput. Mater. Sci.* **2003**, *28*, 155.
- (82) Marzari, N.; Mostofi, A. A.; Yates, J. R.; Souza, I.; Vanderbilt, D. Maximally Localized Wannier Functions: Theory and Applications. *Rev. Mod. Phys.* **2012**, *84*, 1419–1475.
- (83) Mostofi, A. A.; Yates, J. R.; Pizzi, G.; Lee, Y.-S.; Souza, I.; Vanderbilt, D.; Marzari, N. An Updated Version of Wannier90: A Tool for Obtaining Maximally-Localised Wannier Functions. *Comput. Phys. Commun.* **2014**, *185*, 2309–2310.
- (84) Mattuck, R. D., *A Guide to Feynman Diagrams in the Many-Body Problem*, 2nd ed.; Dover Publications: New York, NY, 1992.
- (85) Mukamel, S., *Principles of Nonlinear Optical Spectroscopy*; Oxford University Press: New York, NY, 1995.
- (86) Fano, U. Effects of Configuration Interaction on Intensities and Phase Shifts. *Phys. Rev.* **1961**, *124*, 1866–1878.
- (87) Anderson, P. W. Localized Magnetic States in Metals. *Phys. Rev.* **1961**, *124*, 41–53.
- (88) Rabani, E.; Baer, R. Theory of Multiexciton Generation in Semiconductor Nanocrystals. *Chem. Phys. Lett.* **2010**, *496*, 227–235.
- (89) Clark, E. S. The Crystal Structure of Polytetrafluoroethylene, Forms I and IV. *J. Macromol. Sci. B* **2006**, *45*, 201–213.

- (90) Bunn, C. W.; Cobbold, A. J.; Palmer, R. P. The Fine Structure of Polytetrafluoroethylene. *J. Polym. Sci.* **1958**, *28*, 365–376.
- (91) Bednarz, M.; Knoester, J. The Linear Absorption and Pump-Probe Spectra of Cylindrical Molecular Aggregates. *J. Phys. Chem. B* **2001**, *105*, 12913–12923.
- (92) Didraga, C.; Klugkist, J. A.; Knoester, J. Optical Properties of Helical Cylindrical Molecular Aggregates: The Homogeneous Limit. *J. Phys. Chem. B* **2002**, *106*, 11474–11486.
- (93) Lampoura, S. S.; Spitz, C.; Dähne, S.; Knoester, J.; Duppen, K. The Optical Dynamics of Excitons in Cylindrical J-Aggregates. *J. Phys. Chem. B* **2002**, *106*, 3103–3111.
- (94) Vlaming, S. M.; Augulis, R.; Stuart, M. C. A.; Knoester, J.; van Loosdrecht, P. H. M. Exciton Spectra and the Microscopic Structure of Self-Assembled Porphyrin Nanotubes. *J. Phys. Chem. B* **2009**, *113*, PMID: 19193042, 2273–2283.
- (95) Wilson, E. B. Some Mathematical Methods for the Study of Molecular Vibrations. *J. Chem. Phys.* **1941**, *9*, 76–84.
- (96) Griffiths, D. J., *Introduction to Electrodynamics*, 4th ed.; Cambridge University Press: Cambridge, UK, 2013.
- (97) Jackson, J. D., *Classical Electrodynamics*, 3rd ed.; Wiley: New York, NY, 1999.
- (98) Kubo, R. The Fluctuation-Dissipation Theorem. *Rep. Prog. Phys.* **1966**, *29*, 255–284.
- (99) Nitzan, A., *Chemical Dynamics in Condensed Phases: Relaxation, Transfer, and Reactions in Condensed Molecular Systems*; Oxford University Press: Oxford, UK, 2006.
- (100) Van Kampen, N. G., *Stochastic Processes in Physics and Chemistry*, 3rd ed.; Elsevier: Amsterdam, The Netherlands, 2007.

- (101) Ekuma, E. C.; Franklin, L.; Zhao, G. L.; Wang, J. T.; Bagayoko, D. Local Density Approximation Description of Electronic Properties of Wurtzite Cadmium Sulfide (w-CdS). *Can. J. Phys.* **2011**, *89*, 319–324.